Vertical Compact Torus Injection into the STOR-M Tokamak

A Thesis Submitted to the

College of Graduate Studies and Research

in Partial Fulfillment of the Requirements

for the degree of Doctor of Philosophy

in the Department of Physics and Engineering Physics

University of Saskatchewan

Saskatoon

By

Dazhi Liu

Permission to Use

In presenting this thesis in partial fulfilment of the requirements for a Postgraduate degree from the University of Saskatchewan, I agree that the Libraries of this University may make it freely available for inspection. I further agree that permission for copying of this thesis in any manner, in whole or in part, for scholarly purposes may be granted by the professor or professors who supervised my thesis work or, in their absence, by the Head of the Department or the Dean of the College in which my thesis work was done. It is understood that any copying or publication or use of this thesis or parts thereof for financial gain shall not be allowed without my written permission. It is also understood that due recognition shall be given to me and to the University of Saskatchewan in any scholarly use which may be made of any material in my thesis.

Requests for permission to copy or to make other use of material in this thesis in whole or part should be addressed to:

Head of the Department of Physics and Engineering Physics
University of Saskatchewan
Saskatoon, Saskatchewan
Canada S7N 5E2

Abstract

Central fuelling is a fundamental issue in the next generation tokamak-ITER (International Thermonuclear Experimental Reactor). It is essential for optimization of the bootstrap current which is proportional to the pressure gradient of trapped particles. The conventional fusion reactor fuelling techniques, such as gas puffing and cryogenic pellet injection, are considered inadequate to fulfill this goal due to premature ionization caused by high plasma temperature and density. Compact Torus (CT) injection is a promising fuelling technique for central fuelling a reactor-grade tokamak. An accelerated CT is expected to penetrate into the core region and deposit fuel there provided the CT kinetic energy density exceeds the magnetic energy density in a target plasma. This process is complicated and involves CT penetration into an external magnetic field, a CT stopping mechanism, magnetic reconnection, and excitation of plasma waves.

CTs can be injected at different angles with respect to the tokamak toroidal magnetic field, either horizontally or vertically. Normally, CTs are injected radially in the mid-plane of a tokamak. In this configuration, CTs will undergo a decelerating force due to the gradient of the tokamak toroidal magnetic field. CTs will stop inside the tokamak chamber or bunce back depending on the relation between kinetic energy density of injected CTs and the tokamak toroidal magnetic field energy density. In the case of vertical injection, deeper penetration is expected due to the absence of the gradient of the tokamak toroidal field in that direction. Experimental investigations on vertical CT injection into a tokamak will be of great significance.

The aim of this thesis is to experimentally investigate the feasibility of vertical CT injection into a tokamak and effects of CTs on tokamak plasma confinements. The Saskatchewan Torus-Modified (STOR-M) tokamak is currently the only tokamak equipped with a CT injector in the world. Vertical CT injection experiments have been performed in STOR-M by using the USCTI device (University of Saskatchewan

Compact Torus Injector). To perform vertical injection, the original USCTI has been modified by attaching a segment of 90° curved tube to deflect CT injection from horizontal to vertical direction. Therefore, a CT formed and accelerated by USCTI in horizontal direction will change its trajectory to vertical and be injected into STOR-M through a vertical port.

The main findings of this thesis are: (1) The horizontally injected CT could be deflected to the vertical direction with a velocity $\sim 130\,\mathrm{kms}^{-1}$ and penetrated into the STOR-M plasma by the curved drift tube. A significant increase in the CT velocity after passing the curved tube, from $130\,\mathrm{kms}^{-1}$ to $270\,\mathrm{kms}^{-1}$, has been achieved by further attaching a copper inner electrode. (2) Vertical compact torus injection for fuelling a tokamak has been successfully demonstrated for the first time. Disruption-free discharges of STOR-M have been obtained with vertical CT injection. Prompt increases both in line-averaged density and in the soft X-ray emission level have been observed. The typical density increase is about 20% within 600 μs. Some signatures of confinement improvement of the STOR-M plasma induced by vertical CT injection have also been observed.

Acknowledgements

I would like to express my deepest thanks to my supervisor, Prof. A. Hirose, for being the chief motivator and providing timely guides and support during all phases of this thesis. Without him this work would not have been possible.

I especially thank Prof. C. Xiao for his friendship and many insightful discussions. His untiring willingness to teach and encourage me made the whole course of this thesis work highly enjoyable. His dedication to high quality experimental plasma physics research has been a great inspiration. I am especially fortunate to have witnessed Prof. Xiao's talent for identifying important research problems and solving technical problems.

I am also indebted to Dr. A.K. Singh and Dr. T. Asai for their expertise and lots of immediate help whenever needed.

I would also like to thank my fellow graduate students Steeve Livingstone, Weifeng Chen and Jordan Morelli for providing a friendly atmosphere in which to work and relax. Many thanks go out to David McColl for his friendship and kind assistance with all the hardware of this work. The Physics Machine Shop (Perry Balon, Blair Chomyshen and Ted Toporowski) deserves a note of thanks for their assistance whenever needed.

Finally, I would like to thank my wife, Minhui for her patience and love throughout the tenure of my work on this thesis.

This work was supported by the grants from the Natural Sciences and Engineering Research Council of Canada and through financial aid from the University of Saskatchewan Graduate Scholarship and the Alex Kavadas Memorial Scholarship.

Dedicated to my parents.

Table of Contents

List of Tables

List of Figures

List of Symbols

1. This list of symbols aims to explain the meaning of the symbols in the text.

2. Vector quantities are denoted by bold face.

Operators

∇	Gradient operator

Latin symbols

a, R	Tokamak minor and major radius
A	Collection area of probe tip
$\mathbf{A}_\phi$	Magnetic vector potential
$\mathbf{B}$	Magnetic flux intensity
B_r, B_ϕ, B_z	Magnetic field of CT in r, ϕ, z coordinates where r, ϕ and z are radial, toroidal, and poloidal coordinates respectively.
B_0	Normalized CT magnetic field strength
B_{CT}	CT magnetic field strength
$\mathbf{B}_{ext}$	External magnetic field
$\mathbf{B}_t$	Tokamak toroidal magnetic field
B_θ	Magnetic field produced by the radial discharge current for CT acceleration
C_{acc}	Capacitance of the CT acceleration circuit
D-T	Deuterium-Tritium
e	Electron charge
E	Energy
E_i	Ionization energy
$\mathbf{E}$	Electric field
$\mathbf{E}_y$	Electric field along the y direction
FB	Coils for feedback plasma position control in STOR-M
$\mathbf{F}_{drag}$	Force due to Alfvén wave drag
I	Current
I_{acc}	CT acceleration bank discharge current
I_{form}	CT formation bank discharge current
I_{gun}	Gun current of the CT injector
I_p	Plasma current
I_{sat}	Ion saturation current
I_t	Toroidal current in CT plasma
j_0	Axial current density in a tokamak
J	Current density
$\mathbf{J}_{gun}$	Gun current density of the CT injector
$\mathbf{J}_r$	Radial current density

$J_m(x)$	Bessel function of the first kind of order m
l	Characteristic distance
L	Inductance
$L^{'}$	Inductance per unit length in the CT acceleration circuit
L_{ext}	External inductance of the CT acceleration circuit
L_t	Total inductance of the CT acceleration circuit
L_{fc}	Length of a flux conserver
L_p	CT translation distance between the end of acceleration and the center of tokamak chamber
L-H	Transition from Low confinement mode to High confinement mode
K_{CT}	CT kinetic energy density
k_r, k_z	Radial and poloidal wave number of the CT magnetic field
m	MHD mode number
$\mathbf{m}$	Dipole moment of a CT
m_{CT}	Mass of a CT
m_e, m_i	Electron and ion mass
N	Number of turns making up a coil
n_c	Cutoff density
n_{CT}	Electron density of a CT
$\bar{n}_e$	Line averaged electron density
n_e, n_i	Electron and ion density
OH	Ohmic primary coils in STOR-M
P	Pressure
q	Safety factor
q_0	The axial value of q
Q	The ratio of fusion power to input auxiliary heating power
r	Radial coordinate in a tokamak
r_{in}, r_{out}	Inner and outer radius of coaxial electrodes for CT acceleration
r_{CT}	CT radius
r_L	Larmor radius
R_c	Resistance of the CT acceleration circuit
Re_{mag}	Magnetic Reynolds number
R_{fc}	Radius of a flux conserver
t_{tilt}	Tilt time for CT to align its dipole moment with the external magnetic field
T	Tesla
T_e, T_i	Electron and ion temperature
$U_{\nabla B}$	Work done to exclude tokamak magnetic field lines in CT penetration
$v_\perp$	Velocity component perpendicular to the magnetic field
$v_\parallel$	Velocity component along the magnetic field
V	Volt
V_{acc}	CT acceleration bank voltage
V_A	Alfvén velocity
$V_{A,tok}$	Alfvén velocity in tokamak plasma

V_{CT}	CT velocity
VE	Vertical equilibrium field coils in STOR-M
V_f	Floating potential
V_l	Loop voltage
V_s	Plasma space potential
z	Axial distance in CT trajectory
Z	Charge number
Z_i	Ion charge number
Z_{eff}	Effective ion charge number

Greek symbols

α	Random coefficient for the first order in the description of λ in terms of Ψ
β	The ratio of plasma pressure to magnetic pressure
γ	Random coefficient for the second order in the description of λ in terms of Ψ
λ	Eigenvalue of CT magnetic filed in force-free state
λ_c	Critical λ value for CT formation
$\bar{\lambda}$	Average λ value over the flux conserver radius
δ	Wall thickness
δ_{gap}	Radial distance between the inner and outer coaxial electrodes in the CT formation region
ϕ	Toroidal coordinate in a tokamak
Ψ_{bias}	Stuffing magnetic flux
τ_E	Energy confinement time
τ_{CT}	Magnetic field decay time of a CT
τ_{comp}	CT compression time
$\tau_{A,CT}$	Alfvén time for CT plasma
τ_{decay}	Decay time of CT magnetic field
τ_{life}	CT lifetime
τ_p	CT translation time
τ_R	Resistive decay time
τ_{RC}	Time constant of RC integator
τ_{rec}	Magnetic reconnection time
ρ_{CT}	CT mass density
ρ_{tok}	Tokamak plasma mass density
Ψ	Poloidal magnetic flux coordinate for a CT
Ψ_{max}	Maximum of Ψ, it occurs at the magnetic axial of CT
μ_0	Permeability of free-space
η	Classical Spitzer resistivity of CT plasma
ω_c	Cyclotron frequency
$\Delta\phi$	Phase shift
ΔH	Plasma horizontal displacement
ϵ_0	Permittivity of free-space

Chapter 1

Introduction

In a fusion reactor, most fusion reactions take place in the plasma core region where both the plasma density and temperature are peaked. Therefore, central fuelling is a crucial issue for successful development of magnetic fusion reactors. At present the leading candidate for a magnetic confinement fusion reactor is the *tokamak*, a Russian word standing for *"toroidal'naya kamera v magnitnykh katushkakh"* - toroidal chamber in magnetic coils. As the tokamak size increases, fuel deposition at the plasma core is becoming increasingly difficult because of premature ablation and/or ionization by high density, high temperature plasma. Although injection of cryogenic pellets of fusion fuels is considered to be the leading candidate for a fuelling method for large tokamaks in the future, even in present tokamaks pellet fuelling has been observed to face difficulties in penetration. This has recently been recognized at an International Energy Agency (IEA) Workshop [1] and the expert panel recommended that novel methods for core fuelling be explored, with particular emphasis on compact torus injection.

Besides supplying sufficient fusion fuels, it would be advantageous for tokamak operation if fuelling can also control the plasma pressure profile through selective fuel deposition at different magnetic surfaces. This is because in tokamaks, a large fraction of the toroidal current can be self-induced as the bootstrap current which is proportional to the pressure gradient of trapped particles [2, 3]. In addition, it must be done as often as required to minimize density perturbation due to fuelling. Conventional fuelling methods cannot meet these requirements. For example, pellet injection in present tokamaks causes density perturbation as large as 50% which is unacceptably large for steady-state operation of fusion reactors.

A Compact Torus (CT) is a high density, self-contained magnetized plasma structure. Compact torus injection as a means to centrally fuel a reactor-grade tokamak was proposed by Parks [4] and Perkins *et al*. [5] in 1988. Since then, active research has been pursued to validate its feasibility and to study the interaction between the CT and the tokamak plasma. The first disruption free injection experiment was performed by Raman *et al*. on TdeV [6]. CT injection into H-mode plasmas has been performed on the JFT-2M tokamak [7]. In the Plasma Physics Laboratory (PPL) at the University of Saskatchewan, a CT project was initiated by constructing a CT injector (USCTI) for the Saskatchewan Torus-Modified (STOR-M) tokamak. H-mode like discharges in STOR-M induced by tangential CT injection have been observed for the first time [8]. Currently, STOR-M is the only tokamak in the world equipped with a CT injector.

As the attractiveness of CT injection as a means to fuel large tokamak reactors is recognized, further improvements in the CT injection technology are in order. In CT fuelling, a CT has to penetrate through a high magnetic field and it is important to determine if there is an optimum injection angle relative to the toroidal magnetic field for deepest penetration. Furthermore, in CT injection, two high density plasmas (CT and tokamak) merge through magnetic reconnection. Detailed studies on this basic physical process, which necessarily involves an anomalous resistivity, are actively pursued.

In this thesis, results of experimental study on vertical compact torus injection into the STOR-M tokamak are presented. Different from conventional radial and horizontal injection, a unique injection angle was adopted. The CT was injected perpendicular to the STOR-M mid-plane. Since there is no gradient of the tokamak toroidal magnetic field in the vertical direction, deeper CT penetration is expected in vertical injection. To perform vertical injection in STOR-M, USCTI was modified by attaching a segment of 90° curved drift tube to deflect CT injection direction from horizontal to vertical.

This introductory Chapter will begin with a brief introduction to nuclear fusion and the tokamak concept which has been the most successful among various

schemes proposed in the past. Tokamak fuelling techniques currently available will be reviewed in Section 1.3. Previous work on CT injection, both theoretical and experimental, will be reviewed in Section 1.4. The motivation for this research will be addressed in Section 1.5. The major findings and outline of this thesis will be given in Sections 1.6 and 1.7.

1.1 Nuclear fusion

At the beginning of the twenty-first century mankind is faced with the serious problem of meeting the energy demands of a rapidly industrializing population around the world. Even in an optimistic scenario of world population saturated at 10 billion, severe energy shortage will occur unless the moratorium of nuclear energy is lifted. Fossil fuels may continue to be abundantly available but their uses will be much restricted because of green-house gas emission. Thermonuclear fusion has a potential of becoming the long term environmentally friendly energy source because of its (1) virtually inexhaustible and universally available fuel source; (2) intrinsically safe nature (no chain reaction); (3) right energy density for large scale production of electricity; and (4) acceptable environmental impact from the operational and waste points of view [9].

In a nuclear fusion reaction, two light nuclei merge, forming a heavier nucleus and releasing the energy corresponding to the mass deficiency before and after reaction. There are several fusion reactions that can be considered for energy production. The deuterium-tritium (D-T) reaction is the most promising one because of its large cross-section at relatively low temperatures [10]:

$$ {}_1\mathrm{D}^2 + {}_1\mathrm{T}^3 \rightarrow {}_2\mathrm{He}^4(3.50\,\mathrm{MeV}) + {}_0\mathrm{n}^1(14.1\,\mathrm{MeV}). \tag{1.1} $$

Deuterium is found naturally in sea water (abundance 1 part in 6000). Tritium has a half-life of 12.3 years and does not occur naturally, but can be bred from the vast deposits of lithium which exist in the Earth's crust and oceans. Nuclear fusion requires that fusion fuels be heated to high temperature to overcome Coulomb

repulsion. In the case of D-T fusion, a temperature in the range between 10 and 20 keV (i.e. between 100 and 200 million degrees centigrade) is necessary to realize the reaction as shown in Eq. (1.1).

D-T fusion produces a neutron with an energy of 14.1 MeV and a He (alpha) particle with an energy of 3.5 MeV. The alpha particles remain confined in the plasma and deposit energy back to the main D-T fuel. The neutrons produced in the D-T reactions are absorbed by a blanket which act as a tritium breeder and also as a heat exchanger. Tritium production in the blanket is based on the following reaction,

$$\mathrm{Li}^6 + \mathrm{n} \rightarrow \mathrm{T} + \mathrm{He}^4. \tag{1.2}$$

Coolants circulating within the blanket and the plasma facing components transfer the heat out of the reactor area to produce steam and to generate electricity in the conventional way. A fusion based power plant is illustrated in Figure 1.1.

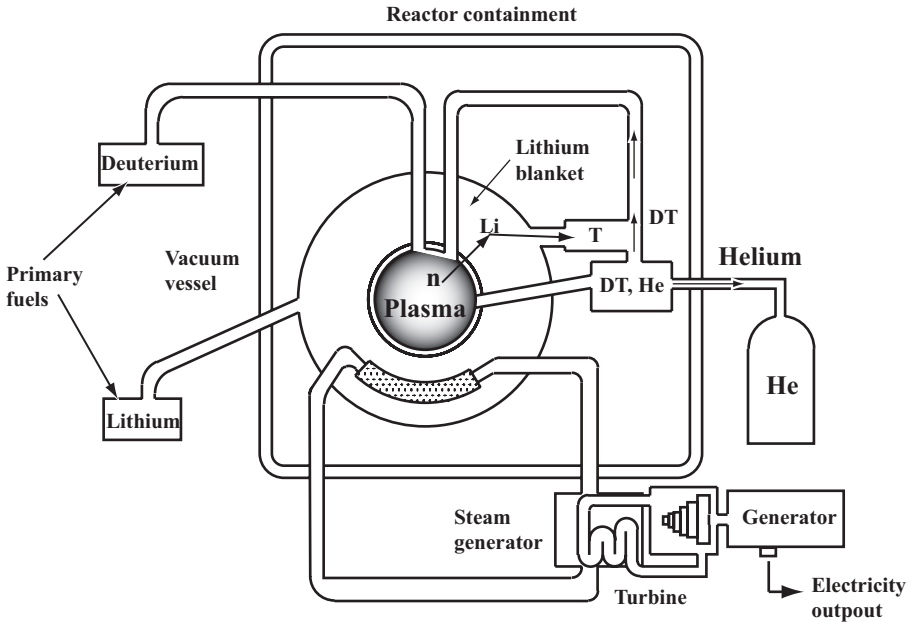

Figure 1.1: Schematic diagram of a D-T fusion power plant, from IFRC [9].

An important parameter for a fusion based power plant is Q, which is defined as the ratio of fusion power to external heating power. If the temperature of a D-T plasma was continuously increased by external heating, a point would be reached

where the alpha particle heating balances the power losses. The plasma would then ignite and the external heating could be removed. The objective of ITER [9] is to demonstrate a burning plasma in which plasma heating by alpha particles maintains the high fuel temperature required by fusion reactions. In ITER , $Q \geq 10$ is envisaged.

To indicate how close a plasma is to 'reactor conditions', a parameter called the triple product $nT_i\tau_E$ is used. It is the product of density (n), the ion temperature (T_i) and the energy confinement time (τ_E). In order to achieve ignition ($Q = \infty$) in a 50-50 D-T plasma, a temperature close to 30 keV is needed and the condition on the fusion triple product is [10]:

$$n_{DT}T_i\tau_E > 5 \times 10^{21} \text{ m}^{-3} \cdot \text{keV} \cdot \text{s} \tag{1.3}$$

1.2 Magnetic confinement and tokamaks

At a temperature required for fusion reactions, the fuels become fully ionized and form a *plasma*. Charged particles can be confined by a suitable magnetic field. It is well known that charged particles follow magnetic field lines by spiraling around them with an orbital frequency known as the cyclotron frequency given by [11]:

$$\omega_c = \frac{|q|B}{m}, \tag{1.4}$$

where q is the charge of the particle, m is its mass, and B is the magnitude of the magnetic field. Furthermore, the orbital radius of a particle about its guiding center, commonly referred to as the Larmor radius, is given by [11]:

$$r_L = \frac{v_\perp}{\omega_c} = \frac{mv_\perp}{|q|B}, \tag{1.5}$$

where $v_\perp$ is the velocity component of the particle perpendicular to the magnetic field. Magnetic confinement fusion exploits the ability of a steady magnetic field to restrain the motion of the charged particles in a plasma across the magnetic field.

One way of trapping the particles along the field lines is by closing the field lines in the form of a torus. However, a simple toroidal field alone cannot confine a plasma

because the magnetic surfaces are not closed. Simple toroidal magnetic field causes two particle drifts, the curvature and gradient drifts, given by [11]:

$$\mathbf{V}_R + \mathbf{V}_{\nabla B} = \frac{m}{q}\frac{\mathbf{R}_c \times \mathbf{B}}{R_c^2 B^2}\left(v_\parallel^2 + \frac{1}{2}v_\perp^2\right), \tag{1.6}$$

where $\mathbf{V}_R$ is the curvature drift velocity, $\mathbf{V}_{\nabla B}$ is the gradient drift velocity, m is the particle mass, $\mathbf{R_c}$ is the radius of curvature of the magnetic field, $\mathbf{B}$ is the magnetic field, $v_\parallel$ is the velocity component of the particle parallel to the magnetic field and $v_\perp$ is the velocity component of the particle perpendicular to the magnetic field. The magnetic drifts of ions and electrons are in opposite directions, as shown in Figure 1.2, which causes a vertical charge separation. An electric field created by the charge separation causes $\mathbf{E} \times \mathbf{B}$ drift [11],

$$\mathbf{v_{E\times B}} = \frac{\mathbf{E} \times \mathbf{B}}{B^2}, \tag{1.7}$$

which is charge insensitive and radially outward. This drift causes particles to drift towards the outer wall, and the plasma is not confined. This can be seen schematically in Figure 1.2.

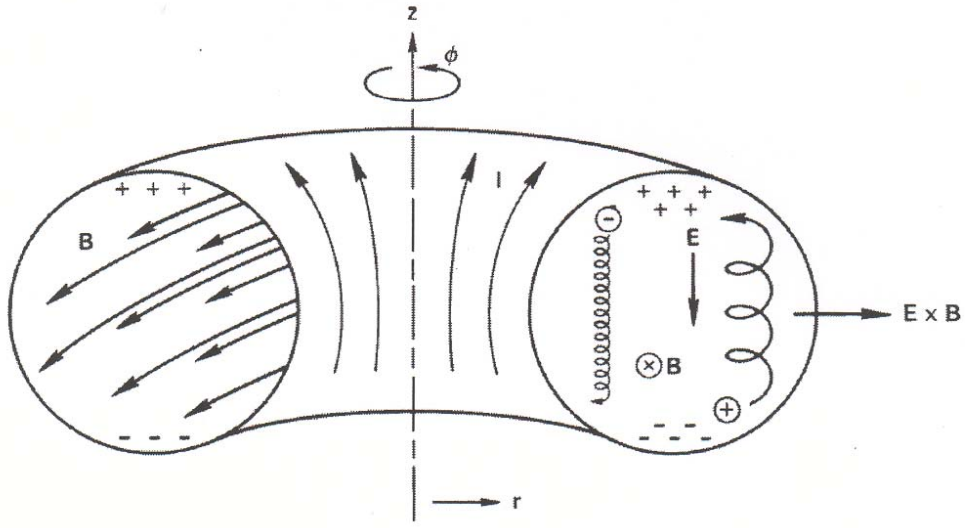

Figure 1.2: Particle motion in a toroidal field. The particles are pushed outward due to the $\mathbf{E} \times \mathbf{B}$ drift caused by charge separation, from Chen [11].

To prevent the build up of the electric field, one needs an additional component of magnetic field, the poloidal magnetic field, to form closed magnetic surfaces. This

leads to the concept of rotational transform. The resulting magnetic field lines become helical. Since the magnetic surfaces are nested, the hot plasma in the core is thermally insulated from the colder plasma near the edge, and a charged particle can move across a magnetic field only by collisions with other charged particles or through turbulence.

In tokamaks, the required rotational transform is realized by the poloidal magnetic field, generated by a toroidal current flowing in the plasma itself [10, 11]. The resultant magnetic field becomes helical and closed magnetic surfaces are formed. Figure 1.3 illustrates a schematic of a tokamak.

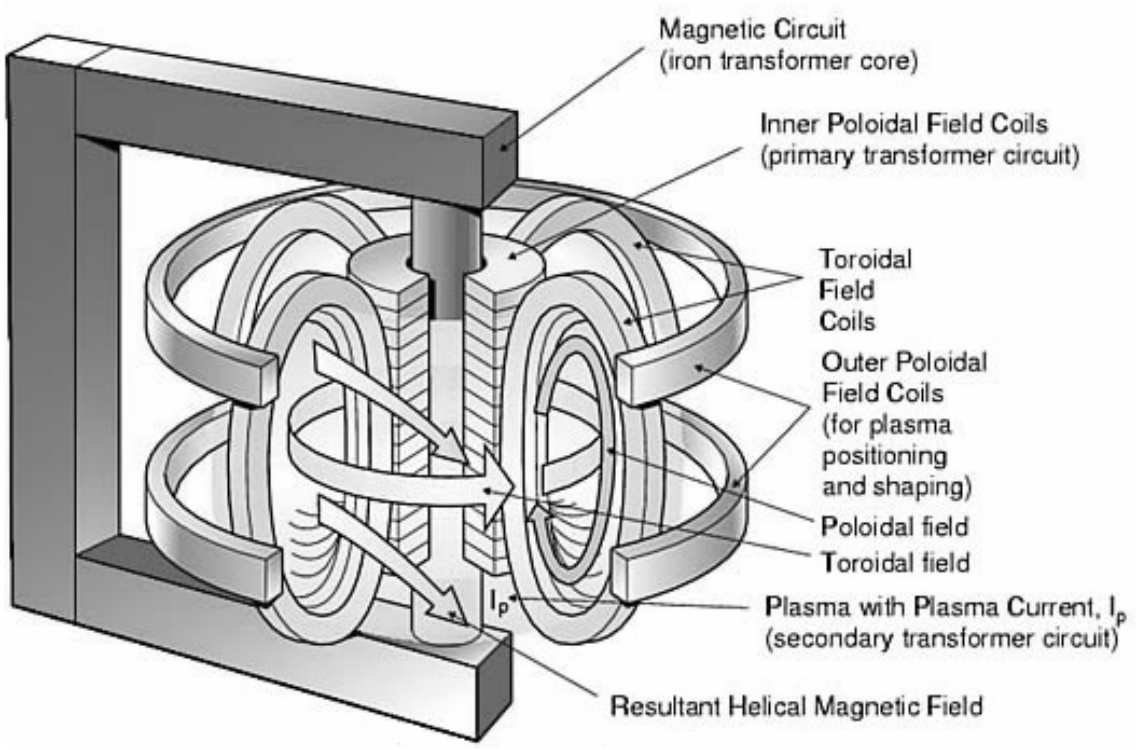

Figure 1.3: Schematic of a tokamak showing the resultant helical magnetic field by toroidal and poloidal magnetic field, field coils and plasma current.

Tokamaks have registered impressive progress in key areas of reactor relevance in the last ten to fifteen years. Significant improvement in reduced transport, operating density and stability of the tokamak plasma have been achieved in this period. In

present day tokamak experiments the fusion triple product has reached record values of $1.5 \times 10^{21}\,\mathrm{m}^{-3} \cdot \mathrm{keV} \cdot \mathrm{s}$ ($n_D(0) = 4.9 \times 10^{19}\,\mathrm{m}^{-3}$, $T_i(0) = 16.5\,\mathrm{keV}$, and $\tau_E = 0.97$ s, where "(0)" denotes the plasma parameter in the core region) in JT-60U [13]. Up to 16 MW of fusion power has been produced for several seconds in JET [14]. Fusion experiments have brought this critical parameter within a factor of 3-5 of the required value and have already exceeded conditions equivalent to a Q =1 operating power plant. Figure 1.4 illustrates the impressive progress road map in tokamak experiments toward the development of fusion as an energy source.

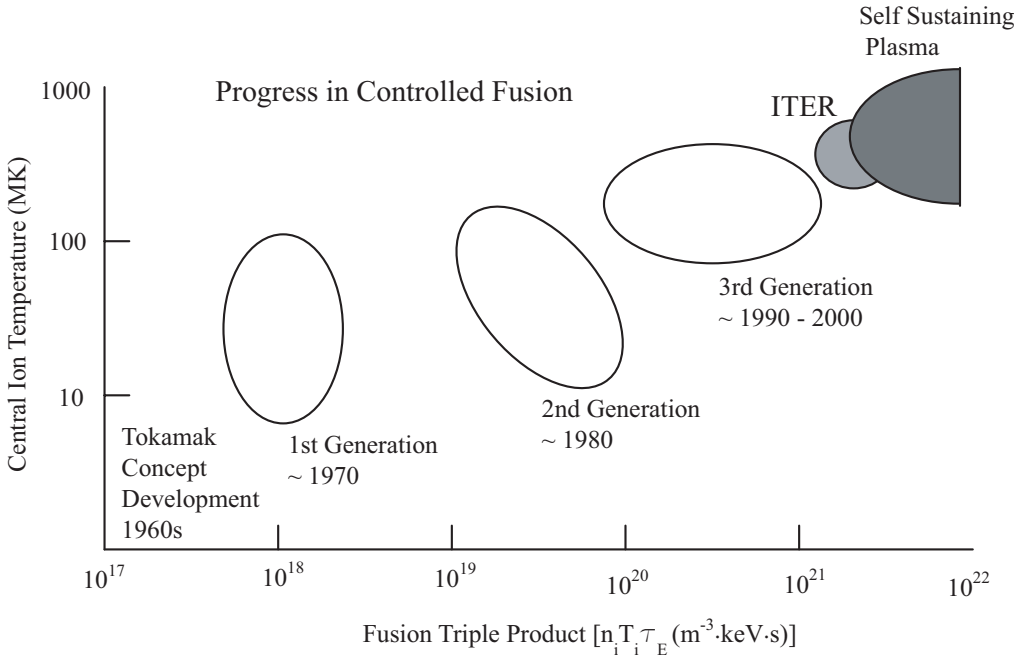

Figure 1.4: Progress of the achieved central ion temperature and fusion triple product, from IFRC [9].

1.3 Tokamak fuelling

As the tokamak size increases, fuelling the core, where fusion reactions are most active, becomes more difficult. For example, in pellet fuelling, the density perturbation observed in present tokamaks is as large as 50% which is not acceptable for steady state operation of fusion reactors. The pellet size has to be large to survive ablation and ionization before reaching the core. There is a technical limit to the pellet

velocity as well. It appears that a pellet injected from the low magnetic field side (LFS) has to overcome the force due to the gradient in the magnetic field. Injecting from the high field side (HFS) has been tested on ASDEX [15]. However, localized fuel deposition is difficult.

The direct fuelling of the core of a fusion tokamak has several advantages. It leads to peaked plasma density profile which is beneficial to plasma confinement. Central fuelling is desirable for optimization of the bootstrap current which is proportional to the pressure gradient of trapped particles. Meanwhile, parametric study of the ITER operating regime has shown that a centrally peaked density profile can lower the ignition parameter and the plasma pressure required for ignition [16, 17].

1.3.1 Conventional fuelling techniques

The conventional tokamak fuelling techniques include gas puffing, neutral beam injection, and cryogenic pellet injection. In gas puffing, fuels are puffed at the tokamak edge using fast valves. Gas puffing is inexpensive and reliable but of low efficiency. Gas puffing will be inadequate to fuel reactor size tokamaks. Fuelling by NBI (neutral beam injection) is inefficient and inadequate particularly when core fuelling is required.

An interesting core fuelling mechanism based on turbulence induced particle pinch has been proposed [18]. If the temperature profile is steeper than the density profile, particles are transported toward higher density region according to quasilinear estimates in temperature gradient driven instabilities. However, recent numerical simulations do not support the simplistic quasilinear estimates [19].

Pellet injection [20-24] has demonstrated efficient core plasma fuelling in a number of present day tokamaks and is the primary fuelling technique planned for core fuelling of the ITER burning plasma. Efficient core fuelling in ITER with D-T cannot be achieved with gas puffing alone. Experiment on the DIII-D tokamak [20] has shown that injection of pellets from the high field side (HFS) provides efficient fuelling and is therefore planned to be implemented on ITER. However, it was found that the pellet speed was limited to $\sim 0.3\,\mathrm{kms}^{-1}$ for reliable delivery of pellets because

of insufficient inertial strength. These velocities are much lower than the required value of $2 \sim 3\,\mathrm{kms}^{-1}$ for central fuelling of ITER plasma from the HFS using pellet injection.

1.3.2 Compact torus injection

Compact torus (CT) injection is considered a promising approach which has potential to centrally fuel a reactor-grade tokamak. CT fuelling involves injecting a compact self-contained plasma torus at a high velocity. A compact torus is a small, stable plasma configuration with embedded magnetic fields [25]. It is formed in a magnetized plasma gun and subsequently accelerated using a rail gun. An accelerated CT is able to penetrate into the core region and deposit fuel there provided the CT kinetic energy density exceeds the magnetic energy density in the target plasma. From the point of view of fuelling economics, the energy required per injected fuel particle by CT injection is in the order of 100 eV for fuelling ITER plasma, which is two orders of magnitude lower than fuelling by neutral beam injection.

This method has two features that make it attractive. Firstly, a CT is good conductor on the penetration time scale (several μs) and the primary stopping mechanism is that the CT slows down due to the tokamak toroidal magnetic field gradient. The process is complicated and involves magnetic reconnection [25] and excitation of plasma waves [26]. Secondly, the CT formation and acceleration schemes are electrical, allowing themselves to be operated in a repetitive mode. This is crucial for fuelling next generation fusion reactors operated in steady state. The technology for CT formation and acceleration has been well-established. For example, CT velocity up to 2000 kms^{-1} has been achieved in RACE [32]. The proof-of-principle experiments on tokamak fuelling by CT injection have been conducted in TdeV [6] and JFT-2M tokamaks [7].

1.3.3 Plasma jet injection

Plasma jet injection [27, 28] is an emerging tokamak fuelling method which has been recently tested on the Globus-M spherical tokamak (major radius $R = 36$ cm, minor radius $a = 24$ cm, toroidal magnetic field $B_t = 0.2$-0.5 T) [29, 30]. The fuelling process by plasma jet injection is similar to CT injection. The difference lies in injecting a bulky, dense, plasma jet rather than a well confined plasma torus. The plasma jet has typical parameters of $\sim 10^{22}\,\mathrm{m}^{-3}$ in density and $\sim 50 - 100\,\mathrm{kms}^{-1}$ in velocity. A compact and dense plasma jet is formed and subsequently accelerated in the classical "Marshall gun" scenario. So far, this approach was only demonstrated on the Globus-M tokamak. It has not been verified whether plasma jet injection can penetrate into a large sized tokamak plasma.

1.4 Previous work on CT injection

Compact torus injection as a means to centrally fuel a reactor-grade tokamak was proposed by Parks and Perkins *et al.* in 1988 [4, 5]. In their work the CT penetration, slowing down and reconnection process of a CT penetration into a tokamak plasma were theoretically studied. The fundamental criterion for CT penetration was that the CT should have sufficient kinetic energy density to exceed the magnetic energy density in a tokamak so that the magnetic field lines could be pushed aside by CT. Since then, active research has been carried out to validate feasibility and to study the interaction between the CT and the tokamak plasma.

The early experiments on acceleration and focusing of magnetically confined plasma ring were conducted in the LLNL Ring Accelerator Experiment (RACE) project in 1988 [31-33]. In this experiment the CT accelerator concept was developed in order to increase the CT velocity. The approach was to use the first stage of 1.5 m diameter, puffed gas, magnetic field embedded coaxial plasma gun discharge to form a CT. The second stage discharge was used to compress and to accelerate the CT by $\mathbf{J} \times \mathbf{B}$ forces. Conical electrodes were at the exit of the accelerator to

focus CT. The initial experiments showed that CT velocity reached a value of 400 kms^{-1} and kinetic energy reached a value of ≈ 40 kJ (out of 100 kJ of accelerator bank energy). After optimization of the accelerator operation which included using tantalum liners on the gun and accelerator electrodes and glow discharge cleaning, electrode contributions to the CT mass had been significantly reduced, resulting in acceleration up to about $2500\,\mathrm{kms}^{-1}$. The CT plasma kept its integrity while undergoing acceleration. Field amplification was also observed after the CT passed the focusing exit. This proof-of-principle experiment provided the technical basis of tokamak fuelling by CT. Core penetration might be achieved provided the CT gained sufficient kinetic energy in CT accelerator.

The first tokamak fuelling by CT was performed on Caltech's ENCORE tokamak ($R = 0.38\,\mathrm{m}, a = 0.12\,\mathrm{m}, B_t = 0.07\,\mathrm{T}$) in 1992 [34, 35]. The CT with $n_{CT} = 10^{21}\,\mathrm{m}^{-3}$ and $V_{CT} = 30\,\mathrm{kms}^{-1}$ was injected by a magnetized coaxial plasma gun. The tokamak density profile peaked sharply because of the injected CT plasma ($\bar{n}_e$ increased by a factor of six). In addition, an interesting phenomena observed in this experiment was the identification of tokamak current drive by CT injection. The typical increase in current is 30%. The underlining mechanism was attributed to the process of helicity injection. However, the discharges of the ENCORE tokamak were always disrupted by the CT injection.

The first disruption-free CT injection experiment was performed in 1994 on the TdeV tokamak, a medium sized tokamak with major radius $R = 0.86$ m, $a = 0.25$ m and toroidal field $B_t = 1.4$ T [6, 36]. The CT injector CTF (Compact Toroid Fuller) was fabricated in PPL at the University of Saskatchewan. In these experiments, CTs were injected into a deuterium plasma. Following the CT injection, the tokamak particle inventory increased by 16%. The CT particle inventory was $\sim 1.1 \times 10^{19}$, whereas the increase in the tokamak particle inventory is $\sim 3.3 \times 10^{18}$ implying a CT fuelling efficiency of about 30%. Interferometer measurements showed that a rapid increase in density occurred at the core ($r/a = 0.1$). No adverse effects on tokamak plasma parameters were observed following CT injection. The plasma diamagnetic energy and the energy confinement time increased by more than

35%. Global tokamak parameters such as plasma current and loop voltage were not perturbed and there was no enhancement in MHD activity following CT injection. This was the first demonstration of central fuelling of a mid-sized tokamak by CT injection.

In the STOR-M tokamak, along with electrode biasing and turbulent heating, H-mode like discharges have been induced by tangential CT injection [8, 37-38]. The CTs produced in USCTI with a typical velocity $\sim 150\,\mathrm{kms}^{-1}$, and $\bar{n}_e \sim (1-4) \times 10^{21}\,\mathrm{m}^{-3}$ were injected in the direction at a 27° angle with the normal local radial direction. Interesting phenomena, characterized by doubling line averaged electron density, plasma position radially outwards movement, suppression of MHD fluctuations and drop in H_α emission level, have been observed following CT injection. The mechanism of H-mode triggering was likely because of the interaction of CT plasma with the edge plasma of STOR-M, resulting in stabilization of the dissipative drift ballooning modes [8, 37].

CT injection into H-mode plasma discharge has been performed on the JFT-2M tokamak ($R = 1.31\,\mathrm{m}, a = 0.35\,\mathrm{m}, B_t = 1\,\mathrm{T}$) [7, 39-40]. Reflection of CTs by the JFT-2M toroidal field was observed in the experiments. Recent experimental results [41] demonstrated a fast increase in density up to $1.3{\times}10^{22}\,\mathrm{m}^{-3}\mathrm{s}^{-1}$ caused by CT injection after upgrade of the CT injector. The injected CT reached the core region of the tokamak. A magnetic fluctuation with the spectral peak at 250-350 KHz was observed following the CT injection. The fluctuation propagated in the toroidal direction at the Alfvén velocity of the order of $10^6\,\mathrm{ms}^{-1}$ and was identified as an Alfvén wave [41-42]. In addition, the experimental results suggested that CT injection induced H-mode like discharges which were characterized by the increase in the soft x-ray emission level, suppression of the ion saturation current fluctuation and drop of D_α emission at the divertor region.

Along with the progress in CT injection experiments, considerable efforts have been made to design and construct CT injectors to fulfill various experimental objectives, such as MARAUDER [43-44], CTF [45], Caltech CT injector [46], CTIX [47-48] and HIT-CTI MARK III [49]. The technical issues include mechanical configuration,

impurity control, power supply, fuel handling and shielding of electromagnetic impulse [50]. Sputtering and arcing can release atoms which contaminate the CT due to CTs being in contact with metal walls during their formation and acceleration. The primary impurities are carbon and oxygen trapped in the walls, and metals from erosion of electrodes. These impurities can be eliminated by coating the electrodes with tungsten or chromium, by baking the electrodes, by using oil-free vacuum pumps, and by repetitively pulsing the injector prior to operation in order to condition the surfaces. The CT injector impurity control technique and the optimization of CT injector discharge are crucial to conduct quality injection experiments. The CT kinetic energy density can be significantly improved by performing the optimization process, resulting in increases of CT velocity, lifetime and confinement field strength.

Moreover, care must be taken to choose the proper drift tube configuration. A drift tube is used to connect a CT injector with a tokamak port. The experiments performed by J. Yee *et al*. showed that the larger diameter of the drift tube is more beneficial for CT penetration into tokamak magnetic fields [51]. CT acceleration in the coaxial electrodes was studied in the CTIX injector. The "blow-by" effect, which means the velocity saturates when increasing the acceleration voltage, was identified [47, 52]. In addition, CT translation in a curved drift tube was studied with HIT-CTI [53]. A 90° flux conserving drift tube was used to deflect the CT trajectory from horizontal to vertical. The objective was to achieve injection of a CT perpendicular to the tokamak toroidal field to optimize CT penetration. In the experiments, the curved drift tube did not degrade the CT magnetic field and slow down the CT. In the experiments, the CT velocity was $40\,\mathrm{kms}^{-1}$ which is low compared with the normal speed in CT injection experiments.

Theoretical simulation work has also been made to investigate CT-tokamak interaction [54-57]. Various injection angles, such as radial, vertical and tangential were examined to optimize the CT penetration in the tokamak magnetic field. The Alfvén wave excitation by CT injection was predicted by Newcomb as another braking mechanism in CT penetration [26].

1.5 Motivation and objectives

Compact torus injection was proposed as a means to fuel a reactor-size tokamak. A significant amount of theoretical and experimental work has been carried out on several moderate-size tokamaks to study various physics issues related with CT injection, e.g. central fuelling, H-mode triggering and CT translation dynamics. The common feature of these experiments is that CTs are injected in the horizontal direction, from the outer board of a tokamak (low field side). In this case, the injected CT is decelerated by the retarding force due to the gradient of the tokamak magnetic field. It is conjectured that a vertically injected CT (as shown in Figure 1.5) is expected to penetrate deeper due to the absence of the retarding force along its penetration. Therefore, a higher fuelling efficiency would be achieved in vertical injection. Simulation work [56-57] has suggested that deeper penetration can be achieved by vertical injection. Experimental investigations on vertical CT injection into a tokamak will be of great significance.

Experimental investigation on vertical injection of CTs into the STOR-M tokamak was proposed. The objectives are as follows:

(1) Modify the original USCTI to allow vertical injection,

(2) Bench test the CT deflector,

(3) Perform vertical injection into the STOR-M tokamak.

1.6 Major findings

The original USCTI has been modified to perform vertical injection. The modifications included adding a segment of a 90° flux conserving drift tube and a compressor to the exit of the acceleration section. Bench test of CT translation in the 90° curved drift tube was carried out. Magnetic probe and H_α emission measurements were used to characterize the CT plasma parameters. The test results have confirmed that CTs injected horizontally into the bend can be deflected to the vertical direction. In addition, the experiments extended the CT velocities passing through the

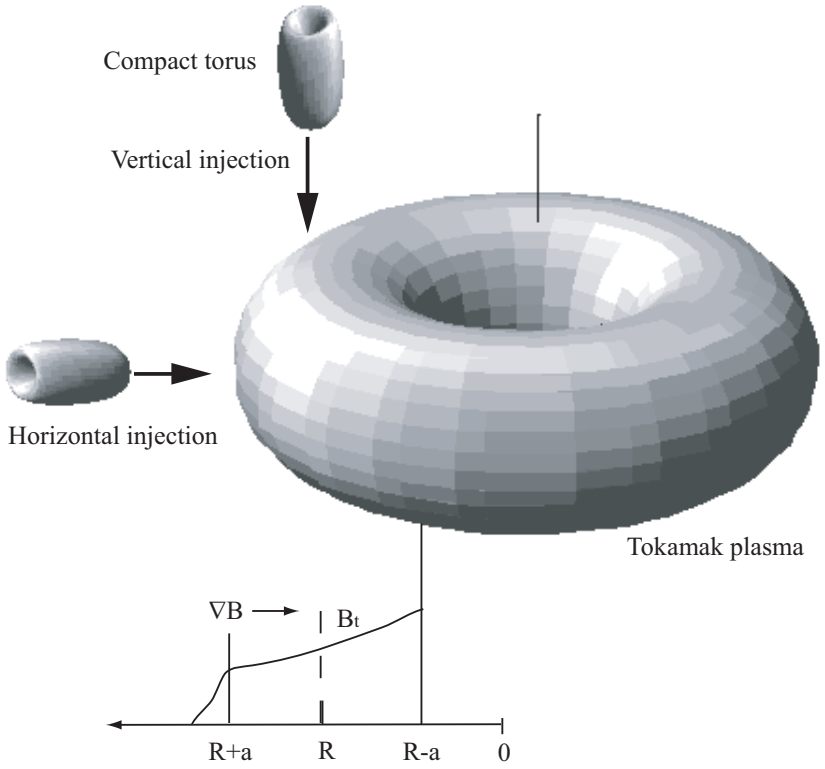

Figure 1.5: Horizontal and vertical CT injection for tokamak fuelling.

90° bending drift tube from 40 kms^{-1} in Fukumoto's experiments [53] to 130 kms^{-1}. At this speed, the magnetic probe measurements showed that the CT magnetic field structure kept intact as a typical structure for a compact torus plasma. By further optimization of the USCTI configuration, this value has been increased to 270 kms^{-1}. The H_α emission measurement showed that the CT can reach the distance as far as the traveling distance in the actual vertical injection. In addition, a one-dimensional point model was employed to study the CT acceleration dynamics in the modified acceleration region under the conditions of the USCTI working parameters. The numerical results agreed well with the experimental measurements.

Based on the bench test results, actual vertical CT injection experiments have been carried out, for the first time, in the STOR-M tokamak. The modified USCTI was connected to a vertical port of the STOR-M tokamak. Under the USCTI discharge condition: $V_{form} = 18$ kV and $V_{acc} = 14$ kV, disruption-free discharges have been achieved with the vertical CT injection. A prompt increase in the line averaged

electron density, an increase in soft X-rays emission (center chord) and suppression of the $m = 2$ Mirnov oscillation level have been observed following the vertical injection. The typical density increase is 20% within 600 μs. This work explored tokamak fuelling by CT injection at a unique injection angle. Vertical injection will be a feasible technique for fuelling large-size tokamaks.

1.7 Outline of thesis

A brief introduction to nuclear fusion, tokamak concept, current tokamak fuelling schemes and a review of previous work on CT injection has been given in this Chapter. The rest of this thesis is organized as follows:

- Chapter 2 presents the basic physics on tokamaks, including plasma equilibrium, magnetic field components, tokamak confinement and plasma heating.

- Chapter 3 is dedicated to describe the physics involved in CT injection. The magnetic field structure of CT is described. Detailed physical processes of CT injection and CT-tokamak interaction are discussed.

- Chapter 4 is devoted to a detailed description of the experimental hardware, the USCTI CT injector and the STOR-M tokamak. Major diagnostic tools for CT and tokamak plasma are presented in detail.

- In chapter 5, the modifications of the original USCTI to allow vertical injection are presented. The CT deflection experiments were carried out under two different configurations. Chapter 5 includes the CT deflector design and the bench test results.

- Chapter 6 presents the results of actual vertical injection into STOR-M plasma. The Behavior of STOR-M plasma following vertical injection is analyzed. Comparison in density changes between tangential and vertical injection was conducted.

- In Chapter 7, the conclusions of this work are given and suggestions of future work are presented.

Chapter 2

Tokamak basics

2.1 Tokamak equilibrium

The MHD (magnetohydrodynamics) equilibrium of plasma is governed by [10]

$$\nabla p = \mathbf{j} \times \mathbf{B}, \tag{2.1}$$

where $p = nT$ is the plasma pressure.

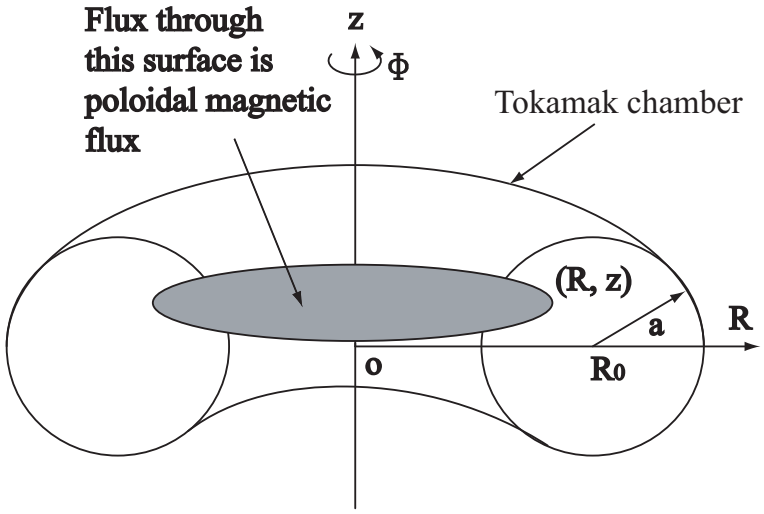

Figure 2.1: Cylindrical coordinate (R, ϕ, z) system showing the definition of poloidal magnetic flux.

In studying tokamak equilibrium, it is convenient to introduce the poloidal magnetic flux function $\Psi(R, z)$. $\Psi = 2\pi R A_\phi$ in axisymmetric system such as tokamaks,

where A_ϕ is the magnetic vector potential. Ψ = constant surface defines magnetic surface, since

$$\mathbf{B} \cdot \nabla \Psi = 0. \tag{2.2}$$

In an axisymmetric torus as shown in Figure (2.1), the equilibrium Eq. (2.1) can be rewritten in terms of Ψ as [10]:

$$R\frac{\partial}{\partial R}\left(\frac{1}{R}\frac{\partial \Psi}{R}\right) + \frac{\partial^2 \Psi}{\partial z^2} = -\mu_0 R^2 p'(\Psi) - \mu_0^2 f(\Psi) f'(\Psi), \tag{2.3}$$

where f and p are arbitrary functions of Ψ and primes indicate derivatives with respect to Ψ. The equation is called the Grad-Shafranov equation. In general, the Grad-Shafranov equation is nonlinear and the plasma equilibrium may not be uniquely determined. Often bifurcation in equilibrium occurs.

In tokamaks, the toroidal magnetic field provides the main confinement of the plasma. The required rotational transform is provided by the poloidal magnetic field created by the toroidal current. The combination of the toroidal and poloidal fields results in a helical magnetic field with closed, nested magnetic surfaces. The helical magnetic field is characterized by the toroidal and poloidal magnetic field B_ϕ and B_θ as shown in Figure 2.2.

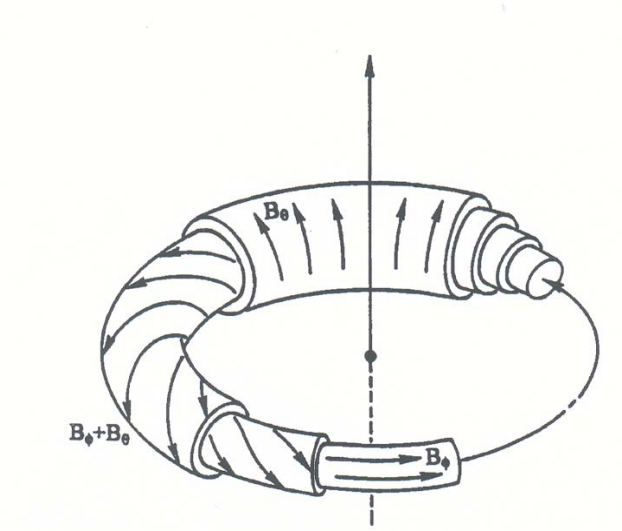

Figure 2.2: Toroidal magnetic field B_ϕ and poloidal magnetic field B_θ resulting in a helical magnetic field, from Chen [11].

The pitch of the field lines is defined as the safety factor q,

$$\frac{1}{q(r)} = \frac{d\theta}{d\phi} = \frac{RB_\theta}{rB_\phi}, \tag{2.4}$$

where θ is the poloidal angle, ϕ is the toroidal angle, r is the minor radius, and R is the major radius. The quantity $q(r)$ is so called because of its importance in determining plasma stability against the kink instability.

In addition to the toroidal and poloidal magnetic fields, a small vertical magnetic field must be applied to a tokamak discharge to counterbalance the radially expanding force due to plasma pressure, plasma inductance and mutual inductance between the plasma current and the toroidal coils. This field can be determined by identifying the total expansion force.

The magnetic force is given by

$$F_1 = \frac{\partial}{\partial R}\left(\frac{1}{2}LI_p^2\right) = \frac{1}{2}I_p^2\mu_0\left[\ln\left(\frac{8R}{a}\right) - 1 + \frac{l_i}{2}\right], \tag{2.5}$$

where L is the inductance of toroidal plasma and given by

$$L = \mu_0 R\left[\ln\left(\frac{8R}{a}\right) - 2 + \frac{l_i}{2}\right], \tag{2.6}$$

in which l_i is the internal inductance parameter (l_i =1/2 for a uniform toroidal current density and $l_i = 0$ for skin current).

A plasma confined in a toroidal chamber also tends to expand radially with the so-called ballooning force,

$$F_2 = \frac{\partial}{\partial R}(2\pi^2 R a^2 \bar{p}) = 2\pi^2 a^2 \bar{p}, \tag{2.7}$$

where $\bar{p}$ is the average plasma pressure.

Finally, the force due to the change in the toroidal magnetic field is

$$F_3 = -2\pi^2 a^2 \frac{1}{2\mu_0}\left[\overline{B_\phi^2} - B_\phi^2(a)\right], \tag{2.8}$$

where $\overline{B_\phi^2}$ is the average over the plasma cross-section,

$$\overline{B_\phi^2} = \frac{1}{\pi a^2}\int_0^a B_\phi^2(r) 2\pi r dr. \tag{2.9}$$

The radial component of the equilibrium

$$\nabla\left(p+\frac{B^2}{2\mu_0}\right)=\frac{1}{\mu_0}(\mathbf{B}\cdot\nabla)\mathbf{B} \tag{2.10}$$

yields

$$\bar{p}+\frac{1}{2\mu_0}\left[\overline{B_\phi^2}-B_\phi^2(a)\right]=\frac{1}{2\mu_0}B_\theta^2(a), \tag{2.11}$$

or

$$\frac{1}{2\mu_0}\left[\overline{B_\phi^2}-B_\phi^2(a)\right]=\frac{B_\theta^2(a)}{2\mu_0}(1-\beta_p), \tag{2.12}$$

where

$$\bar{p}=\frac{2}{a^2}\int_0^a p(r)rdr, \tag{2.13}$$

and

$$\beta_p=\frac{\bar{p}}{B_\theta^2(a)/2\mu_0} \tag{2.14}$$

is the poloidal β.

The total radial expansion force, $F_1+F_2+F_3$, can be counterbalanced by applying a vertical magnetic field $B_\perp$ which exerts a radially inward Lorentz force, $2\pi RB_\perp I_p$. The required vertical magnetic field is given by

$$B_\perp=\frac{\mu_0 I_p}{4\pi R}\left[\ln\left(\frac{8R}{a}\right)+\beta_p+\frac{l_i}{2}-\frac{3}{2}\right]. \tag{2.15}$$

As the plasma pressure and current density distribution vary, the vertical field should accordingly be adjusted to maintain the plasma discharge at a desired position. In most tokamaks (including STOR-M), active feedback control is used to achieve such adjustment.

2.2 Plasma confinement

To achieve thermonuclear conditions in a tokamak it is necessary to confine the plasma energy for a sufficient time. The global energy confinement time, denoted by τ_E is [10]

$$\tau_E=\frac{\frac{3}{2}n(T_i+T_e)}{P}, \tag{2.16}$$

where P is the total heating power. Confinement is limited by thermal conduction and convection processes and by radiation. The efficiency of confinement of plasma pressure by the magnetic field is represented by the ratio

$$\beta = \frac{p}{B^2/2\mu_0}. \tag{2.17}$$

β is limited to values of around a few per cent (i.e. the plasma pressure must be much lower than the magnetic pressure) due to plasma instabilities, such as the ballooning mode.

In a collisionless plasma with straight magnetic field lines, particles move along helical orbits composed of a circular motion with a Larmor radius $r_L = mv_\perp/eB$ in the direction perpendicular to the magnetic field and a free motion in the direction of the magnetic field. In such a plasma, there is no perpendicular displacement of the particles from one field line to another and, therefore, there is no perpendicular transport. Collisions lead to the deviation of the trajectory of the particles and, in the direction perpendicular to the magnetic field, particles are displaced by a distance of the order of the Larmor radius r_L. This gives the following expression for the diffusion coefficient across the magnetic field

$$D_c = \nu r_L^2, \tag{2.18}$$

where ν is the collision frequency. In the case of a fully ionized plasma, ν will be the electron-ion frequency. This transport induced by collisions in a cylindrical plasma is called classical transport.

In toroidal geometry, there is inevitable curvature and gradient in the magnetic field. The reduced symmetry leads to an enhanced level of transport known as neoclassical transport. This takes different forms depending on the collisionality of the plasma. In a highly collisional plasma the transport is Pfirsch-Schlüter transport, whereas with low collisionality, tapped particles cause the so-called banana diffusion.

The diffusivity in a toroidal geometry is enhanced by a factor $1 + q^2$,

$$D_{ps} \simeq \nu r_L^2 (1 + 2\frac{\sigma_\perp}{\sigma_\parallel} q^2) = \nu r_L^2 (1 + q^2), \tag{2.19}$$

where q is the safety factor introduced earlier and $\sigma_{\parallel} = 2\sigma_{\perp}$. The factor $(1+q^2)$ is due to toroidicity. The Pfirsch-Schlüter formula in Eq. (2.18) is valid in the collisional regime characterized by

$$\nu > \frac{\upsilon_T}{qR}, \tag{2.20}$$

where υ_T is the electron thermal velocity. As the collision frequency decreases with an increase in the plasma temperature, the diffusivity tends to decrease. However, in the collisionless regime (banana regime), the diffusivity is enhanced by trapped particles and is given by

$$D \simeq \frac{D_{ps}}{\epsilon^{3/2}} \quad \left(\nu < \epsilon^{3/2}\frac{\upsilon_T}{qR}\right), \tag{2.21}$$

where $\epsilon = r/R$ (the inverse aspect ratio).

In the intermediate collisionality regime, $\epsilon^{3/2}\upsilon_T/qR < \nu < \upsilon_T/qR$, the diffusivity becomes insensitive to the collision frequency,

$$D_{ps} \simeq r_L^2 q^2 \frac{\upsilon_T}{qR}. \tag{2.22}$$

This is called the plateau regime. Figure (2.3) shows the neoclassical prediction of the variation of diffusion coefficient D with collision frequency.

In a large tokamak such as JET ($a/R = 1.3$ m/3 m), the plasma has a high temperature and density ($\bar{T}_e \simeq 5$ keV, $\bar{n}_e \simeq 3 \times 10^{19}\,\mathrm{m}^{-3}$) and the electron-ion collision frequency is estimated to be 3.88×10^3 s^{-1}, which is two orders of magnitude smaller than $\epsilon^{3/2}\upsilon_T/qR$ ($\simeq 8.7 \times 10^5\,\mathrm{s}^{-1}$). The discharge is, therefore, in the collisionless regime.

For a smaller tokamak such as STOR-M, T_e is about 200 eV and n_e is $2 \times 10^{19}\,\mathrm{m}^{-3}$ at the plasma center. The estimated electron-ion collision frequency is around 2.2×10^5 s^{-1}, which is three times smaller than $\epsilon^{3/2}\upsilon_T/qR$ ($\simeq 6.9 \times 10^5\,\mathrm{s}^{-1}$), and the plasma is marginally in the collisionless regime. However, the plasma temperature is low in the edge region ($T_e \simeq 30$ eV, $n_e \simeq 3 \times 10^{18}$ m^{-3}), the collision frequency is about $1 \times 10^6\,\mathrm{s}^{-1}$ while $\upsilon_T/qR = 2.0 \times 10^6\,\mathrm{s}^{-1}$ and $\epsilon^{3/2}\upsilon_T/qR \simeq 2.6 \times 10^5\,\mathrm{s}^{-1}$. The edge plasma in STOR-M is in the plateau regime, or near the collisional regime.

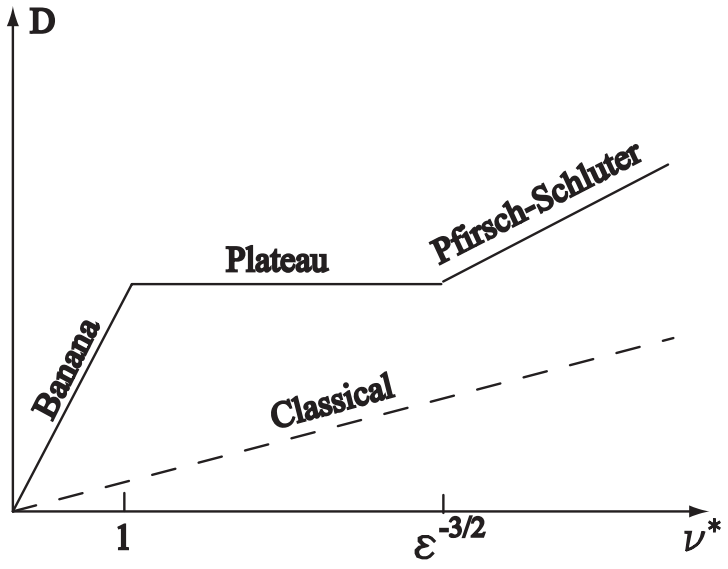

Figure 2.3: Neoclassical prediction of variation of D with collision frequency. Dashed line corresponds to the behavior of the classical diffusion coefficient. $\nu^* = \frac{\nu_{ei}}{\epsilon^{-3/2}\frac{v_T}{qR}}$ is the collisionality parameter.

In practice, the neoclassical diffusion coefficients (particle and thermal) are seldom obtained in tokamaks. The confinement times in tokamaks are anomalously short due to plasma turbulence. This will be explained in Section 2.3.2.

2.3 Stability of tokamak discharges

A magnetically confined plasma is not in thermal equilibrium with its environment and thus is expected to be intrinsically unstable against various electrostatic and electromagnetic modes. It is generally accepted that the experimentally observed level of transport in tokamaks is due to instabilities and fluctuations of electric potential and magnetic field inherent to the plasma. In accordance to a scale of instabilities, they may be roughly categorized into two classes: macroscopic and microscopic. The first class involves the physical displacement of plasma on the scale much larger than Larmor radius and may be, therefore, described by MHD equations. Thus, this category of instabilities is also called MHD instabilities, including kink instabilities, tearing modes, and ideal/resistive ballooning modes [10]. Microinstabilities are caused by

small fluctuations of the electric or magnetic field which lead to small fluctuations in the particle velocity and radial position, enhancing the characteristic length of radial particle displacement and leading to anomalous particle and energy transport.

2.3.1 MHD instabilities

MHD instabilities are long wavelength electromagnetic modes [58]. Because of the long wavelength nature, the entire plasma is perturbed and, in this respect, MHD instabilities are most dangerous and may cause discharge disruption [59].

MHD modes may be classified into current driven and pressure gradient driven types. A typical current driven MHD instability is the kink mode [123]. In the lowest order, the dispersion relation of the kink mode is given by [60]

$$\omega^2 = \frac{V_A^2}{(qR)^2}(m - nq)(m - nq - 1), \tag{2.23}$$

where $V_A = B/\sqrt{\mu_0 \rho}$ is the Alfvén velocity and ρ is the mass density of the tokamak plasma. the perturbation of the form

$$\sum_{m,n} f(r) e^{i(m\theta - n\phi) - i\omega t}, \tag{2.24}$$

is assumed in cylindrical geometry (r, θ, ϕ), and $m\,(n)$ is the poloidal (toroidal) mode number. For the longest wavelength mode with $m = n = 1$, the stability condition $(\omega^2 > 0)$ becomes $q > 1$. In general, the $m = m, n = 1$ mode can be stabilized if $q > m$.

In tokamaks, q is nonuniform, starting at q slightly less than unity at the magnetic axis (at the core) and increasing toward the periphery. The surface safety factor $q(a)$ is usually chosen larger than 3. Wherever q becomes a rational number such that $q(r) = m/n$, resonant perturbation can take place in the vicinity of the rational magnetic surfaces. MHD perturbations near the $q = 1$ surface are readily observable in tokamaks as sawtooth oscillations in soft x-ray signals [61]. This instability is characterized by relaxations with a fast collapse or crash of the center plasma pressure followed by a gradual build-up phase. The presence of sawteeth is an important energy loss channel from the central region. Higher order modes $(m \geq 2)$ can also

be detected by Mirnov coils located outside the discharge chamber. In practice, the maximum plasma current allowed in a tokamak is limited by the condition $q(a) > 2$, where a is the minor radius. This is known as the $q = 2$ MHD barrier and, unless the plasma current is ramped sufficiently, it is difficult to cross the barrier without causing a major plasma disruption [62]. Therefore, in tokamaks, the maximum plasma current is imposed by the condition $q(a) \geq 2$, or

$$I_p \leq \frac{1}{\mu_0}\frac{\pi r^2}{R}B_\phi, \tag{2.25}$$

which in turn limits the ohmic heating power.

The ballooning mode is a pressure gradient MHD mode [63] and is expected to occur when the plasma pressure gradient exceeds a certain limit. The dispersion relation of the ballooning mode is given by [64]

$$\omega^2 \simeq k_\parallel^2 V_A^2 - 4\frac{c_s^2}{RL_p}, \tag{2.26}$$

where $k_\parallel \simeq 1/qR$ is the wavenumber along the magnetic field, $c_s = \sqrt{p/\rho}$ is the sound speed, and L_p is the pressure gradient scale length. The driving source of the ballooning mode is the unfavorable magnetic curvature combined with pressure gradient.

2.3.2 Microinstabilities

Microinstabilities are characterized by wavelengths of the order of a few ion Larmor radii. Approximating an average plasma particle displacement caused by microinstabilities with typical perpendicular wavelength of unstable spectrum $1/k_\perp$ and characteristic time with linear growth period $1/\gamma$, one can obtain an estimate of the diffusion coefficient:

$$D \simeq \frac{\gamma}{k_\perp^2}. \tag{2.27}$$

Depending on the growth rate γ, the resulting diffusion coefficient can be significantly larger than the neoclassical value. In addition, depending on the type of the instability, an inward or outward convection can appear.

A particularly important class of microinstabilities is the drift instabilities, which are associated with a diamagnetic current induced by the plasma itself through diamagnetism:

$$\mathbf{J} = \frac{\mathbf{B} \times \nabla p}{B^2}. \tag{2.28}$$

Various drift type instabilities are driven by a density and/or temperature gradient and the thermal expansion force is the source of those instabilities. The classical example is the drift mode (the universal mode [65]) driven by the electron Landau damping and trapped electron magnetic drift resonance.

One of the most important drift instabilities is the ion temperature gradient (ITG) mode [66-68]. The ITG mode is a drift wave driven by an ion pressure gradient in the unfavorable magnetic curvature region. The temperature gradient parameter

$$\eta_i \equiv \frac{d(\ln T_i)}{d(\ln n_i)} \tag{2.29}$$

has to exceed a threshold for the ITG mode to be excited. The ITG mode can be suppressed by plasma nonuniform plasma rotation and the ion thermal diffusivity of the order of the neoclassical value has been achieved in several tokamaks. However, the electron thermal diffusivity χ_e continues to be anomalous which indicates that the anomalous χ_e is caused by other instabilities. Candidate instabilities include the electron temperature gradient (ETG) mode [124], skinsize electromagnetic drift mode, and trapped electron mode (TEM).

2.4 Plasma heating

Fusion reactions require fuels to be heated to a high temperature. The initial plasma heating in all tokamaks comes from the Ohmic heating caused by the toroidal current. The Ohmic heating density is

$$P_\Omega = \eta J^2 = 0.071 \frac{(B_\phi/R)^2}{T_e^{3/2}} \ (\mathrm{MW} \cdot \mathrm{m}^{-3}), \tag{2.30}$$

where η is the resistivity of the plasma, J is the current density, T_e is the central electron temperature in keV, and the axial value of the safety factor, $q_0 = 2B_\phi/\mu_0 j_0 R$,

is approximately unity. It is clear that Ohmic heating becomes ineffective as the plasma temperature increases. The maximum electron temperature achievable by Ohmic heating alone is a few keV. Any attempt to make use of Ohmic heating at high temperatures requires high magnetic field. In most tokamaks, Ohmic heating is used for the initial plasma production, the current ramp up, and the quasi-steady current phase.

The two main methods which are envisaged for heating to ignition temperatures are injection of energetic neutral beams (NBI) and the resonant absorption of radio frequency (RF) electromagnetic waves at resonant plasma frequencies such as ion-cyclotron (ICRF), electron cyclotron (ECRF) and lower hybrid (LHRF). These auxiliary plasma heating techniques have successfully contributed to the heating of the plasma to the temperature required for fusion, but they have also shown significant degradation in the energy confinement time with the injected power, and the plasma temperature increment is not linearly proportional to the heating power. For example, the energy confinement time with the ITER H-mode scaling law [12] has a heating power dependence,

$$\tau_E \propto \frac{1}{P^{0.69}}, \tag{2.31}$$

where P is the auxiliary heating power. This is because of the fact that confinement is determined mainly by turbulent processes in plasmas, which are significantly influenced by the heating processes themselves. The confinement time has been experimentally found to increase with the size of the machine and with the plasma current, hence the desirability of large machines. For example, the empirical scaling law for ITER H-mode discharge is given by [12]

$$\tau_E(s) = 0.0562 A_i^{0.19} A^{-0.58} I_p^{0.93} k_a^{0.78} n^{0.41} B^{0.15} P^{-0.69} R^{1.97}, \tag{2.32}$$

where A_i is the average isotopic mass number ($A_i = 1$ for hydrogen plasma), A the aspect ratio R/a, I_p the plasma current in MA, k_a is the elongation factor at the plasma surface, n the plasma density in $10^{19}\,\mathrm{m}^{-3}$, B the toroidal magnetic field in T, P the total heating power in MW, and R the major radius in meters.

The toroidal current in tokamaks can be driven by various means. Induction

current drive based on transformer action is by far the most efficient and economical. However, inductive current drive cannot last forever because of the limit in the magnetic flux in the transformer. Injection of microwaves at the lower hybrid resonance frequency has successfully been developed and is currently considered as one of the candidates for steady state current drive. It is noted that in high performance tokamak discharges, a large fraction of toroidal current is driven by the plasma itself in the form of the bootstrap current [2, 3]. The bootstrap current is caused by incomplete cancellation between neighboring trapped particle fluxes in the toroidal direction and approximately given by

$$J_{BS} \simeq -\frac{\sqrt{\epsilon}}{B_\theta}\frac{dp}{dr}, \tag{2.33}$$

where $\sqrt{\epsilon} = \sqrt{r/R}$ is the fraction of trapped particles and B_θ is the poloidal magnetic field. Since the bootstrap current is proportional to the pressure gradient, scenarios with large internal pressure gradients are being developed. Such scenarios are called advanced tokamak scenarios [69], with a large fraction of the plasma current being provided by the bootstrap current. This kind of operation has been achieved on the TCV tokamak where no inductive current is driven and about 80% of I_p is bootstrap current [70].

Chapter 3

The physics of CT fuelling

Physical processes involved in CT formation, acceleration, and CT-tokamak interaction are complicated as found in numerous theoretical, experimental and computational investigations [4-8, 25-26, 31-42, 47, 51-52, 54-57]. CT formation involves self-organization of magnetically confined plasma through nonlinear magnetohydrodynamics [25]. Main processes in CT-tokamak interaction include CT deceleration by the magnetic field, "tilt" instability, magnetic reconnection, and excitation of plasma waves (Alfvén waves). In this Chapter, basic plasma physics involved in CT formation and its interaction with a tokamak will be described.

3.1 The magnetic field structure of CT plasma

CTs are self-contained, magnetized plasma structures [25] that have internal toroidal and poloidal magnetic fields associated with internal poloidal and toroidal plasma currents. After formation, a CT relaxes to a force-free state (Taylor state) [71], which is characterized by a plasma current parallel to the magnetic field, $\mathbf{J} \parallel \mathbf{B}$. In this case, Ampere's law reduces to

$$\nabla \times \mathbf{B} = \lambda \mathbf{B}, \tag{3.1}$$

where λ is a constant having dimensions of inverse length. Constant λ corresponds to the minimum energy (or force-free) state for CT.

It is convenient to describe CT magnetic fields in an axisymmetrical (r, ϕ, z) coordinate system, as shown in Figure 3.1. A poloidal flux function is defined as $\Psi = \int \mathbf{B} \cdot d\mathbf{A} = 2\pi r A_\phi$, where A_ϕ is the magnetic vector potential associated with the toroidal current in the CT. The magnetic axis of CT is the radial location where

the poloidal magnetic flux Ψ reaches its maximum, or $B_z = 0$ [72].

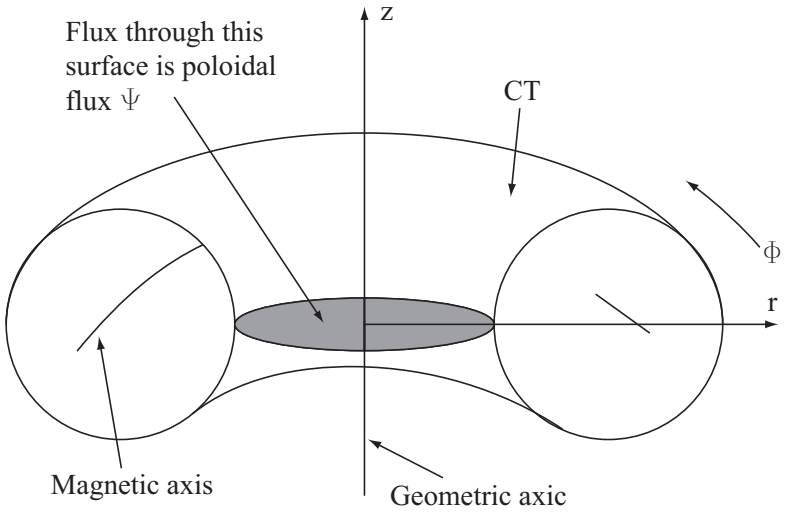

Figure 3.1: Cylindrical (r, ϕ, z) coordinate system showing poloidal flux Ψ and the CT magnetic axis.

For an axially symmetric two-dimensional CT surrounded by a flux conserving cylinder of inner radius R_{fc} and height L_{fc} (see Figure 3.2(b)), Eq. (3.1) can be solved with the boundary conditions such that $B_r = B_\phi = 0$ at $r = R_{fc}$. The poloidal components (B_z, B_r), toroidal component (B_ϕ), and the poloidal magnetic flux (Ψ) are [73-75]:

$$B_z = B_0 J_0(k_r r)\sin(k_z z), \tag{3.2}$$

$$B_r = -B_0 \frac{k_z}{k_r} J_1(k_r r)\cos(k_z z), \tag{3.3}$$

$$B_\phi = B_0 \frac{\lambda}{k_r} J_1(k_r r)\sin(k_z z), \tag{3.4}$$

$$\Psi = B_0 \frac{r}{k_r} J_1(k_r r)\sin(k_z z), \tag{3.5}$$

where J_0 and J_1 are the Bessel functions of the first kind, $k_z = \dfrac{\pi}{L_{fc}}$ is the axial wavenumber, $k_r = \dfrac{3.83}{R_{fc}}$ (3.83 being the first root of the Bessel function J_1), and $\lambda = \sqrt{k_r^2 + k_z^2}$. Substituting $k_r = 3.83/R_{fc}$ into Eq. (3.2) and letting $B_z = 0$, the location of the CT magnetic axis is found to be at $r = 0.63 R_{fc}$.

Normally, CTs are formed and accelerated in a coaxial electrode configuration. In this case, the boundary conditions are given by $B_r = 0$ at $r = r_{in}, r_{out}$, where r_{in}

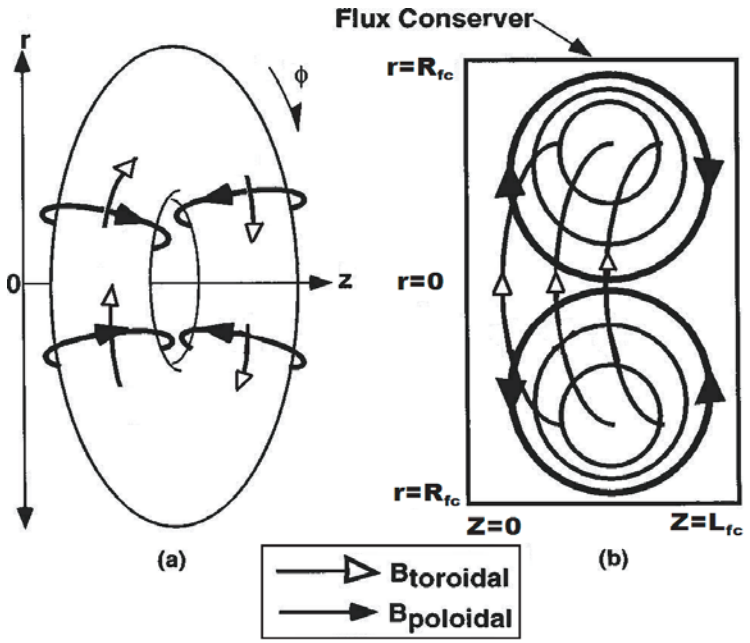

Figure 3.2: Two views of CT magnetic fields. In (b), the cross section is taken in the poloidal $(r-z)$ plane. The flux cylindrical conserver is shown in the cross section view only, from Geddes [73].

and r_{out} are the radii of the inner and outer electrode, respectively. Corresponding analytical solution of Eq. (3.1) is:

$$B_z = B_0[J_0(k_r r) + F_0 Y_0(k_r r)]\sin(k_z z), \tag{3.6}$$

$$B_r = -B_0\frac{k_z}{k_r}[J_1(k_r r) + F_0 Y_1(k_r r)]\cos(k_z z), \tag{3.7}$$

$$B_\phi = B_0\frac{\lambda}{k_r}[J_1(k_r r) + F_0 Y_1(k_r r)]\sin(k_z z), \tag{3.8}$$

where Y_i is the Bessel functions of the second kind. k_r and F_0 are determined from

$$J_1(k_r r_{in}) + F_0 Y_1(k_r r_{in}) = 0, \tag{3.9}$$

$$J_1(k_r r_{out}) + F_0 Y_1(k_r r_{out}) = 0. \tag{3.10}$$

Figure 3.3 shows the field profile of the CT in the USCTI acceleration region. In this case, $k_z = 0.21$ cm^{-1} (measurement shows CT length is about 15 cm in USCTI [38]), $k_r = 1.01$ cm^{-1}, and $F_0 = 2.58$.

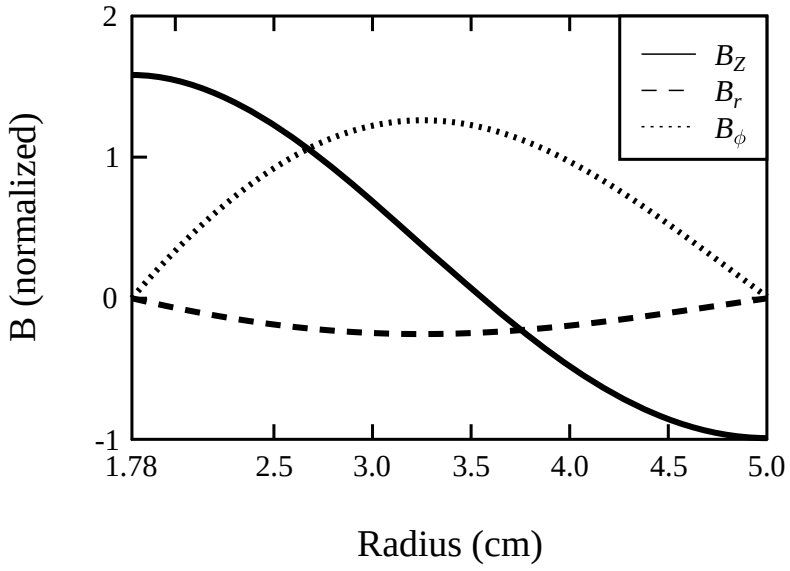

Figure 3.3: Radial profile of CT magnetic fields in the USCTI acceleration region, r_{in} =1.78 cm, r_{out} = 5 cm.

3.2 CT formation and acceleration

An illustration of the CT formation process is shown in Figure 3.4. In the first stage, a solenoid prepares a bias magnetic field (stuffing magnetic field), as shown in Figure 3.4-(1). In Figure 3.4-(2), working gas (e.g., hydrogen) is puffed into the coaxial cylindrical electrode. Then, the formation capacitor bank is discharged across the electrodes, breaking down the gas and forming a plasma. A current flows from the center conductor radially outward inducing a magnetic field in the azimuthal direction. The resulting $\mathbf{J} \times \mathbf{B}$ force then pushes the plasma down the electrodes until the solenoid field pinches off behind it, forming the CT poloidal magnetic field, as shown in Figure 3.4-(3),(4). The magnetic field generated by the formation bank discharge current becomes the CT toroidal field. In USCTI, the typical CT field strength is about 0.2 T and CT plasma temperature is about 10 eV.

Within a few microseconds after formation, the CT relaxes to the minimum energy state. As the CT detaches itself from the formation region, it is accelerated along the electrodes by discharge of the CT acceleration capacitor bank. The $\mathbf{J} \times \mathbf{B}$ force provides the accelerating force and the CT acts as a sliding short, as shown

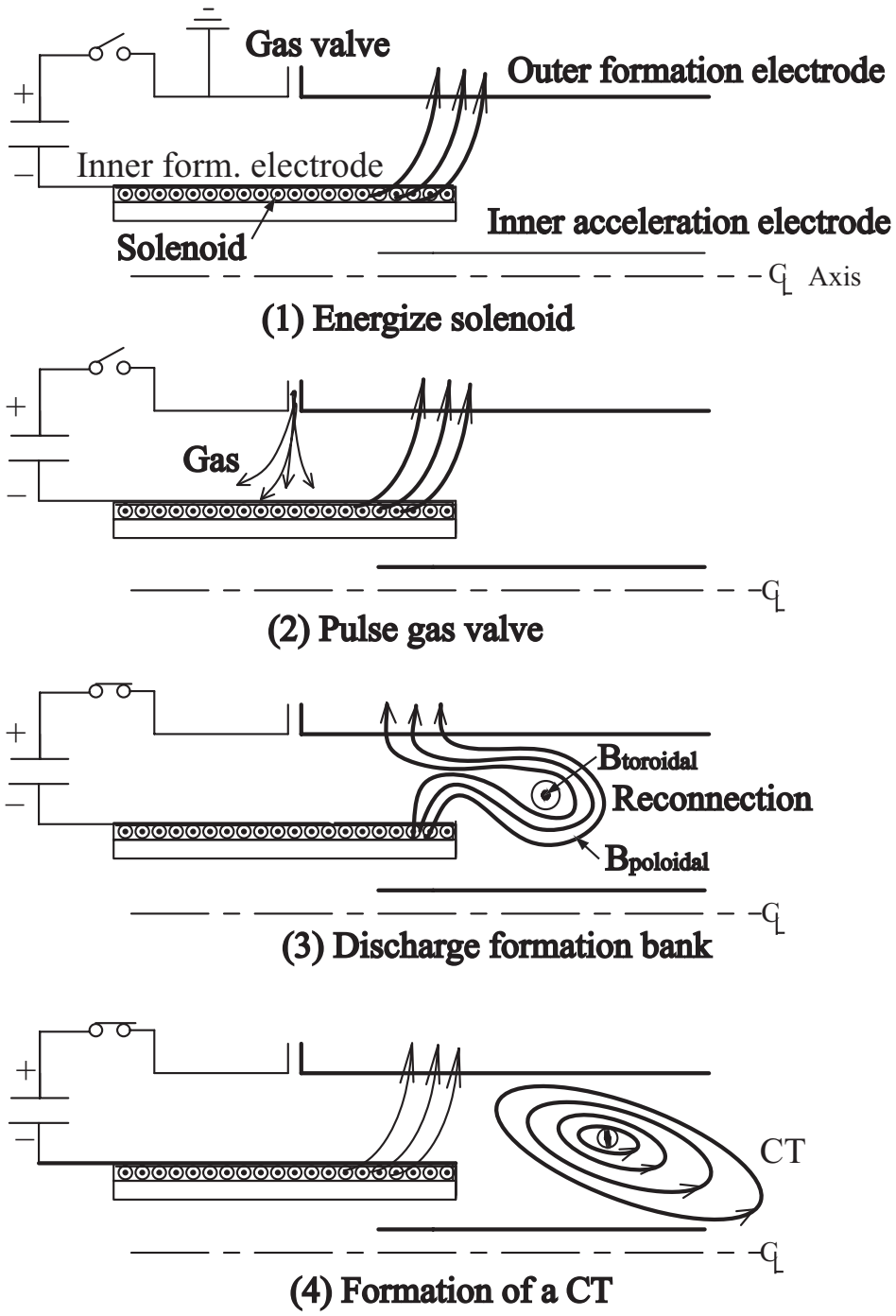

Figure 3.4: Process of CT formation

in Figure 3.5. During passage of the CT along the coaxial electrode, its radial expansion is prevented by a radial equilibrium force generated by an image current in the conducting walls. The CT so formed is robust and can maintain its rigidity during acceleration. CT velocity up to 2000 kms^{-1} was achieved in early experiments [32].

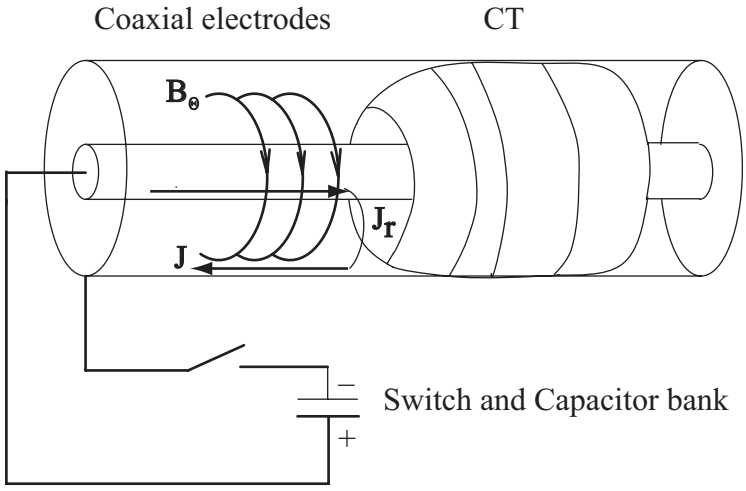

Figure 3.5: CT acceleration. The magnetic field **B** is in the azimuthal direction and the current **J** is in the radial direction. $\mathbf{J} \times \mathbf{B}$ pushes the CT axially to the right (Baker *et al*. [47]).

A CT with higher mass density can be obtained by compression [31-33, 43-44, 77]. The CT compression can be achieved by letting a CT pass through conical coaxial electrodes, as shown in Figure 3.6. As viewed by the CT, the conical electrodes appear as a compressing liner. Compression ratio is defined as R_{c1}/R_{c2}. Scaling law and numerical simulation [31] indicate that the CT compression should be self-similar, i.e., radial focusing is accompanied by axial contraction. The compression ratio must be chosen carefully to avoid CT reflection. In addition, the compression time must be sufficiently long to allow the CT to undergo self-similar compression and to avoid exciting shock waves that impede the compression. The CT compression time $\tau_{comp} \gg \tau_{A,CT}$ is crucial in this process, where $\tau_{A,CT} = r/V_{A,CT}$ and $V_{A,CT}$ is the Alfvén velocity of the CT. Of course, $\tau_{comp} \ll \tau_{CT}$ must be met; that is, the CT lifetime must be longer than the compression time. The process is adiabatic and, therefore, it can lead to an increase in CT density, temperature and magnetic field.

In RACE [32], the magnetic field amplification was observed by factors of four, e.g., 0.1 T of CT magnetic field at the entrance of the cone increased to 0.4 T at the exit and the compression ratio was between 2 and 3.

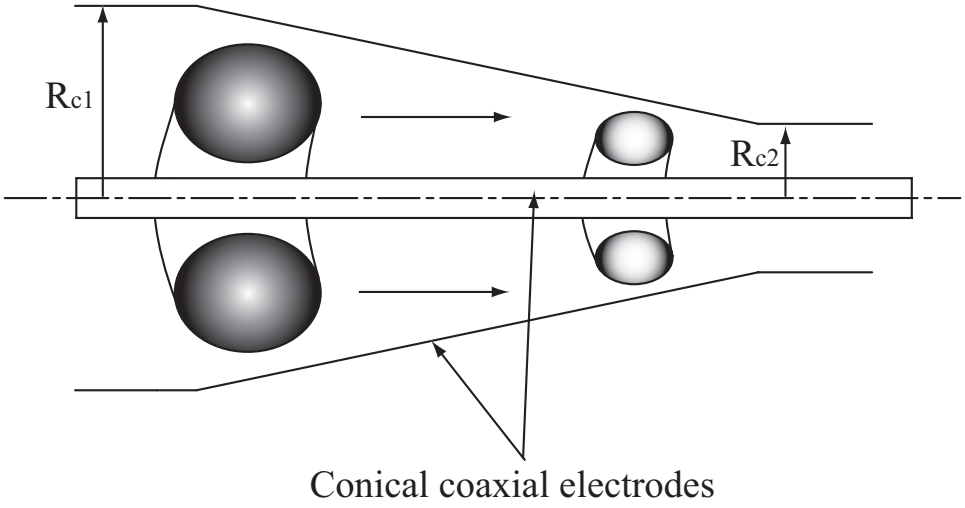

Figure 3.6: CT compression in conical coaxial electrodes. R_{c1} is the radius at the entrance and R_{c2} is the radius at the exit.

It has been found that the eigenvalue λ in Eq. (3.1) can be determined by gun discharge current I_{gun} (formation discharge current) and the bias flux Ψ_{bias} [78]:

$$\lambda = \frac{\mu_0 I_{gun}}{\Psi_{bias}}. \tag{3.11}$$

To form an isolated CT detached from the formation region, a threshold of λ, denoted by λ_c, must be exceeded in the discharge. It has been predicted [75] that for a cylindrically symmetric gun $\lambda_c = 3.83/\delta_{gap}$, where δ_{gap} is the radial distance between the inner and outer electrodes. If $\lambda < \lambda_c$ the CT would not detach from the formation region.

λ is an important parameter to determine CT equilibrium. In the simplest case, constant λ corresponds to the force-free state of CT. Variable λ can be used to model CTs which depart from the force-free state. When considering variable λ states, it is convenient to express λ as a power series in Ψ, and usually the first order term is relevant. This yields [73]:

$$\lambda = \bar{\lambda}\left[1 + \alpha(2\frac{\Psi}{\Psi_{max}} - 1)\right], \tag{3.12}$$

where α governs the dependence on Ψ and Ψ_{max} is the maximum of poloidal flux (at the CT magnetic axis). $\bar{\lambda}$ is the average value of λ over the plasma. If $\alpha > 0$, the current profile is peaked which is typical of a CT in decay, since the edges are cooler and more resistive than the core. If $\alpha < 0$, the current profile is hollow which is typical of a CT still being driven in the gun. While $\alpha = 0$, CT is in the fully force free state corresponding to constant λ. The process can proceed to arbitrary order in Ψ as needed. Higher order in Ψ allows description of more sharply peaked current distributions. For example, the λ profile described in second order in Ψ can be in the form of:

$$\lambda = \bar{\lambda}\left[1 + \alpha(2\frac{\Psi}{\Psi_{max}} - 1) + \gamma\left[2(\frac{\Psi}{\Psi_{max}})^2 - 1\right]\right], \tag{3.13}$$

where γ is a constant.

Normally the β (the ratio of plasma pressure to magnetic pressure) value for the gun produced CT is less then 10%. Therefore, it is reasonable to neglect the plasma pressure effect in CT equilibrium and the CT is in the force-free state. This can be seen from $\mathbf{J} \times \mathbf{B} = \nabla P \simeq 0$, which implies $\mathbf{J} \parallel \mathbf{B}$. When it is necessary to consider the effects of plasma pressure on the equilibrium (generally when $\beta > 10\%$), the Grad-Shafranov equation [10] has to be solved, as for equilibrium in tokamaks. For example, when the CT is compressed adiabatically in the conical electrodes, it is accompanied by plasma heating.

CT acceleration can be described by a one-dimensional point model originally developed by Hammer *et al.* [31-33]. In this model, the CT is considered as a sliding short between the inner and outer electrodes assuming perfect conductivity of the CT. Figure 3.7 (a) shows the point model for CT acceleration. Although Hammer's model assumes no resistance in the acceleration circuit, it agrees well with experimental results. Essentially, the CT acceleration circuit can be considered as an LRC circuit without external power supplies. Here L is the total inductance including a constant part and a time dependent part due to CT traveling. R_c is the resistance of the circuit. The source of R_c consists of both circuit components and the CT plasma itself. $C = C_{acc}$, is the capacitance of the acceleration bank. Figure 3.7(b) shows the LRC equivalent circuit.

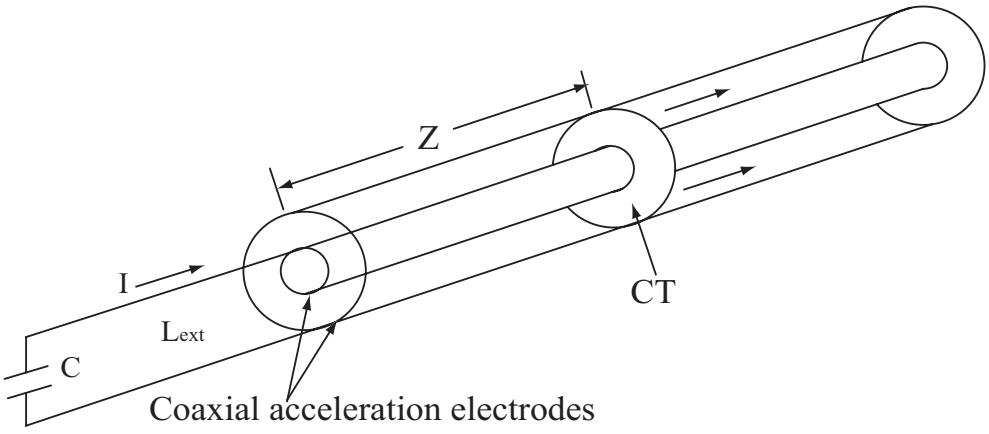

(a)

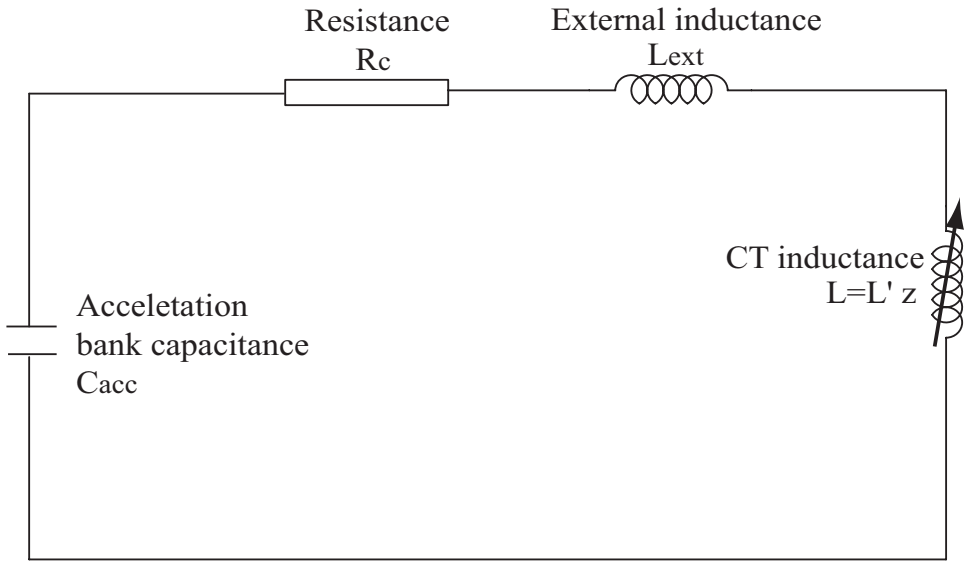

(b)

Figure 3.7: (a) Point model of CT acceleration in a coaxial electrode configuration. The CT acts as a sliding short between the inner and outer electrodes, C is the capacitance of acceleration bank, L_{ext} is the external inductance in the circuit, and I is the discharge current of the acceleration bank. (b) Simplified circuit for CT acceleration in the one dimensional point mode.

The point model [79] with consideration of circuit resistivity R_c consists of three equations below,

$$L_t = L_{ext} + L, \tag{3.14}$$

$$m_{CT}\frac{d^2z}{dt^2} = \frac{1}{2}L^{'}I_{acc}^2 - F_{drag}, \tag{3.15}$$

$$\frac{d^2I_{acc}L_t}{dt^2} + R_c\frac{dI_{acc}}{dt} + \frac{I_{acc}}{C_{acc}} = 0, \tag{3.16}$$

where z is the CT position, $L = \int_0^z L^{'}dx$ ($L^{'} = [\mu_0/2\pi]\ln(r_{out}/r_{in})$ being the inductance of unit length), is the inductance of the coaxial electrode, L_t is the total inductance of the acceleration circuit, L_{ext} is the external inductance of the acceleration circuit, I_{acc} is the discharge current, C_{acc} is the capacitance of the acceleration bank, m_{CT} is the CT mass, and F_{drag} is the drag force. $z(t)$ can be solved by a fourth-order Runge-Kutta method. In the point model, it is assumed that the CT magnetic field B_{CT} is larger than the magnetic field B_{acc}, which is generated by the acceleration current. Otherwise, the CT will be deformed and effective CT acceleration will hardly be realized.

In the CTIX experiments [47], it was found that the CT velocity saturated during its acceleration. The CT velocity will reach the maximum at a critical acceleration voltage. Several mechanisms have been proposed to explain this phenomenon. One of these mechanisms is termed as the "blowby" effect [47, 52] in which the accelerating force becomes too large. "Blowby" can occur when the magnetic pressure pushing the CT, $B_{acc}^2/2\mu_0$, becomes larger than the internal magnetic pressure of the CT, $B_{CT}^2/2\mu_0$. At this point the magnetic field along the inner electrodes, $B_{acc} = \mu_0 I_{acc}/2\pi r$, pushes the CT away from the inner electrode allowing the accelerating flux to leak past and cause CT slow down.

Electrode walls can affect the CT acceleration in several ways. CTs can be slowed down by the accumulation of gas. As a CT travels along the electrode, the gas not ionized or plasma not trapped in the CT magnetic field may be swept up by the CT, introducing a drag effect. CTs can also lose momentum without changing their mass due to charge exchange with gas emitted from the walls. In addition, the accelerating force on CTs can be reduced due to plasma trailing behind them providing a current

return path [80], as shown in Figure 3.8.

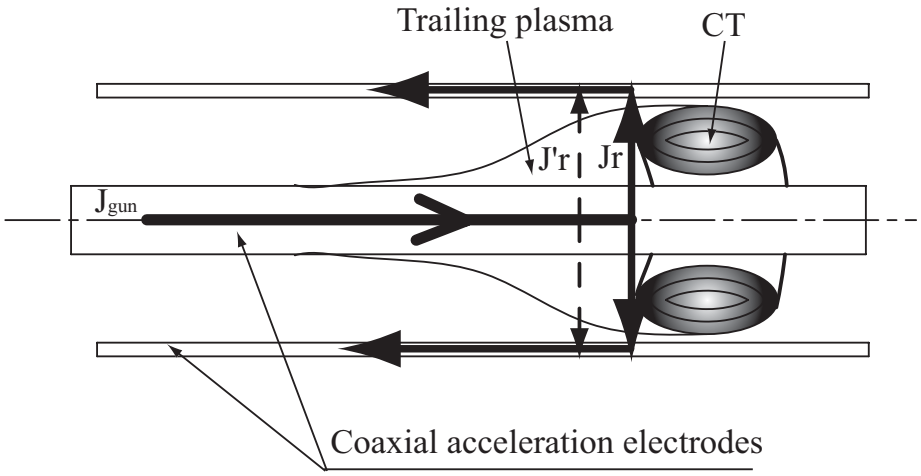

Figure 3.8: Effects of CT the trailing plasma. The gun current $J_{gun} = J'_r + J_r$, in which J'_r is produced by the plasma trailing behind the CT. This current cannot contribute to CT acceleration.

3.3 CT injection into a tokamak

3.3.1 CT penetration into a tokamak toroidal field

In the lowest order approximation, a CT behaves like a magnetic dipole with dipole moment $m \sim \pi I_t r_{CT}^2$, where I_t is the toroidal current inside the CT and r_{CT} is the CT radius [4]. We consider a CT with a dipole moment $\mathbf{m}$ originally oriented perpendicular to the target magnetic field $\mathbf{B}_t$, as in the case of radial CT injection. Once the CT leaves the drift tube of the injector and enters the vacuum tokamak magnetic field region, it will tend to tilt 90° under torque $\mathbf{m} \times \mathbf{B_t}$ until the magnetic moment and $\mathbf{B}_t$ are aligned parallel to each other. This "tilt" time can be expressed as $t_{tilt} \sim (mB_t/I_m)^{-1/2}$, in which $I_m = \frac{2}{5} m_{CT} r_{CT}^2$ is the moment of inertia of the CT. Since $I_t \propto r_{CT} B_{CT}$, we have $t_{tilt} \sim \tau_{A,CT} = r_{CT}/V_{A,CT}$, where $V_{A,CT} = B_t/(4\pi n_{CT} M_i)^{1/2}$ is the Alfvén speed in the CT and M_i is the ion mass.

Here we assume that the characteristic magnetic field inside the CT, B_{CT}, is comparable to B_t in order that the closed magnetic field line topology remains intact. The "tilt" time is so short (typically $< 1\mu$s) that the realignment of the CT with its axis of rotation parallel to the tokamak magnetic field B_t occurs almost immediately after its encounter with B_t. Then, the poloidal magnetic field of the CT reconnects with the tokamak toroidal field and CT configuration rapidly diffuses and deposits the fuel. This process is illustrated in Figure 3.9.

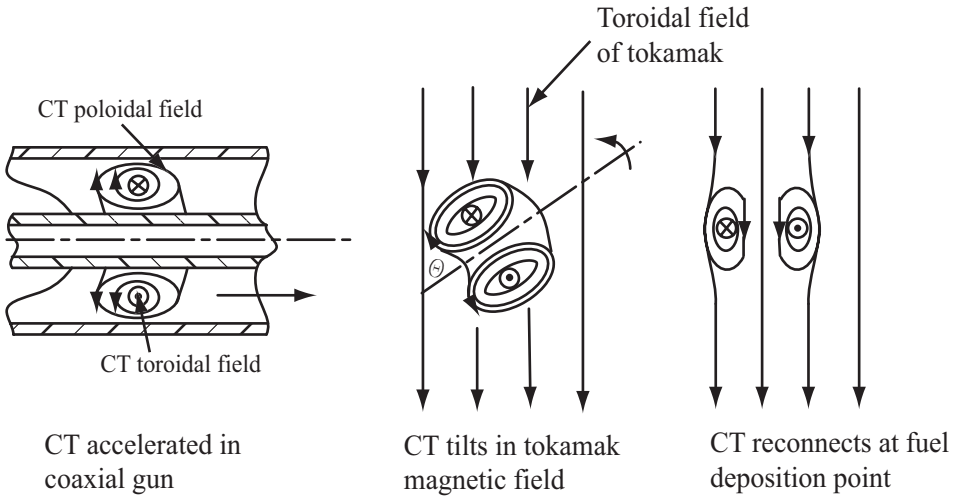

Figure 3.9: Penetration process of CT injection in tokamak plasma. When the CT stops at the desired point in the tokamak plasma, currents that were flowing in the CT get gradually dissipated and the CT loses its identity, from Perkins [5].

An extreme case was studied by Xiao *et al*. [54]. If the CT velocity is relatively low and its penetration time is much longer than t_{tilt}, the dipole axis will oscillate provided reconnection does not occur in time.

In the case of incomplete shielding, the CT tends to tilt so that its magnetic moment aligns with the external magnetic field. The CT 'tilting' phenomenon has been investigated by Turner *et al*. in a flux conserver with a bias magnetic field [78] and by Brown *et al*. in a vacuum tokamak magnetic field [81]. In the experiments by Turner, when a CT was injected into a flux conserver with its magnetic moment anti-aligned with the bias magnetic field, both external field exclusion and 180° CT tilting were observed. In the experiments by Brown *et al*., the CT tilted 90° in the drift

tube, so that the CT magnetic moment was anti-aligned with the tokamak toroidal magnetic field when it entered the tokamak and then another 90° (or −90°) in the tokamak magnetic field with its magnetic moment perpendicular to the tokamak magnetic field.

A CT deposits its fuel in a tokamak through magnetic reconnection [25]. The magnetic reconnection will occur wherever magnetic field becomes tangled or tightly wound. In a region where oppositely directed magnetic field lines are pushed together, the current density $\mathbf{j}_c = \nabla \times \mathbf{B}/\mu_0$ becomes large and anomalous Ohmic dissipation becomes important. Under these conditions, the magnetic structure is destroyed and magnetic field line reconnection starts when the Larmor radius of the ions becomes comparable to the thickness of the current sheet. There are two models to deal with this phenomena.

A simple model for reconnection is the Sweet-Parker model [82-83]. They considered a plane region in which the field in the x direction reversed sign at $y = 0$ and has uniform, but oppositely directed, values for $|y| > L_y$. When the field lines reconnect, the pressure causes them to accelerate away from the reconnection point at $x = 0$, reaching a terminal velocity V_A at a distance $\pm L_x$. In this model, the magnetic reconnection time is evaluated as,

$$\tau_{rec} \sim \frac{L_y}{2V_A}\sqrt{Re_{mag}}, \tag{3.17}$$

where Re_{mag} is the magnetic Reynolds number with V_A the Alfvén velocity,

$$Re_{mag} = \frac{2L_x V_A}{\eta}. \tag{3.18}$$

Alternatively, Petschek [84] proposed a fast reconnection model in which the central diffusion region does not need to have a length $2L_y$. He used X-type neutral points, near which the magnetic field almost vanishes, instead of the current sheet. Petschek modified the Sweet-Parker model by including the effects of wave propagation. There is no wave propagation at the neutral points and diffusion is the main cause of magnetic energy dissipation. With increasing distance from the neutral point, the magnetic field becomes stronger and stronger and finally wave propagation dominates the diffusion.

Based on these two models, we can examine the rapid reconnection limit $\tau_{rec} \cong \tau_A$ (Petscheck) and the slow limit $\tau_{rec} \cong \sqrt{\tau_A \tau_R}$ (Sweet-Parker) in the reconnection between CT and tokamak magnetic fields. Here τ_{rec} is the reconnection time, $\tau_A = r/V_A$ = Alfvén time, $\tau_R = \eta r^2/\mu_0$ = resistive time, r = CT radius, $V_A = B/\sqrt{\mu_0 \rho_{CT}}$, and η = CT resistivity. For rapid reconnection, if the CT penetrates into the tokamak center before reconnection and tilting, then the required kinetic energy density is [5, 85]:

$$\tau_{rec} \cong \tau_A \rightarrow \rho_{CT} V_{CT}^2 \cong \frac{B^2}{\mu_0} (\frac{a}{r})^2. \tag{3.19}$$

For slow reconnection, Alfvén drag is usually the dominant irreversible process. The drag power is given by [26]

$$P_{drag} \cong 2\pi r^2 \rho_{tok} V_{CT}^2 V_{A,tok}, \tag{3.20}$$

where the subscript "tok" is the tokamak parameter. The required energy density is then

$$\rho_{CT} V_{CT}^2 \cong \frac{B^2}{\mu_0} (\frac{a}{r})^2 \frac{\rho_{tok}}{\rho_{CT}}, \tag{3.21}$$

since $\rho_{tok}/\rho_{CT} \ll 1$ for a CT fuelling scheme; the required energy density is much less if the slow reconnection model applies.

Since CT plasma is a good conductor on the penetration time scale (several μs), it will tend to develop screening currents that exclude the tokamak field from the CT. To the extent that the CT behaves as a perfect conductor, the dominating drag would be caused by excitation of Alfvén waves in the tokamak plasma and the CT dynamics would be determined by this drag force together with the ∇B^2 force. If the CT does not behave as a perfect conductor but can undergo magnetic reconnection, the screening currents will dissipate and the CT dipole moment will interact strongly with the tokamak magnetic field and cause tilting. The dynamics of the CT are thus critically dependent on the rate at which magnetic field line reconnection can occur.

3.3.2 CT deceleration mechanisms

A CT with finite directed kinetic energy will slow down with its penetration into a tokamak magnetic field. Two kinds of deceleration mechanisms are proposed to account for CT deceleration.

1. **Alfvén wave drag**.

   A conducting sphere moving in a magnetized plasma experiences an MHD wave drag, as discussed by Newcomb [26],

   $$\mathbf{F}_{drag} = -2\pi\rho r_{CT}^2 K V_A \mathbf{V}_{CT}, \tag{3.22}$$

   where ρ is the mass density in the tokamak plasma, $V_{A,tok}$ the Alfvén velocity in the tokamak plasma and K a coefficient

   $$K = \frac{V_{s,tok}}{V_A}\left[\frac{2}{9}(1+\ln\frac{V_A}{V_{s,tok}}) - 0.37\right], \tag{3.23}$$

   with $V_{s,tok}$ denoting the velocity of sound in the tokamak plasma. The negative sign in Eq. (3.22) indicates a friction force.

2. **Magnetic field gradient force**

   When a CT enters a tokamak, the induced surface current in the CT prevents penetration of the tokamak magnetic field into the CT and a strong field exclusion effect is expected. The work done by the CT to exclude the tokamak magnetic field lines is estimated as

   $$U_{\nabla B} = \frac{B_{tok}^2}{2\mu_0}\frac{4}{3}\pi r_{CT}^3, \tag{3.24}$$

   where $B_{tok}^2/2\mu_0$ is the energy density of the tokamak magnetic field. Since the tokamak toroidal magnetic field is non-uniform with a radially inward gradient ($B_t \propto 1/R$, R is the tokamak major radius), a radially outward force will act on the CT. The CT will be slowed down by the magnetic field gradient force in its penetration.

3.3.3 Requirements of CT penetration into tokamaks

CT injection into a tokamak plasma consists of three stages: (1) CT formation and acceleration; (2) CT translation in a drift tube, and (3) CT penetration into the tokamak magnetic field. As a CT is injected radially from the low field side of the tokamak, the kinetic energy of the CT is reduced in displacing the spatially growing magnetic field of target tokamak. The CT slows down and, if the field strength is large enough, the CT will stop or even be reflected. The penetration distance is considered as the point where all of its kinetic energy is used up. Therefore, the initial velocity must be sufficiently high to overcome the retarding force due to the toroidal gradient in the tokamak. Thus, the basic requirement for CT central fuelling a tokamak is that the CT kinetic energy density should exceed the tokamak magnetic field energy density. This can be described as:

$$\frac{1}{2}\rho_{CT}V_{CT}^2 > \frac{B_t^2}{2\mu_0}, \tag{3.25}$$

where ρ_{CT} is mass density of the injected CT, V_{CT} the CT initial velocity, and B_t the field strength in the core of the target tokamak. Typically $\rho_{CT} > \rho_{tok}$; the required V_{CT} is less than the Alfvén velocity in the tokamak discharge.

In practice, a CT has a finite lifetime caused by resistive decay of its internal fields. The time for a magnetic field to diffuse through a characteristic distance l is:

$$\tau_{CT} = \mu_0 l^2/\eta, \tag{3.26}$$

where η is the classical Spitzer resistivity,

$$\eta = 1.65 \times 10^{-9}\frac{Z_{eff}\ln\Lambda}{T_e^{3/2}(\mathrm{keV})}\ (\Omega\cdot\mathrm{m}). \tag{3.27}$$

Substituting into Eq. (3.26) and replacing l by the inverse of the Taylor eigenvalue $1/\lambda \sim r/5$, where r is the radius of the CT, we obtain a CT lifetime of [5]:

$$\tau_{life} = \frac{30.5\, r_{CT}^2 T_e^{3/2}(\mathrm{keV})}{Z_{eff}\ln\Lambda} \propto r_{CT}^2, \tag{3.28}$$

where $\ln\lambda = 31 - \ln(\sqrt{n_{CT}}/T_e)$ can be used for simple estimation. According to Eq. (3.28), a larger CT will have a longer lifetime.

In the case of tokamak fuelling by CT the CT lifetime must be sufficiently long relative to its penetration time in the tokamak plasma. This can be described as:

$$\tau_p \ll \tau_{life}, \tag{3.29}$$

where τ_p is the time of CT propagation to the stopping point, $\tau_p \sim L_p/V_{CT}$, where L_p is the CT traveling distance before stopping and V_{CT} is the CT initial velocity.

In USCTI, lifetime of the CT is estimated as 20 μs based on the typical values of CT density, $\bar{n}_{CT} \sim 2.5 \times 10^{21}\,\mathrm{m}^{-3}$ and temperature $T_e \sim 10$ eV [37-38]. The CT traveling time is about 7 μs, assuming $L_p = 100$ cm and $V_{CT} \sim 150\,\mathrm{kms}^{-1}$. It is clear that the requirement of (3.29) is satisfied.

3.3.4 CT motion in an external magnetic field

It is important to understand CT motion in the drift tube and tokamak chamber embedded in a tokamak magnetic field. The study is vital for understanding the orientation of the injected CT in the target tokamak magnetic field; and the interactions between the injected CT with the static transverse magnetic field through comparison with theory [4-5]. This issue has been studied both theoretically and experimentally [39, 81] in the drift tube as well as the tokamak chamber (without tokamak plasma). The results demonstrated complicated behavior of CTs.

Before the injected CT enters a tokamak chamber, the CT will travel in a drift tube. The drift tube serves as an interface between the barrel of an injector and the port of the tokamak chamber. The CT motion in the drift tube embedded in an external magnetic field can be understood by taking the two fluid effect into consideration. Figure 3.10 shows a schematic diagram of the drift and the CT injector acceleration regions. The CT plasma ($+z$) and the external magnetic field ($+x$) are directed as shown here. As a moving CT plasma with velocity $\vec{u}$ encounters a transverse magnetic field, a polarization electric field $\mathbf{E}_y = -\mathbf{u}_z \times \mathbf{B}_{ext}$ is set up in the y direction because the electron and ion fluid drifts are in opposite directions (Figure 3.10(b,c)), but $\mathbf{E}_y$ is shorted out when a cylindrical conductor is present (Figure 3.10(d)). The Lorentz force $\mathbf{J}_{gun} \times \mathbf{B}_{ext}$ between the return gun current $\mathbf{J}_{gun}$

along the z axis and $\mathbf{B}_{ext}$ diffusing inside the CT is responsible for the shift in the y direction.

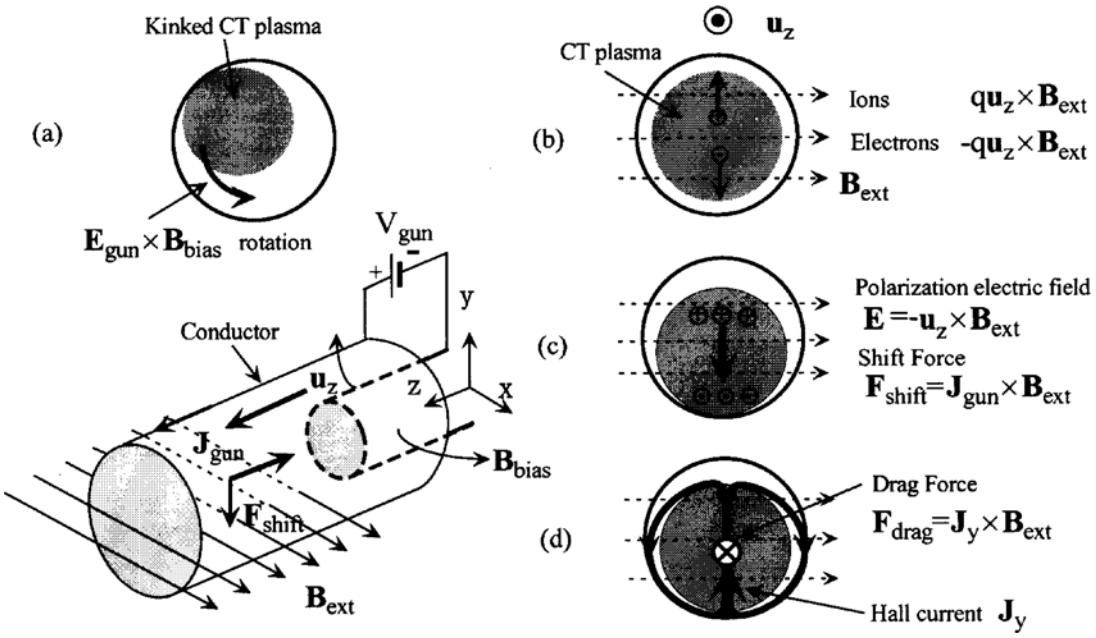

Figure 3.10: Schematic diagram of the drag and shift mechanisms. (a) the helically deformed CT plasma rotates in the direction of $\mathbf{E}\times\mathbf{B}$ in the case without B_{ext}. (b) Electrons drift vertically in the opposite direction to ions. Then, a vertical electric field is produced but shorted out by the presence of the conducting drift tube. (d) The Hall current is induced by CT injection, from Nagata [39].

In the case of CT in the vacuum field of a tokamak (without tokamak plasma), the injected CT will undergo a vertical shift in the tokamak chamber [65], as shown in Figure 3.11. The shift is caused by $\mathbf{J}_{center}\times\mathbf{B}_{tok}$ force, where $\mathbf{J}_{center}$ is the current that threads the center of the CT. $\mathbf{J}_{center}$ is the unbalanced poloidal current. The shift of CT in the tokamak chamber has been observed recently in the CT injection experiments on the JFT-2M tokamak [41].

3.4 Horizontal injection

Experimental study on CT injection has been performed on several tokamaks. Different injection angles were chosen to investigate specific physical issues.

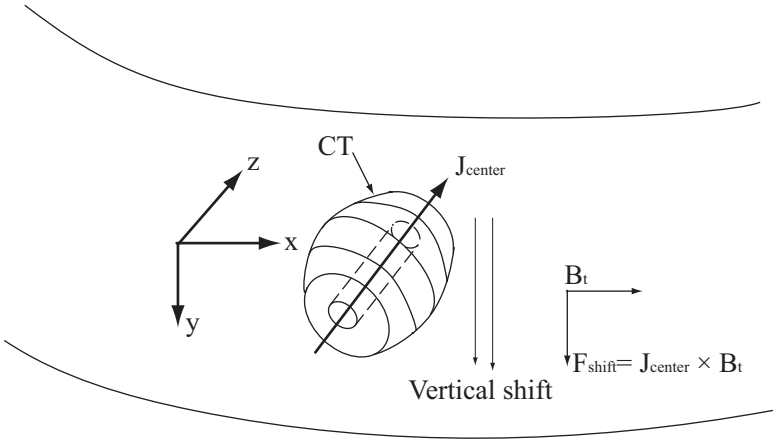

Figure 3.11: Schematic diagram of the vertical shift of an injected CT in a tokamak chamber with $\mathbf{B}_t$ alone. $\mathbf{J}_{center}$ is in the $\vec{z}$ direction and $\mathbf{B}_t$ is in the $\vec{x}$ direction. The induced vertical shift of the CT is in the $\vec{y}$ direction.

(1) Radial (normal) injection

For technical simplicity, CTs are normally injected radially, from the low field side (LFS) in the tokamak mid-plane, as shown in Figure 3.12. Various physical issues were studied in this configuration, such as core fuelling, H-mode triggering, and Alfvén wave excitation, etc.

(2) Tangential injection

In the STOR-M tokamak, CTs were injected tangentially (27° with respect to the local major radius direction, as shown in Figure 3.13. The advantage of such an angle being chosen is that the CT momentum could be transfered to the tokamak plasma. Enhancement of the tokamak plasma toroidal rotation was expected. The experiments have demonstrated that H-mode-like discharges of STOR-M plasma were triggered in this configuration [37-38].

The common feature of these experiments is the injection of CTs in the horizontal direction, from the outer board of the tokamak mid-plane. The CT has to move toward the tokamak center in the direction opposite to the magnetic field gradient force.

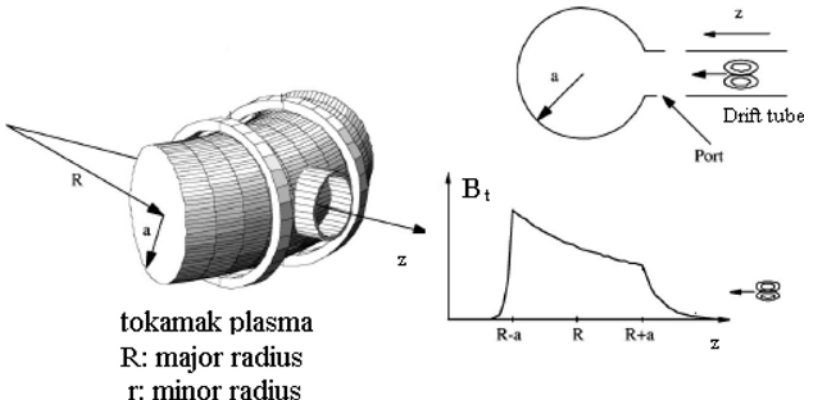

Figure 3.12: Schematic diagram of radial CT injection, from Hwang [121].

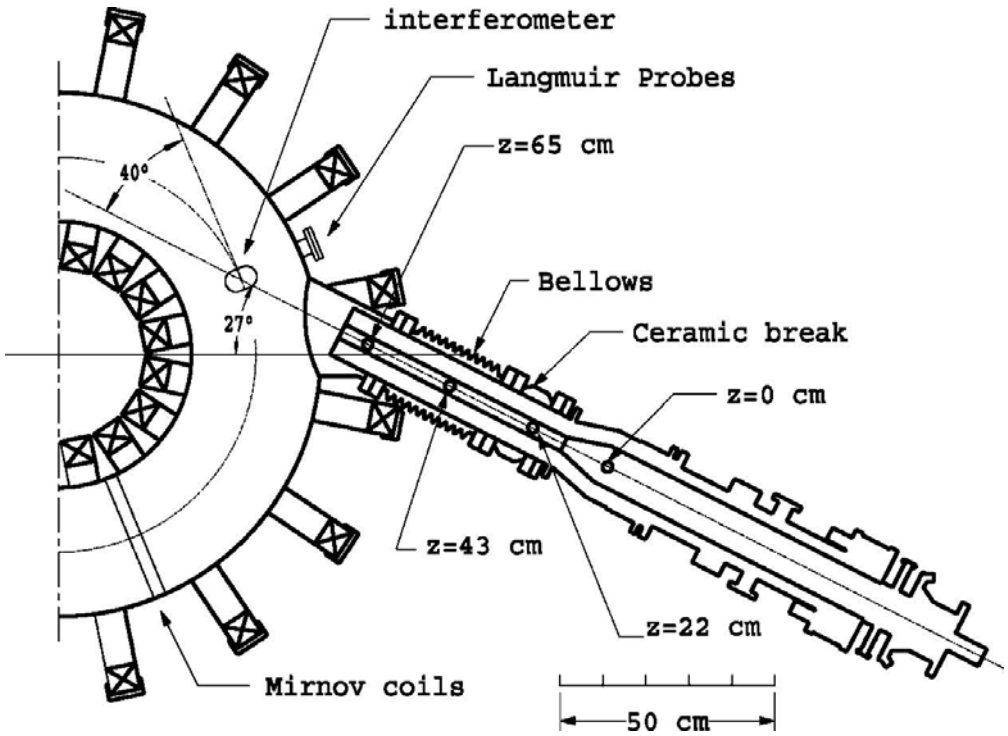

Figure 3.13: Tangential CT injection into the STOR-M tokamak, from Xiao *et al*. [37].

3.5 Vertical injection

Since there is no tokamak field gradient along the vertical direction, vertical injection was proposed to achieve deeper penetration. In this case, once a CT enters the tokamak magnetic field, its trajectory can be decomposed into two parts (assuming that the CT velocity is sufficiently high and no field reconnection occurs during its penetration): (1) in the vertical direction, the CT will move with constant velocity due to the absence of the gradient of tokamak magnetic field; (2) in the horizontal direction, the CT will be pushed towards the low field side due to the magnetic stress (∇B) force. The resulting trajectory becomes a curve as shown in Figure 3.14. Therefore, in order to deposit fuel at the center of tokamak by vertical CT injection, off-center injection (trajectory 2) might be required.

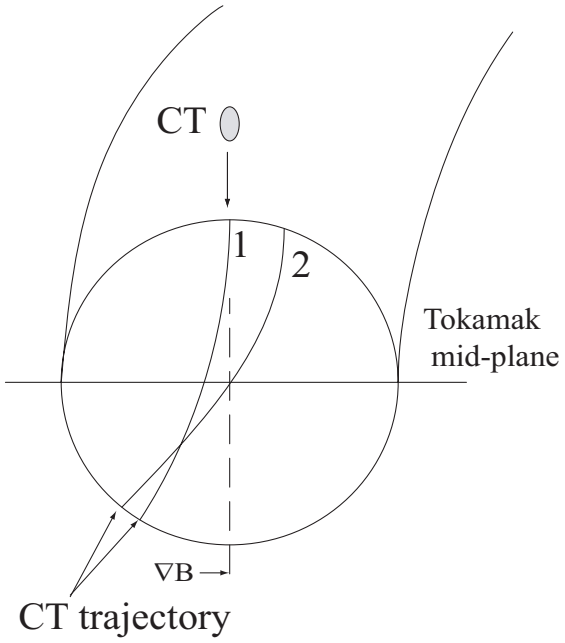

Figure 3.14: CT trajectory in vertical injection.

Chapter 4

The CT injection system on STOR-M

4.1 Introduction

Several toroidal devices have been built in the PPL over the past thirty years to study the plasma characteristics related with fusion research. These devices include the plasma Betatron, STOR-1, and the STOR-1M, STOR-M tokamaks. The construction of STOR-M was completed in 1987. Experiments in STOR-M began in 1990 and since then, some 180,000 discharges have been logged for various experiments including high confinement mode (H-mode) by turbulent heating, alternating current (AC) operation, bias induced H-modes, plasma flow measurements using Mach probes, plasma position control using a fuzzy logic digital controller, and CT injection. The CT injector, USCTI, was installed on STOR-M in 1995. Its objective is to investigate the feasibility of CT injection as a fuelling technique in future tokamak reactors. One unique feature of the USCTI is its capability to test various injection angles relative to the STOR-M toroidal field [86]. The USCTI is of the coaxial plasma gun type and acceleration of CTs is provided by the Lorentz force $\mathbf{J} \times \mathbf{B}$ in the acceleration section.

Figure 4.1 shows the side view of the STOR-M tokamak. STOR-M has a major radius $R = 46$ cm and a minor radius $a = 12$ cm. The chamber is a doughnut shaped vacuum vessel which surrounds the core of an iron transformer. A plasma current up to 50 kA is induced through transformer action which provides Ohmic heating and confinement. A combination of horizontal rail limiters at $r = 12$ cm and partial circular limiters at $r = 13$ cm near the mid-plane is made of stainless steel. This configuration allows the plasma to shift 1 cm inwards or outwards horizontally

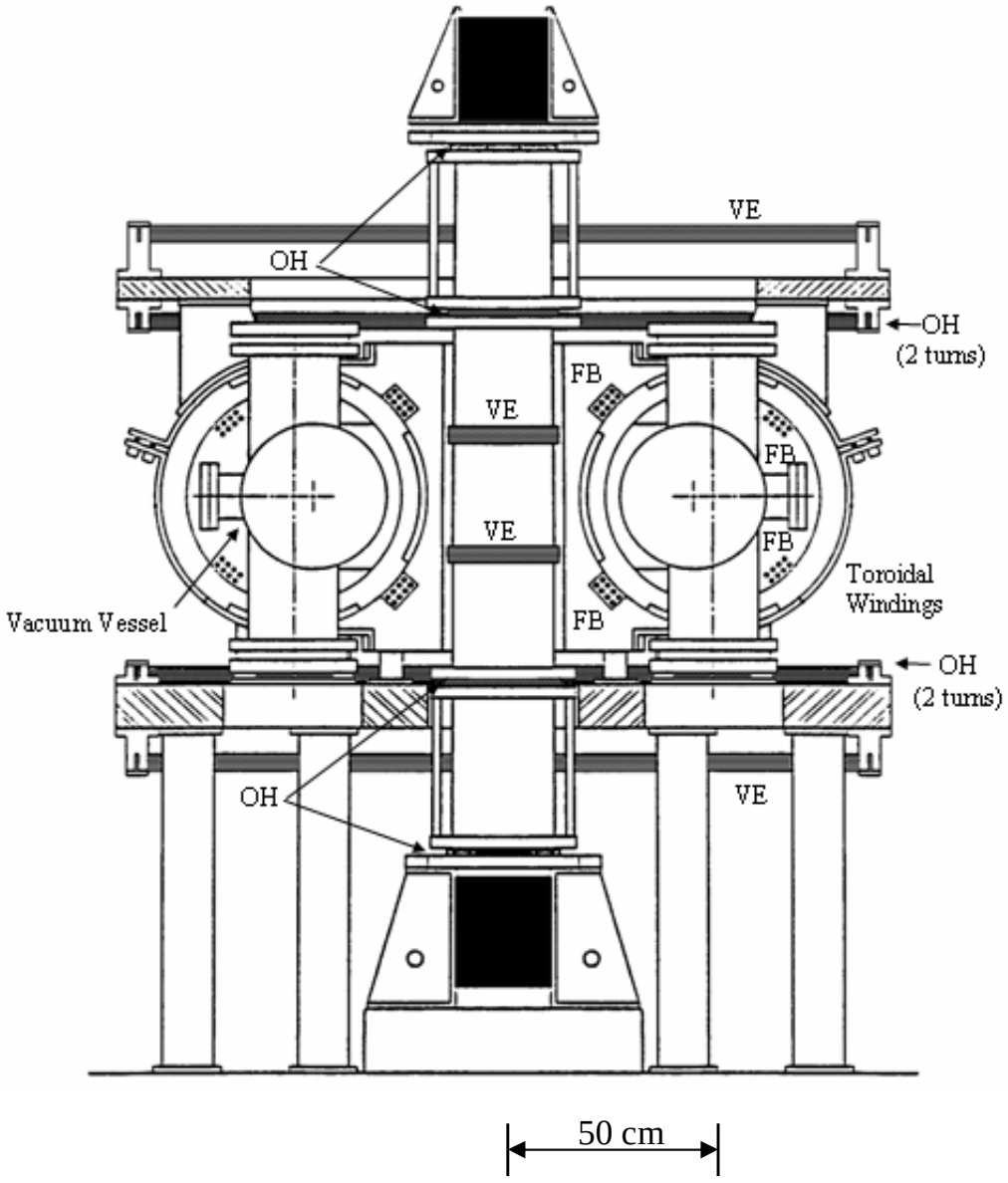

Figure 4.1: Vertical cross-sectional view of the STOR-M tokamak showing the locations of coils. OH: Ohmic primary coils (8 turns); VE: Vertical Equilibrium field coils; FB: coils for feedback plasma position control and induction coils for fast, turbulent heating current.

without being scraped off. The configuration of the limiter in shown in Figure 4.2. STOR-M is equipped with a position feed-back control system to optimize discharges. Typical parameters of the STOR-M plasma are listed in Table 4.1.

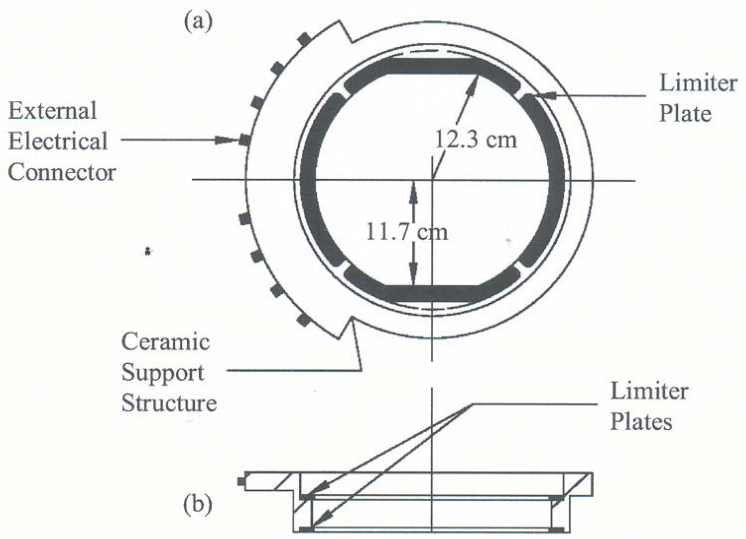

Figure 4.2: Segmented limiter (a) toroidal view (b) horizontal cross-section.

The toroidal plasma current (Ohmic current) is driven by an iron core transformer. To maximize the flux available for driving the plasma current, the transformer is first biased negatively by the bias bank. The maximum flux saving is approximately 0.1 Vs and therefore, the flux swing is ± 0.1 Vs in STOR-M discharges. The primary to secondary (plasma current) turn ratio is 8:1. A preprogrammed primary current waveform is produced by capacitor banks which include:

(a) the bias bank (450 V, 20 mF),

(b) the fast bank (450 V, 200 mF) for current ramp up, and

(c) the slow bank (100 V, 10 F) for maintaining the plasma current.

In STOR-M, the location of the primary and vertical field windings was determined so that a vertical magnetic field with an acceptable field curvature index could be produced in the region occupied by plasma, where the index is defined by $n = -\rho(d\ln B_\perp/d\rho)$ and ρ is the radius from the axis. The plasma current itself

Table 4.1: STOR-M plasma parameters

Parameters	Values
Major radius (R)	46 cm
Minor radius (a)	12 cm
Plasma current (I_p)	$30 - 50$ kA
Average electron density ($\bar{n}_e$)	$10^{18} - 10^{19}\,\mathrm{m}^{-3}$
Electron temperature (T_e)	$100 - 200$ eV
Ion temperature (T_i)	$20 - 40$ eV
Toroidal magnetic field (B_t)	≤ 1 T
Discharge duration	50 ms

creates a significant vertical magnetic field ($\sim 40\%$ of that required for equilibrium) due to the image current in the iron core. A toroidal magnetic field up to 1 T is produced by 16 air cooled coils each consisting of 9 turns of copper windings. Mylar is used for internal insulation and each coil is reinforced by layers of fibre-glass impregnated with epoxy. The inductance of the coils (connected in series) is 2.06 mH and the resistance is 13.5 mΩ (at room temperature). The toroidal magnet is powered by a 7 kV(max)/15 mF capacitor bank (maximum energy 350 kJ) through an ignitron. Passive crowbarring is provided by a set of high voltage diodes. The circuits of toroidal field coil and Ohmic heating of STOR-M are shown in Figure 4.3.

Figure 4.4 shows the ports on the STOR-M vacuum chamber for pumping, gas feed, CT injector, and major diagnostic instruments. The toroidal angle for each port is indicated. The central hatched circle represents the ion core of the transformer. The vacuum chamber (5 mm thick 304L stainless steel) of STOR-M consists of two halves insulated in the toroidal direction by two ceramic breaks. The purpose of the limiter (stainless steel) is to reduce plasma-wall interaction by keeping the plasma boundary away from the vacuum chamber wall.

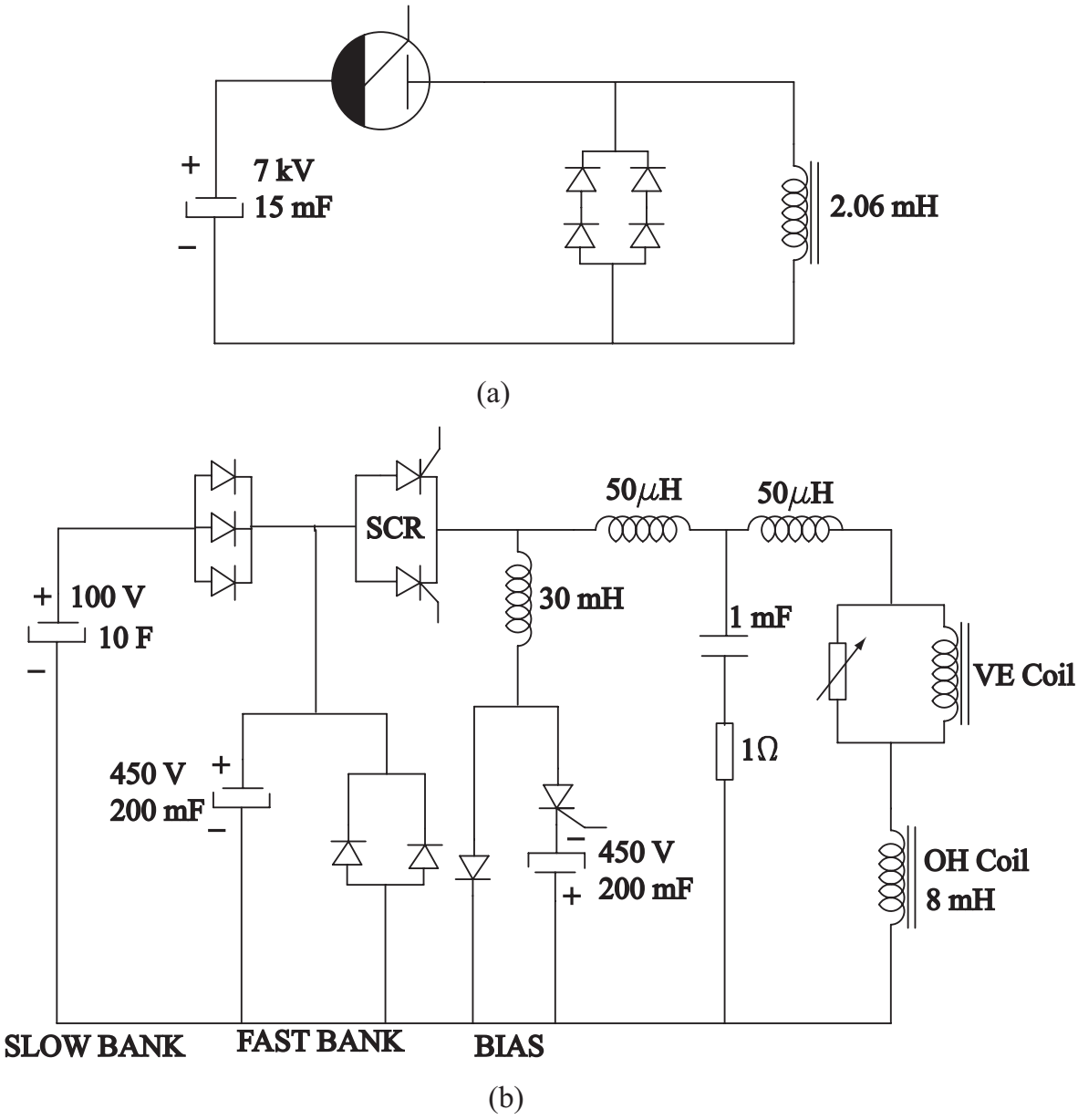

Figure 4.3: STOR-M toroidal field coil and Ohmic Heating circuits. (a) Toroidal field coil circuit and (b) Ohmic Heating circuit.

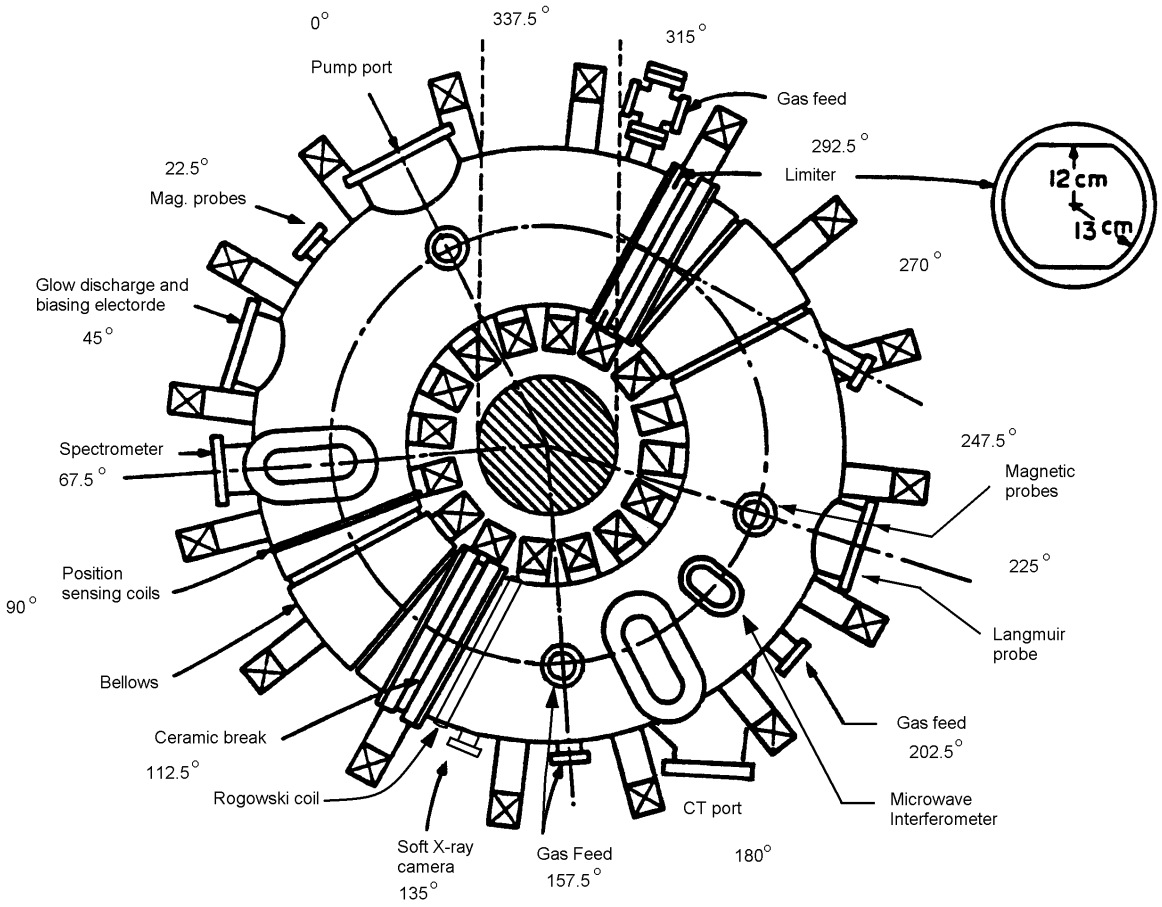

Figure 4.4: Top view of STOR-M showing the access ports and limiter geometry. The stainless steel limiter (3 mm thick) is inserted normal to the toroidal direction. It allows horizontal plasma displacement up to ± 1 cm without being scraped off.

4.2 Description of the CT Injector

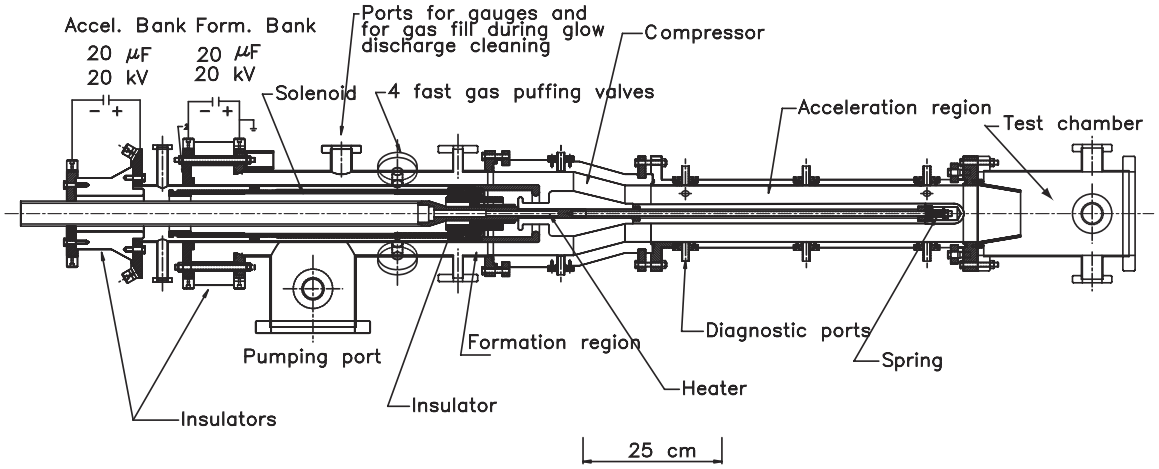

Figure 4.5: Layout of the USCTI injector. A test chamber is attached at the exit of the acceleration section.

The layout of the USCTI is shown in Figure 4.5. Two sets of identical capacitor banks of 20 kV, 20 μF are employed for consecutive formation and acceleration discharges with a time delay of several microseconds. The plasma gun consists of formation, compression, acceleration and focusing sections in a coaxial configuration. The outer and inner electrode radii are 5 cm and 1.78 cm, respectively. An internal solenoid was used to produce a quasi-steady state bias magnetic flux ($\Psi_{bias} \leq 1.8\,\mathrm{mWb}$) for CT formation. Normally, pure hydrogen gas (99.999%) is injected into the circular gap between the inner and outer electrodes through four fast electromagnetic valves evenly spaced azimuthally around the outer formation electrode. After a CT is formed through gas breakdown, it enters the compression section with a length of 91 mm and compression ratio of 1.46. The CT radius changes from 74 mm to 50 mm. The acceleration section is 60 cm long. A cone is used as the exit of the acceleration section to further compress the CT to a smaller size. The surfaces of the electrodes are coated with either tungsten or chromium to minimize impurity content in the CT. The electrodes are routinely baked to a temperature of $\sim 70^{\circ}$ with heating tapes. Four diagnostic ports along the acceleration section ($z =$ 0, 22, 43, 65 cm) are employed to mount magnetic probes to detect CT magnetic

Table 4.2: Parameters of CT at the exit of the USCTI acceleration section.

Parameters	Valus
Radius	5 cm
Length	~ 15 cm
Density (n_{CT})	$1 - 4 \times 10^{21}\,\mathrm{m}^{-3}$
Electron temperature	≤ 10 eV
Magnetic field	~ 0.2 T
Velocity (V_{CT})	$\sim 150\,\mathrm{kms}^{-1}$
Mass	$\leq 1\mu$g

fields at the outer walls in both poloidal and toroidal directions. One pair of holes in the outer acceleration electrode is used to measure CT density using a He-Ne laser interferometer.

The estimated lifetime of the CT produced by USCTI is about 20 μs based on the size (7.4 cm radius in the formation region) and the Spitzer resistivity of the CT. Typical CT parameters at the exit of the acceleration are listed in Table 4.2.

4.2.1 Vacuum and gas feed system

The outer electrode of formation and acceleration also serve as the vacuum chamber in off-line testing (CT formation and acceleration without connection to STOR-M). Such a test is important to characterize CTs. The seals between the inner and outer electrode sections are formed with viton o-rings. The o-ring grooves were designed so that the surface around the o-ring would make contact as the o-ring is compressed. In tangential CT injection experiments, one electrical break and two segments of bellows (both with 20 cm diameter) are joined in series with one end connected to the flange at the beginning of the acceleration section and the other end connected to the STOR-M port (see Figure 3.13). The barrel of USCTI located coaxially inside the bellows and the break, which isolates the two vacuum and electrical systems for

STOR-M and USCTI.

The stainless steel section of the formation electrode is also the location of the vacuum pumping ports and gas feed systems. At the bottom of the stainless steel piece there is a 20 cm diameter (8 inch) pumping port. Attached to the bottom pumping port is a gate valve and a turbo molecular pump (TURBOVAC 450) with a pumping speed of 450 l/s. The ultimate base pressure achieved is about 1×10^{-7} torr. A pumping line is connected to bypass the gate valve. This provides a throttle for the pumping rate during glow discharge cleaning. The other ports of the stainless steel electrode were designed as observation ports and for pressure gauges during the experiment. These ports contain an ionization and convectron vacuum gauge and a third location is available for residual gas analysis during glow discharge cleaning.

The magnetic probe ports in both the formation and acceleration region are sealed with viton o-rings. The surface of the probes are mounted flush with the inside surface of the electrodes to prevent disturbance to the CT and avoid arcing. In order to avoid erosion and degradation of the o-rings, they are recessed behind protective lips.

The quartz windows on both the formation and the acceleration region are sealed with o-rings. These o-rings are well away from the plasma and have no direct line of sight to the plasma. Each seal is made by clamping the window against the o-ring, which is sealed in a groove in the copper.

4.2.2 Electrical system

Figure 4.6 shows the system block diagram. A control system is in charge of providing trigger pulses in the proper time sequence for USCTI operation.

The electrical system of the USCTI consists of four categories [87]. These categories are divided along the lines of a separate capacitor bank for four systems:

(1) the formation capacitor bank for CT formation,

(2) the acceleration capacitor bank for CT acceleration,

(3) the solenoid capacitor bank for producing Ψ_{bias},

(4) the gas puff valve capacitor bank for injecting hydrogen.

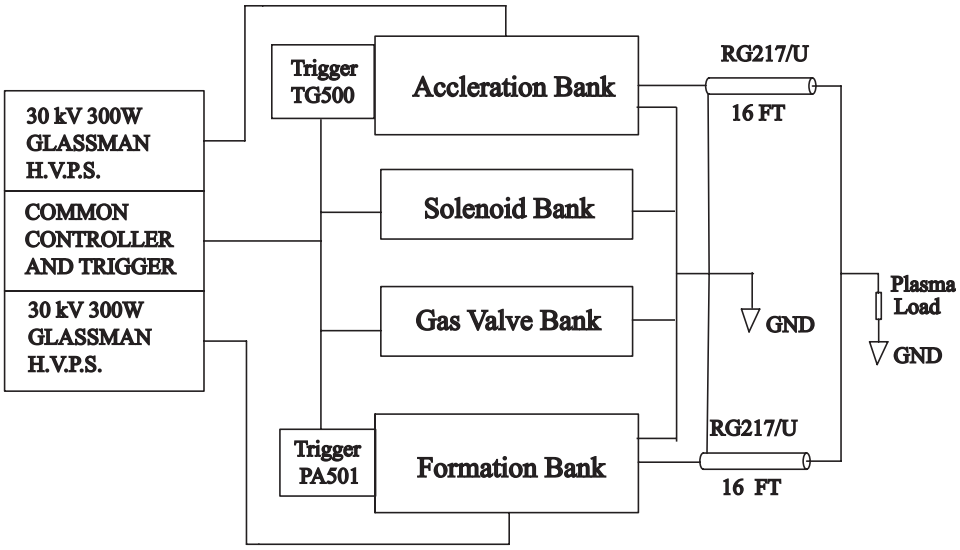

Figure 4.6: USCTI system block diagram.

The energy of the formation bank is used to break down the gas into a plasma, heat the plasma and form part of the magnetic structure of the CT. The formation capacitor bank consists of four identical capacitors (5 μF, charged up to 30 kV), each switched by an "A" sized ignitron (NL-7703EHV). The energy stored in the capacitor bank is delivered to the gun by sixteen RG217/U coaxial cables, each 5 m long. The total resistance of the system is 20 mΩ, which includes a 5 mΩ plasma resistance. The total inductance of the cables, capacitors and ignitrons is 160 nH. Formation of the CT occurs in the microsecond timescale and the formation capacitor bank must be able to deliver the energy quickly. Minimizing the inductance in the formation capacitor bank was important in its design. Figure 4.7 shows the circuit of formation bank and power supply. Its equivalent circuit is shown in Figure 4.8.

The requirement of the acceleration section is that it impart the CT with sufficient kinetic energy to penetrate the toroidal magnetic field of the tokamak. The acceleration capacitor bank is same as the formation bank. A set of four identical capacitors of 20 μF (total), 20 kV, provides the stored energy of 4 kJ (maximum) used for CT acceleration. This value is much higher than the magnetic field energy (0.23 kJ, assuming typical CT size); therefore, the CT is able to penetrate the STOR-M toroidal field (0.7 T). The acceleration phase of the gun occurs on a very short time scale and, again, it is important that the inductance of the acceleration

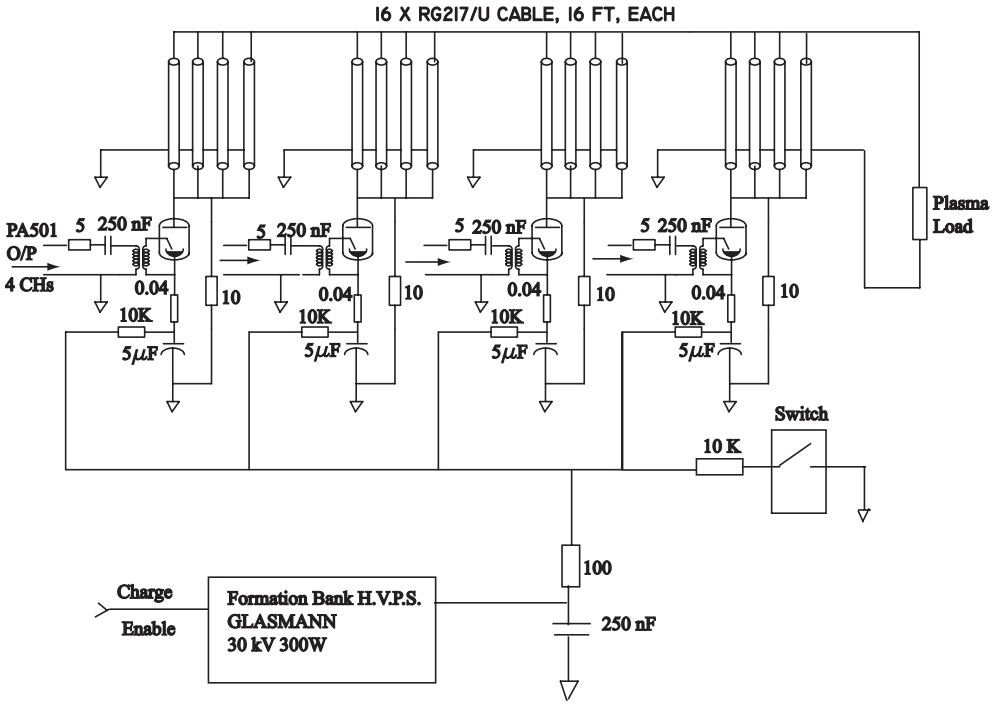

Figure 4.7: Formation bank and power supply.

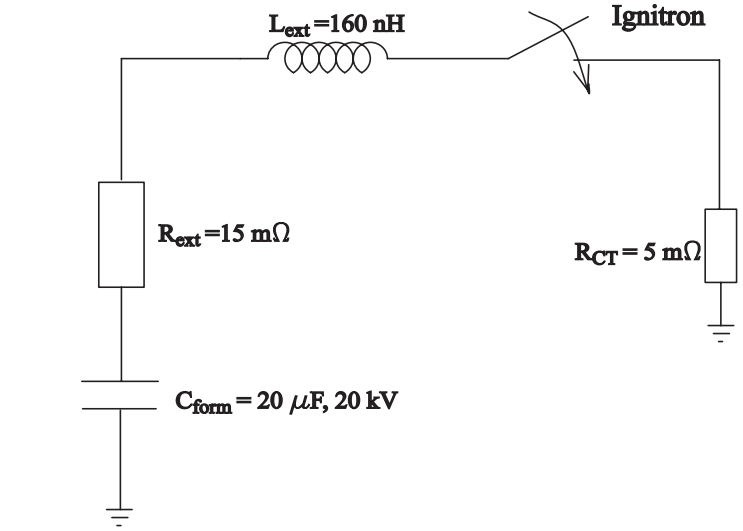

Figure 4.8: Equivalent circuit of the formation bank.

capacitor bank is delivered by sixteen RG217/U coaxial cables, each 5 m long. The total resistance of the system is 20 mΩ, which includes a 5 mΩ resistance for the plasma. The inductance consists of two parts. The first part (160 nH) comes from the cables and ignitrons; the second part is time dependent, as caused by the CT. The equivalent circuit of acceleration bank is shown in Figure 4.9.

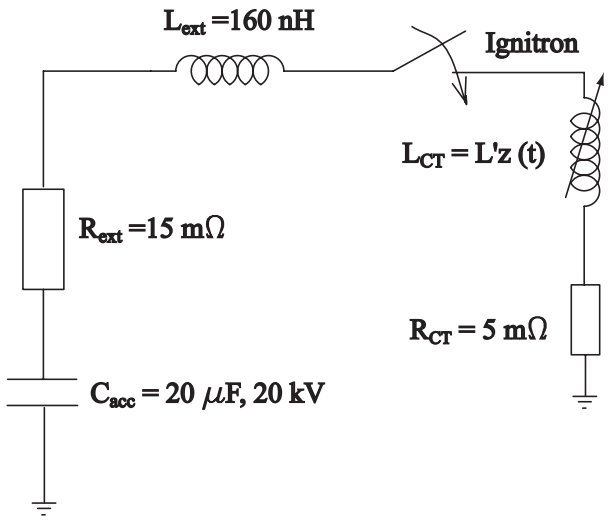

Figure 4.9: Equivalent circuit of the acceleration bank.

The solenoid produces an approximately radial magnetic field in the formation region (see Figure 3.4(1)). To form a CT, this magnetic field must penetrate the stainless steel walls of the formation electrodes prior to formation discharge. The magnetic field diffusion time for the two electrodes combined is 0.55 ms. The measured LC transient rise time for the solenoid is about 1.83 ms. Energizing the solenoid 1.83 ms before the formation capacitor bank is discharged will allow the solenoid magnetic field to peak during the formation phase. The solenoid capacitor bank must be able to maintain the solenoid magnetic field long enough to allow CT formation. This is done by a 5 mF capacitor bank that has a maximum operating voltage of 1 kV, resulting in a maximum magnetic flux of 1.8 mWb. The solenoid is made of AWG #13 wire and has 263 turns. It has a length of 50.8 cm and a diameter of 7.62 cm. The solenoid capacitor bank is switched by a silicon controlled rectifier (SCR, N330CH24).

The capacitor bank for the gas puff valves was designed to deliver a short pulse

of current to briefly open the valves. There are four valves which are powered by a 200 μF 1 kV capacitor bank. The bank is switched by an SCR (R185CH12FKC).

Since CT formation and acceleration involve high voltage and large current discharges, care must be taken to avoid ground loops which could cause troublesome spurious signals and can even damage or destroy instruments. In USCTI several methods are adopted to avoid ground loops. (1) Only one grounding point is provided for all bank systems, the control system and the injector. The power supply for each bank charging system is connected through an isolation transformer so that no direct connection exists between the grounds of the devices. (2) Optical fibers are used to send all trigger signals. (3) RC filters are inserted wherever needed.

4.2.3 Gas valve

Hydrogen gas for the USCTI discharge is injected into the formation region by four fast gas valves. These valves were originally designed by UC-Davis, CTIX group [88]. Commercially available fast gas valves such as fuel injectors were considered for this application, but they do not react fast enough. The optimum gas injection pulse should have steep rising and falling edges in the microsecond timescale, so that the gas injection time is well defined. If the valve does not close fast enough, gas will continue to enter the formation region after the CT has been formed, which leads to an increasing gas load.

The gas valve, shown in Figure 4.10, works on the principle of magnetic induction. The valves consist of a small coil of wire underneath a spring loaded piston. When the coil is energized a diamagnetic current forms in the piston resulting in a repulsive force between the coil and piston. The force lifts the piston from an "o" ring seal, allowing gas to flow from the cavity above the piston. The cavity is fed with gas through a 6 mm stainless steel tube and is connected in series with the other three valves. The action of the piston can be adjusted by changing the compression of the spring, thus allowing the gas flow of each valve to be same with the others. The "valve equalizing" is of importance to the consequent CT formation and to produce CTs with good quality for the injection experiments.

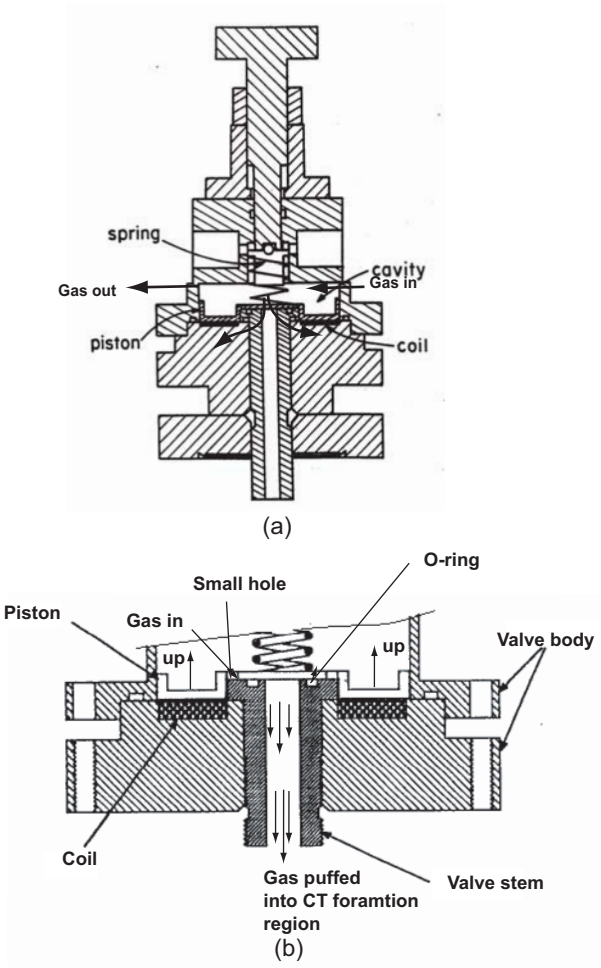

Figure 4.10: (a) Schematic view of the fast gas valve used in USCTI and (b) showing the gas puffing process.

The typical pulse width in the valve "opening" state is about 300 μs. Approximately 10^{19} particles [88] per valve giving a total of about 4×10^{19} particles are injected per discharge. The amount of gas injected decreases with the increasing gas pressure behind the valve. An adequate number of particles can be trapped during formation if the the gas spreads out 12 cm on either side of the gas valves. With this parameter and the the neutral hydrogen transit time of 0.1 cm/μs, it takes only about 120 μs to fill the formation region. The time delay between gas puffing and formation bank discharge is 200 μs, which is long enough to achieve even gas distribution along the formation circumference to produce quality CT formation discharges.

4.3 Diagnostics of CT injection into STOR-M

The progress toward improved fusion parameters of the past three decades has been paralleled by improvements in our understanding of hot plasmas. Essential to this development, and the principal contributors, have been the impressive advances in techniques for measuring plasma properties, collectively referred to as "plasma diagnostics" [89]. The diagnostics of a hot plasma has become a branch of fusion research. All plasma measurements are intrinsically difficult, for the high temperatures preclude the insertion of any instruments. The techniques must be noninvasive to minimize disturbance. They may be passive using the natural emission of radiation or particles, or they may be active, observing the effect of the plasma on a source of applied radiation or particles; but the interaction must be weak in the sense of not perturbing the system, for example, spectroscopy, interferometry, etc. In STOR-M and USCTI, both of these kinds of diagnostics are employed to measure both the CT plasma and the STOR-M plasma.

4.3.1 Diagnostics of CT plasma

Diagnostics in the USCTI includes gun voltage, gun current, internal magnetic fields of CT, CT velocity, density, electron temperature, and optical radiation of CTs. Due to the high velocity of CTs, typically 150–200 kms^{-1} in USCTI, signal detection and data acquisition with high temporal resolution (μs timescale) are required to characterize CT plasma, e.g. CT velocity and magnetic fields. The CT velocity can be estimated by the time of flight method using a series of magnetic signals along the outer acceleration electrode.

(1) **CT magnetic fields measurement**

A magnetic probe is a commonly used technique in CT magnetic field measurement [90-91]. The probe is essentially a pick-up coil which can convert a time-dependent magnetic signal to a voltage output based on Faraday's law: the time-varying flux linked by the small coils induces a voltage at the coil terminals $V =$

$-d\Phi/dt$. Integration of V determines $\Phi\,(= \int \mathbf{B} \cdot \mathbf{ds})$ and hence the magnetic field B linked to a magnetic probe. The design points and probe applications in fusion plasma research are well described in extensive literature [98-109]. In USCTI, the CT magnetic fields were measured in both the formation region (four probes evenly spaced poloidally with 90° apart) and acceleration region (z = 22, 43, 65 cm respectively), as shown in Figure 4.11. At each location, there are two coils perpendicular to each other to measure CT magnetic field components B_z and B_ϕ. Each coil was wounded on a delrin form with a 4 mm radius. The form is machined in such a way that a recess was made to wind the wire easily. Each miniature pick-up coil consists of a 6 turn winding (AWG#32 wire) with a cross-section of 8 mm × 3 mm (see Figure 4.12). Each set of probes is protected by a ceramic holder mounted in the outer walls of electrodes. Passive integration ($\tau_{RC} = 50\,\mu$s) is used to recover the B signal since this method is the simplest and least susceptible to noise.

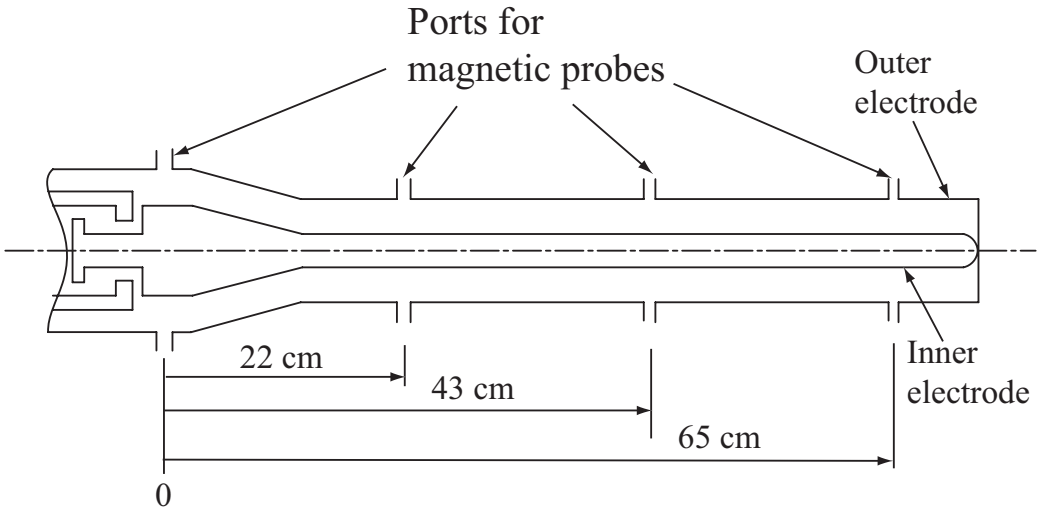

Figure 4.11: Magnetic probe arrangement in USCTI.

(2) **CT density measurement**

(a) Langmuir probe

Since a CT is a low temperature, high density plasma, the simplest way of CT density measurement is to use a Langmuir probe. Langmuir probes are small conductors with well-defined surface area that are inserted into the plasma for the purpose

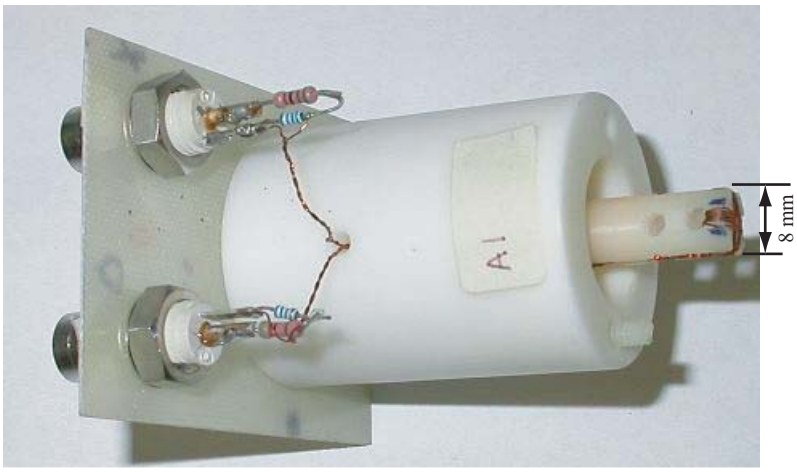

Figure 4.12: Photo of the magnetic probe in USCTI.

of collecting electrons and ions. The Langmuir probes are simple to construct, easy to use and can provide excellent spatial resolution.

A single Langmuir probe is essentially a conductor inserted into the plasma and biased relative to the chamber wall so that a plasma sheath develops around the conductor. By assuming a Maxwellian distribution for the undisturbed electrons and ions, and further ignoring the effect of magnetic field, the current density flowing into the conductor surface is approximately given by [92]

$$J = J_i - J_{e0}(1-\Gamma)e^{e(V-V_s)/T_e},\ V < V_s, \tag{4.1}$$

where J_i is the ion saturation current density, J_{e0} is the electron saturation current density, Γ is the secondary emission rate of the probe conductor, V is the probe potential and V_s is the plasma space potential. For tungsten, Γ is negligible small.

When the probe potential V is higher than the plasma space potential V_s, i.e., $V > V_s$, the probe current is limited by the electron saturation current:

$$I_{e0} = \frac{1}{4} e n_e A \sqrt{8T_e/\pi m_e}, \tag{4.2}$$

where A is the electron collection area, T_e is the electron temperature in eV units, and n_e is the electron density. Decreasing the probe potential, $V < V_s$, the electron current is modified by the Boltzmann factor $\exp[(V - V_s)/T_e]$. When the electron current is further reduced to be equal to the ion current, the total current will become

zero. This occurs at the floating potential V_f,

$$V_f = \frac{T_e}{e} \ln \left(0.66 \sqrt{\frac{M_i}{m_e}} \right). \tag{4.3}$$

Decreasing the bias potential further, only ions are eventually collected, and probe current reaches the ion saturation current I_{sat}, which is given approximately as follows:

$$I_{sat} = a\, A\, e n_e \sqrt{T_e / m_i}, \tag{4.4}$$

where $a = \exp(-1/2) = 0.61$ and m_i is the ion mass.

Various plasma parameters described above may be determined from the equation. For practical use, a multi-probe system was developed to make simultaneous measurement of local plasma parameters. The most convenient usage is a triple Langmuir probe [93-97]. Figure 4.13 Shows the principle of the triple probe.

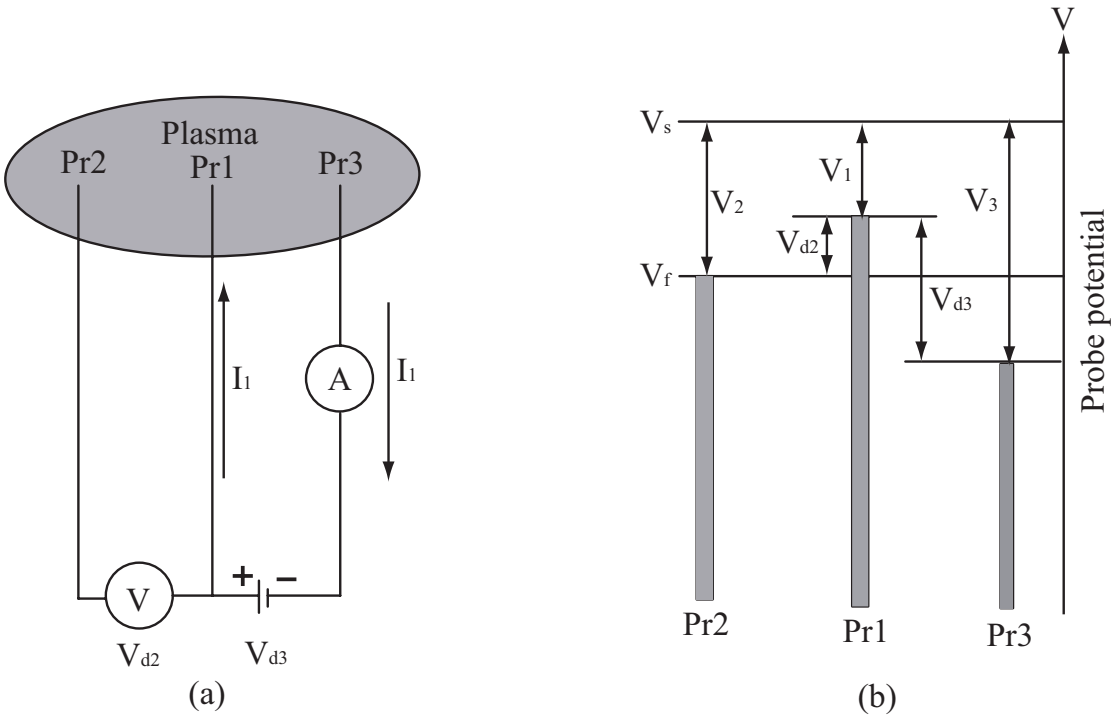

Figure 4.13: (a) Triple probe circuit and (b) potential of each probe.

Three probes Pr1, Pr2, and Pr3 are inserted into the plasma, as shown in Figure 4.13(a). A constant voltage V_{d3} is applied between Pr1 and Pr3 and the probe current is I_1. Let V_{d2} denote the potential difference between Pr1 and Pr2. If we

assume that the plasma space potential V_s is uniform in the region of probes and let V_1, $V_2(\equiv V_f - V_s)$, and V_3 express the potential difference of probes from V_s (note $V_i < 0$, $i = 1, 2, 3$), as shown in Figure 4.13(b), then we have,

$$V_{d2} = V_2 - V_1, \tag{4.5}$$

$$V_{d3} = V_3 - V_1. \tag{4.6}$$

The currents flowing into the three probes can be written as

$$-I_1 = -I_{e0} \exp\left(\frac{V_1}{T_e}\right) + I_{sat}, \tag{4.7}$$

$$0 = -I_{e0} \exp\left(\frac{V_2}{T_e}\right) + I_{sat}, \tag{4.8}$$

$$I_1 = I_{e0} \exp\left(\frac{V_3}{T_e}\right) + I_{sat}. \tag{4.9}$$

Combined with Eq. (4.4) and (4.5), Eqs. (4.6)-(4.8) can be solved with respect to T_e and I_{sat}:

$$\frac{1}{2} = \frac{1 - \exp(-V_{d2}/T_e)}{1 - \exp(-V_{d3}/T_e)}, \tag{4.10}$$

$$I_{sat} = I_1 \frac{\exp(-V_{d2}/T_e)}{1 - \exp(-V_{d2}/T_e)}. \tag{4.11}$$

In the limit of $T_e \ll V_{d3}$, Eq. (4.9) and (4.3) become

$$T_e \simeq \ln 2(eV_{d2}) = 1.44 eV_{d2}, \tag{4.12}$$

$$n_e = \frac{I_1}{eA\sqrt{T_e/m_i}}. \tag{4.13}$$

If the probe current I_1 and voltage V_{d2} are monitored, the electron temperature T_e and electron density n_e can be obtained. The time resolution of T_e and n_e measurements are only limited by the data sampling rate.

In USCTI, the triple probe technique is used to measure CT density. The triple probe consists of a set of three adjacent identical Langmuir probes. A ceramic tube with 5 mm in diameter and 60 mm in length is used as a probe housing. The tube has three axial through holes. Three tungsten wires (diameter = 0.5 mm) are inserted through the holes and make the probe tip 1.5 mm long for each wire. The distance

between probes 1 and 2, and probes 2 and 3 are 1.4 mm. "Torrseal" epoxy is used at the other end of the ceramic tube for vacuum tightness. Figure 4.14 shows the triple probe used in USCTI. The I_{sat} and T_e signals are digitized by a digital oscilloscope with a 50 MHz sampling rate (Tektronix TDS2014).

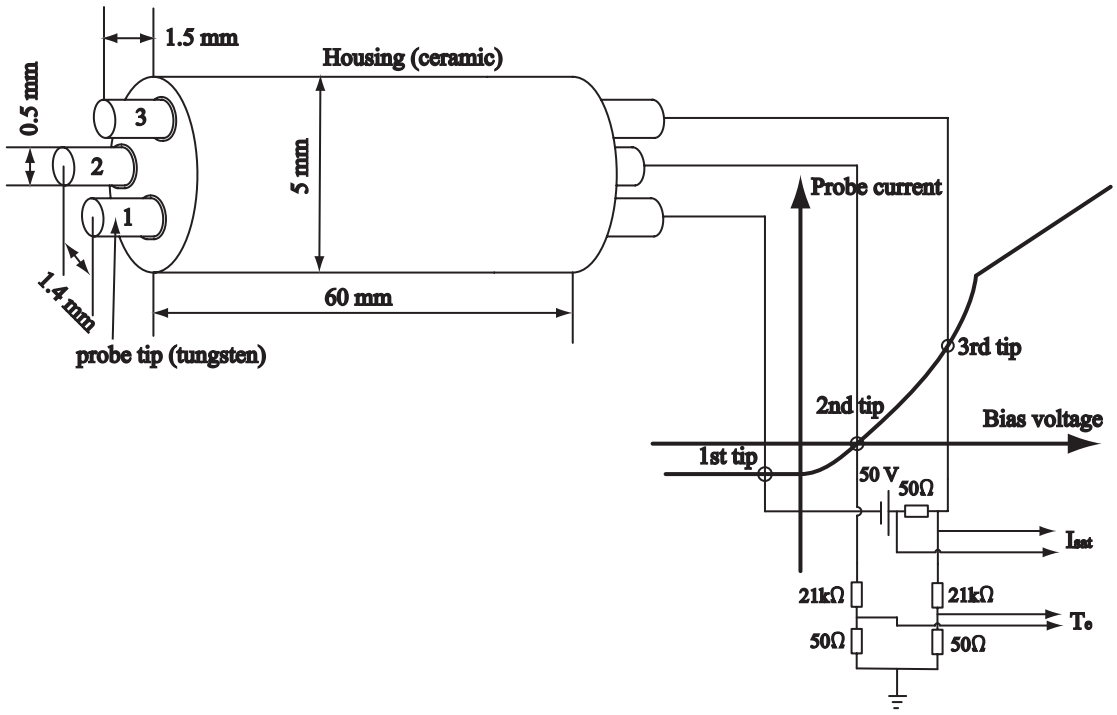

Figure 4.14: The geometry and circuit of the triple probe used in USCTI.

(b) He-Ne interferometer

The line-averaged electron density can be measured with good accuracy from the phase shift of an electromagnetic wave traversing the plasma provided the wave frequency ω is much larger than the plasma frequency ω_{pe}. Here ω_{pe} is given by

$$\omega_{pe} = \left(\frac{n_e e^2}{m_e \epsilon_0}\right)^{1/2}, \tag{4.14}$$

where e and m_e are electron charge and mass, respectively. ϵ_0 is the permittivity constant of vacuum.

Such a wave has the dispersion relation $\omega^2 = \omega_{pe}^2 + k^2 c^2$ so that the phase shift ϕ_p induced on traversing a length L of plasma is

$$\phi_p = \int_0^L k dx \approx \frac{\omega}{c} \int_0^L dx \left(1 - \frac{\omega_{pe}^2(x)}{2\omega^2}\right), \tag{4.15}$$

if $\omega^2 \gg \omega_{pe}^2$. The density of short-pulse laboratory CTs is well suited to the use of interferometers based on He-Ne lasers. A quadrature design [72, 98-99] has proved particularly useful because it provides good noise immunity and does not have phase ambiguity. The quadrature configuration involves measuring both sine and cosine components of the wave so that the phase shift can be determined using the arctangent function. Figure 4.15 shows the diagram of a quadrature density interferometer.

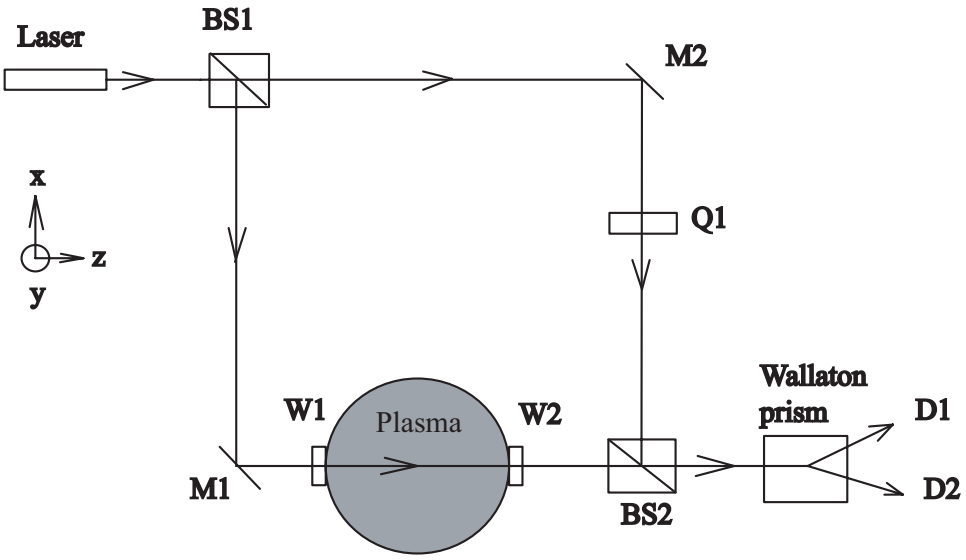

Figure 4.15: Quadrature density interferometer for CT density measurement.

The output of a linearly polarized He-Ne laser is oriented so that its **E** field is out of the plane of the page (y direction). The laser beam is divided into a plasma beam and a reference beam by a non-polarized beam splitter BS1. The plasma beam reflects from mirror M1, enters the plasma through polarization-preserving window W1, exits through polarization-preserving window W2, passes through non-polarizing beam splitter BS2 and enters the Wollaston prism. The Wollaston prism is rotated so that its axis is at a 45° angle relative to the y direction. Thus, if $\mathbf{x}'$ and $\mathbf{y}'$ are unit vectors in the Wollaston prism coordinate system, the plasma beam polarization is $(\mathbf{x}' + \mathbf{y}')/\sqrt{2}$. The reference beam reflects from mirror M2, becomes circularly polarized by the quarter wave plate Q1, reflects from beam splitter BS2 and enters the Wollaston prism co-aligned with the plasma beam.

In the Wollaston coordinate system, the plasma beam electric field is

$$\mathbf{E_s} = E_0 \frac{\mathbf{x}' + \mathbf{y}'}{\sqrt{2}} \cos(k_0 L_s - \Delta\phi_p - \omega t) \tag{4.16}$$

where

$$\Delta\phi_p = \int_0^L (k_0 - k) dx = \frac{1}{2\omega c} \int_0^L \omega_{pe}^2(x) dx \tag{4.17}$$

is the phase shift due to the presence of the plasma, L is the path length through the CT plasma, and L_s is the path length of the plasma beam from beam splitter BS to the Wollaston prism. In practical units, the phase shift resulting from passage through the plasma is

$$\Delta\phi_p = 2.8 \times 10^{15} \lambda_0 \int_0^L n(x) dx, (rad) \tag{4.18}$$

where λ_0 is the laser wavelength. In USCTI, a He-Ne laser ($\lambda_0 = 632$ nm) is used. The phase shift resulting from traversing 0.1 m of plasma with density $n = 10^{20}\,\mathrm{m}^{-3}$ will be $\Delta\phi_p = 1.8 \times 10^{-2}$ radians.

The circularly polarized reference beam has an electric field in the Wollaston coordinate system given by

$$\mathbf{E_r} = E_0[\mathbf{x}'\cos(k_0 L_r - \omega t) + \mathbf{y}'\sin(k_0 L_r - \omega t)], \tag{4.19}$$

where L_r is the path length followed by the reference beam from the beam splitter BS1 to the Wollaston prism.

The Wollaston prism deflects the $\mathbf{x}'$ components of the optical signal to be incident on the detector D1 and the $\mathbf{y}'$ components to be incident on detector D2. These detectors are PIN diodes sensitive to incident power, i.e., to $< E^2 >$. Thus, detector D1 will provide a signals

$$\begin{aligned} S_1 &= \alpha < (E_{rx'} + E_{sx'})^2 > & (4.20) \\ &= \frac{\alpha E_0^2}{2} \cos(\Delta\phi_p - k_0 \delta L), & (4.21) \end{aligned}$$

and detector D2 will provide a signal

$$\begin{aligned} S_2 &= \alpha < (E_{ry'} + E_{sy'})^2 > & (4.22) \\ &= \frac{\alpha E_0^2}{2} \sin(\Delta\phi_p - k_0 \delta L), & (4.23) \end{aligned}$$

where α is the PIN diode responsivity and $\delta L = L_s - L_r$. Thus, the mesured plasma-induced phase shift will be

$$\Delta\phi_p = \arctan(S2/S1) + k_0\delta L. \tag{4.24}$$

The value of $k_0\delta L$ is determined from measurement of $S1$ and $S2$ at the instant before breakdown. Measurement of $\Delta\phi_p$ provides the CT line-averaged electron density.

4.3.2 Diagnostics of STOR-M plasma

Macroscopic properties of STOR-M discharge, such as plasma current, loop voltage, and the plasma position can be obtained by measuring the magnetic field associated with each quantity. These measurements involve Rogowski coils for current measurements, small pickup coils for plasma position measurements, and a single turn loop for plasma loop voltage and transformer flux measurements. Some of the classical techniques (e.g. Langmuir probes and magnetic probes [98-109]) are employed to measure the edge plasma parameters. Diagnostic instruments routinely used in the STOR-M tokamak include a 4 mm microwave interferometer [110-111], a soft x-ray camera, an optical spectrometer, a set of Mirnov coils (m = 2 and 3) and a set of Langmuir probes. In STOR-M, the Langmuir probe signals (I_{sat} and V_f) are digitized at a 1 MHz sampling rate for times up to 20 ms by a digital oscilloscope (Lecroy 9314M). The principles for magnetic probes and Langmuir probes have been presented in Section 4.3.1. This Section will describe the remaining diagnostic tools equipped in STOR-M. Major diagnostic instruments equipped on STOR-M are listed in Table 4.3.

(1) **Rogowski coils**

In the STOR-M tokamak, numerous Rogowski coils are used to measure the currents in the plasma and various windings. Each coil has a frequency response up to 800 KHz, which is more than sufficient for measurements in STOR-M. The coils are calibrated with a commercial Rogowski coil (Pearson Electronics). The parameters of the Rogowski coils used in STOR-M are listed in Table 4.4.

Table 4.3: Major diagnostic tools on STOR-M

Plasma properties	instruments
Current (plasma, windings)	Rogowski coils
Loop voltage	Pick-up loop
Electron density	Microwave interferometer (2 mm, 4 mm)
Electron temperature	Soft X-ray camera, Thomson scattering
Ion temperature	Spectroscopy
MHD fluctuation	Mirnov coils, magnetic probes (edge)
Density fluctuation	Langmuir probes, microwave scattering (2 mm), microwave reflectometer (2 cm, edge)
Plasma position	Magnetic probes

Table 4.4: Parameters of Rogowski coils in STOR-M

Current measured	I_p	I_{BT}	I_{OH}	I_{VE}	I_{th}
R (Ω)	1.4	70	37	84	4
L (mH)	0.12	7.5	5.3	9.6	0.02
N (turns)	600	1187	750	1187	180
R (cm)	17	7.0	7.0	7.0	17
a (cm)	1	1.5	1.5	1.5	1
b (cm)	3.5	2.5	2.5	3.3	3.5
Calibration (kA/V)	100	10	10	10	100

(2) **Mirnov coils and position sensing coils**

Mirnov oscillations are observed during the discharge, particularly at the early stage of plasma current build-up. In the STOR-M tokamak, these oscillations are monitored routinely with two sets of Mirnov coils ($m = 2$ and 3 at toroidal location $\phi = 125°$) [112]. Essentially the coils are magnetic pick-up loops with a specific spatial arrangement. The resulting output is predominantly sensitive to the specific modes. For example, the $m = 2$ sensor consists of four coils arranged poloidally 90° apart and connected in series with polarities as shown in Figure 4.16(a). Each coils has 200 turns of wire wound on a former of area 0.9 cm^2. The frequency response of the coils is flat to 200 KHz which is sufficient for MHD signals in STOR-M ($\sim$ 27 KHz).

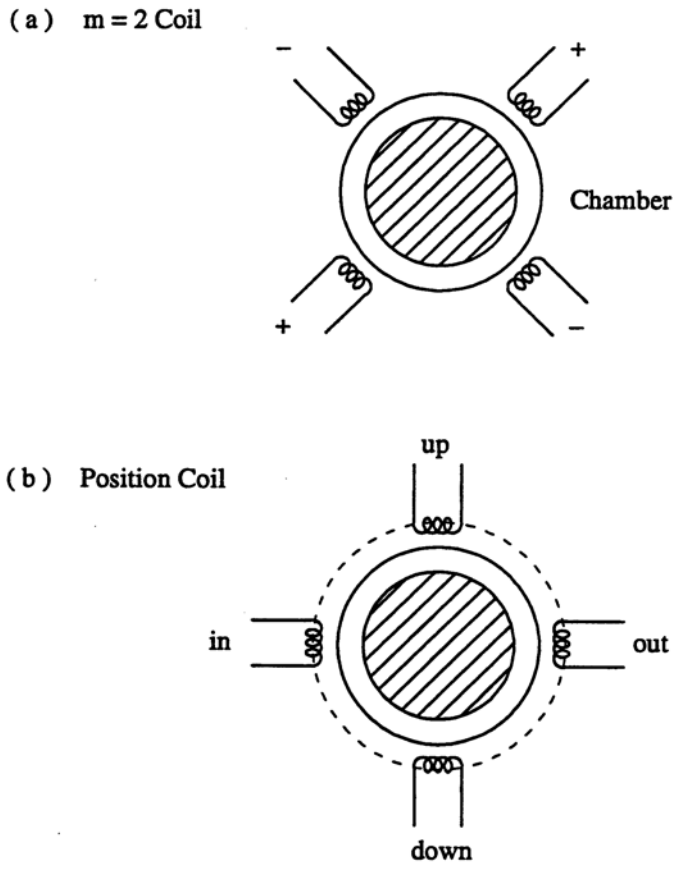

Figure 4.16: (a) Mirnov coils. (b) Position-sensing coils

Accurate control of plasma position during discharges is crucial for experiments, which requires the accurate measurement of the plasma column. In STOR-M, this was done by four magnetic probes located on a circular contour of radius $r_m = 17$ cm to detect the tangential component of the magnetic field B_θ, as shown in Figure 4.16 (b). Each coil has 460 turns of 0.1 mm diameter (AWG#38) wire wound on a cylindrical Teflon former with 90° separation. The parameters of each coil are given in Table 4.5. The frequency response extends to 200 KHz which is sufficiently high for the purpose of plasma position control. In addition, a compensation circuit was used to eliminate the unwanted signal pick-up due to imperfect and unavoidable tilting of the windings. Figure 4.17 shows the compensation circuit. Rogowski coils are used to determine the current waveforms which produce the unwanted magnetic fields. These waveforms are then added with the appropriate amplitude and polarity to the affected magnetic coil signals to cancel the unwanted potions. Pick-up of the toroidal field is usually the largest error source in tokamaks. In STOR-M, it was necessary to cancel the contribution from the toroidal fields from all magnetic probes. The contribution from the OH leakage magnetic field is sufficiently small and does not affect most of the magnetic measurements. The probe signals, after compensation, were integrated with active, gated integrators. An analog circuit then performed the comparison of the signals and yielded an output proportional to the plasma displacement [114].

(3) **Microwave interferometer**

In STOR-M, a 4 mm microwave interferometer is routinely used to measure the center chord line-averaged electron density, as show in Figure 4.18. Similar to the CT density measurement in USCTI, the microwave interferometer is of a quadrature configuration. The maximum density can be measured by this system is $n_c = 7 \times 10^{19}\mathrm{m}^{-3}$, where n_c is the cutoff density for working wavelength $\lambda = 4$ mm. n_c is given by

$$n_c = \frac{m_e \epsilon_0 \omega^2}{e^2}, \tag{4.25}$$

This system provides a direct-reading output without the requirement for source modulation [114-117]. A reflex klystron (Varian VRE-2102) operating at 75 GHz,

Table 4.5: Parameters of Position sensing coils in STOR-M

Magnetic probes	Out	In	Up	Down
R (Ω)	23.5	23.1	22.9	22.8
L (mH)	0.95	0.99	0.93	0.94
N	460	460	460	460
a (mm)	3.5	3.5	3.5	3.5
l (mm)	6	6	6	6
Calibration (G/mV)	10	10	10	10

generates the microwaves which are divided among three paths: a plasma path and two reference paths. The portion passing through the STOR-M plasma undergoes a phase shift $\Delta\phi$ related to the differing indices of refraction. After passing through the plasma, the microwave pass through an E-H tuner and are split into two waves E_{s1} and E_{s2}. Each of the two reference waves E_{r1} and E_{r2} pass through an attenuator and phase shifter before being mixed with E_{s1} and E_{s2} in hybrid tees.

The microwave detectors are MOD-ED silicon beam lead diodes (Pacific millimeter products). The output signals from the diodes are fed into buffer amplifiers with adjustable gains to compensate for the different efficiencies. The final output of the amplifiers is given by

$$V1,2 = K_{1,2}\cos\theta_{1,2} \tag{4.26}$$

where $\theta_{1,2}$ are the phase angles of the detected microwaves. If the phase shifts are adjusted correctly, these become

$$V_1 = K_1\sin(\Delta\Phi) \tag{4.27}$$

$$V_2 = K_2\cos(\Delta\Phi). \tag{4.28}$$

Output signals of this form allow a direct-reading fringe counting circuit to monitor, in real time, the line averaged plasma density. This circuit has a resolution of a quarter fringe and is described in detail by Emaami *et al.* [111, 114-115].

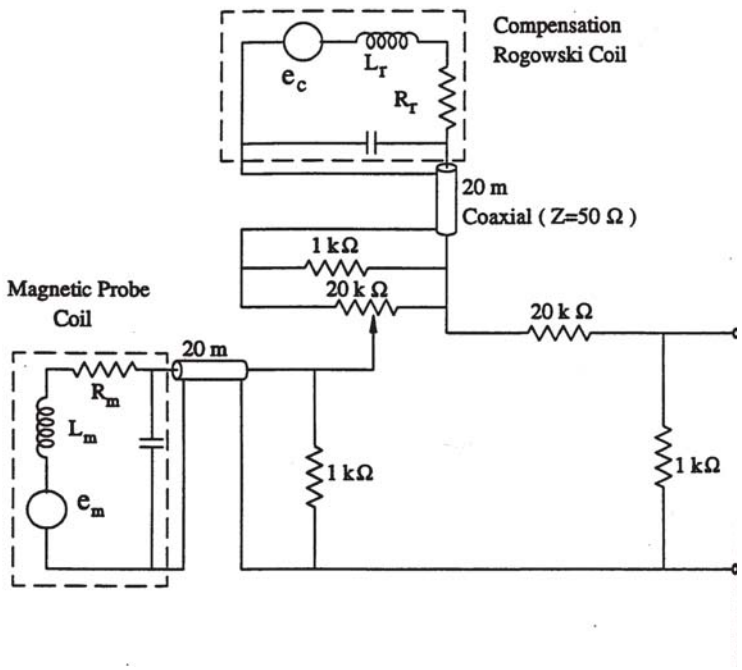

Figure 4.17: Diagram of Position-sensing coil circuit showing compensation circuit.

(4) **Soft X ray camera**

Monitor the soft X-ray (SXR, $0.1 \leq E \leq 30$ keV) emission from a tokamak plasma is a diagnostic technique that can be used to measure the electron temperature, the impurity content and the MHD activity in the plasma. There are three distinct sources of SXR in a high temperature plasma - bremsstrahlung, recombination and line radiation.

Bremsstrahlung radiation is due to the scattering of electrons by the ion Coulomb field. It is also termed "free-free" radiation because the electrons, before and after interaction, are unbounded. The spectrum of the emitted radiation is a continuum which indicates the velocity distribution of the electrons.

Recombination radiation, referred to as "free-bound" radiation, also contributes to the continuum of the emitted radiation from a plasma. This radiation is emitted when an ion of charge Z, in the ground state, captures a free electron of energy E and becomes an ion of charge $Z-1$. It then emits a photon of energy $h\nu =$

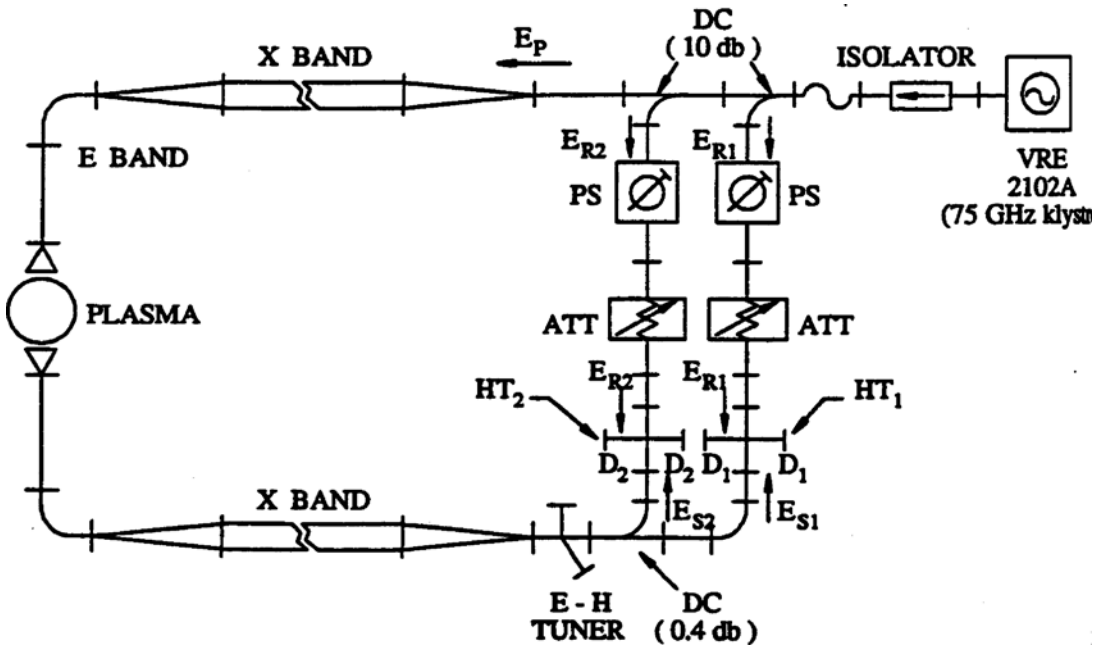

Figure 4.18: Schematic diagram of 4 mm microwave interferometer for electron density measurement in STOR-M.

$E + E_i^{Z-1}$, where E_i^{Z-1} is the ionization energy of the ion of charge $Z-1$. Similar to bremsstrahlung, the recombination radiation spectrum also indicates the velocity distribution of the electrons and is a continuum.

Another source of radiation in the SXR region is inner shell transitions in partially ionized impurities. The accompanying emission is referred to as "line radiation" and it conveys information on the species and ionization states of the impurities.

The intensity of the continuum spectrum from both the bremsstrahlung and the recombination can be described as [90-91]

$$I(E, T_e) \propto n_e^2 T_e^{-1/2} Z_{eff} e^{-E/T_e}, \tag{4.29}$$

where E is the X ray energy, n_e is the electron density, T_e is the electron temperature and Z_{eff} is the effective ion charge. It is clearly that the contribution to the total SXR flux is dominated by radiation from regions of highest electron density and temperature. Therefore, SXR measurements are localized towards the center of the chord along the field of view of the detectors.

Figure 4.19 shows the SXR imaging system in STOR-M [112-113]. The system

is equipped with two arrays of 13 detectors. Each detector array consists of both surface barrier diodes (SBD) and channel electron multipliers (CEM). The SBD's (EG&G ORTEC MODEL BA-17-50-100) measure the total energy of the radiation photons. The circuit diagram for the SBD current to voltage ($I - V$) converter is shown in Figure 4.20.

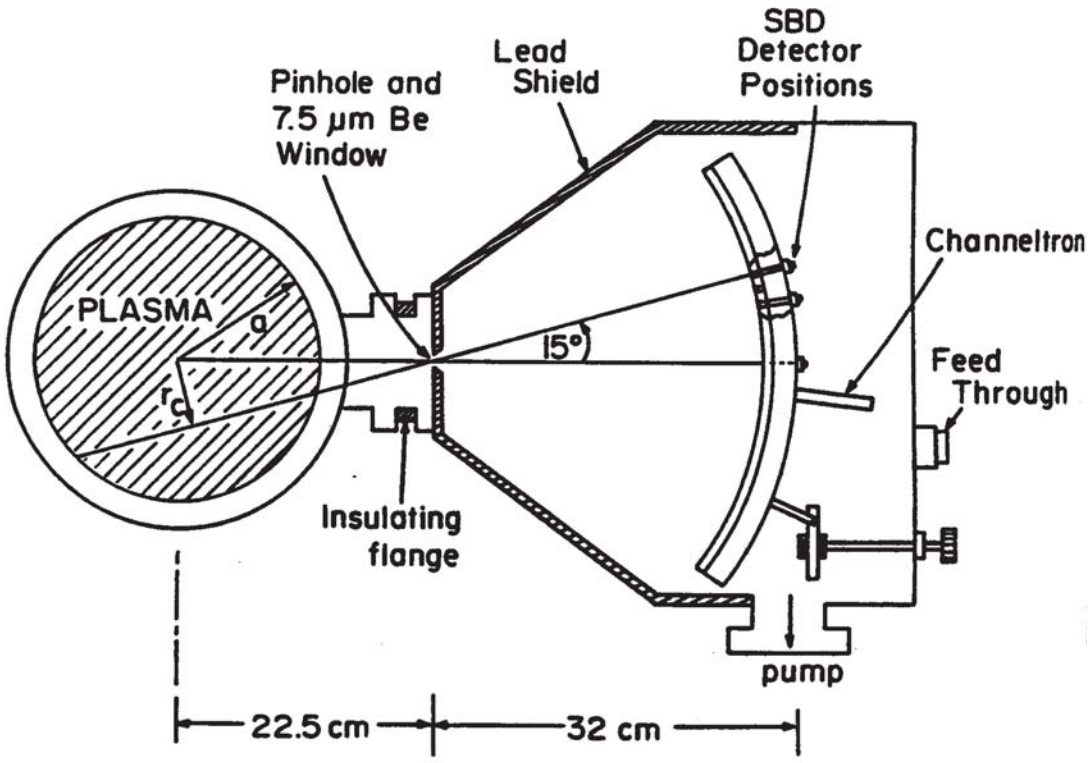

Figure 4.19: Schematic diagram of soft X-ray camera in STOR-M.

Since the current from the SBD is very small, a low noise, high input impedance operational amplifier is utilized as an $I - V$ converter. The output of the signal was further amplified with a simple voltage amplifier. The final signal after amplification is given by

$$V(t) = RAB \int \gamma(E) I(E, T_e) dE, \tag{4.30}$$

where $V(t)$ is in volts, R is the transimpedance of the $I - V$ converter and amplifier chain, A is the area of the detector exposed to the X rays, B is the detection efficiency,

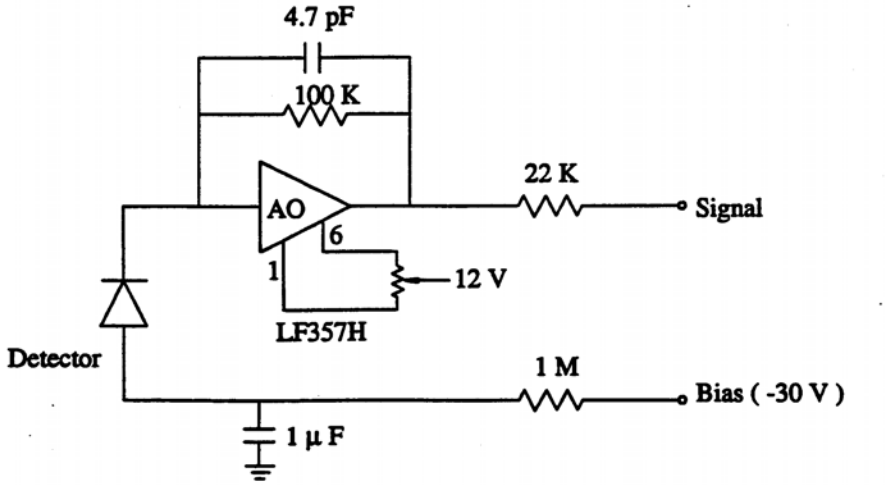

Figure 4.20: $I - V$ converter used for SBD detector

$\gamma(E)$ is the response function of the window and the detector chain given by

$$\gamma(E) = \prod_{i=2}^{5} e^{-\eta_i(E)\rho_i d_i}[1 - e^{-\eta_1(E)\rho_1 d_1}], \tag{4.31}$$

where ρ denotes the mass density, d is the foil thickness and η is the mass attenuation coefficient. The subscript 1 corresponds to the depletion layers, while the subscripts 2 to 5 correspond to the Be foil, Al contact, Au contact, and the dead layer, respectively.

The power for the $I - V$ converter and SBD bias is provided by a DC power supply. Care must be taken to avoid ground loops which can cause noise pick-up from the environment.

The system is mounted on the outside equatorial plane of the STOR-M vacuum chamber at toroidal $\phi = 135°$. The plasma SXR emissions are imaged on the detector array through a 1 cm diameter aperture with a 7.5 μm light tight beryllium foil used as the detector window. The foil isolates the detector housing chamber from the main tokamak chamber. Since most of the X-rays are emitted from the region of plasma which has the highest density and temperature, the signal from each detector represents emission from a region along the line of sight closet to the plasma center. The spatial resolution of the system is 2 cm which is determined by the geometry.

The SXR chamber is pumped down to about 2×10^{-6} torr by a 50 l/s turbomolecular pump backed with a conventional rotary pump.

The electron temperature can be deduced from the soft X-ray emission measurement through the absorbing foil technique. It is worthwhile to note that the interpretation of the SXR data on a small tokamak (such as STOR-M) is difficult since the expected central electron temperature is only about 200-300 eV, which is below the cutoff energy of the foil (For example, a Be foil with 7.5 μm thick has a cutoff energy of about 0.4 keV [90]). Large uncertainty in T_e may be produced in the electron temperature measurement and an independent method (e.g. Thomson scattering) is desirable to confirm the temperature.

(5) **Spectrometer**

Spectroscopy is widely used in tokamak plasmas to monitor line emissions from impurity elements and hydrogen. This measurement give a qualitative indication of the purity and the confinement properties of the plasma. Line broadening effects of the impurities is also utilized to determine the flow velocity of the bulk plasma, both toroidally and poloidal. Oxygen and Carbon lines are often used for impurity studies in tokamaks, since this elements outgas from the material on the inner surface of the vacuum chamber. The H_α radiation indicates the recycling process of the plasma particles at the edge region. Low level H_α radiation at the edge is an indication of batter plasma confinement.

In STOR-M, line emission in the visible range is monitored with a 0.35 m focal length single-pass Czerny-Turner grating monochromator (Heath EU-700) [118] with a relative aperture of f/6.8 and resolution of 1 Å in UV-VIS region. The grating has 1180 lines/mm and is blazed at 2500 Å. A fiber optic probe was used to transmit the radiation from the plasma to the entrance slit of the spectrometer. The optical probe is made of bundles of glass fibers with optical lenses at each end. The optical probe is routinely mounted on a horizontal port in the mid-plane of STOR-M to monitor the H_α line, which is viewed from the center chord. The experimental set-up for the monochromator is shown in Figure 4.21. The entrance and exit slits have a width of 10 μm and a hight of 3 mm. The dispersed light is detected using a photomultiplier

(RCA IP-28), which is shield from the magnetic field with μ-metal and enclosed in a brass and copper housing.

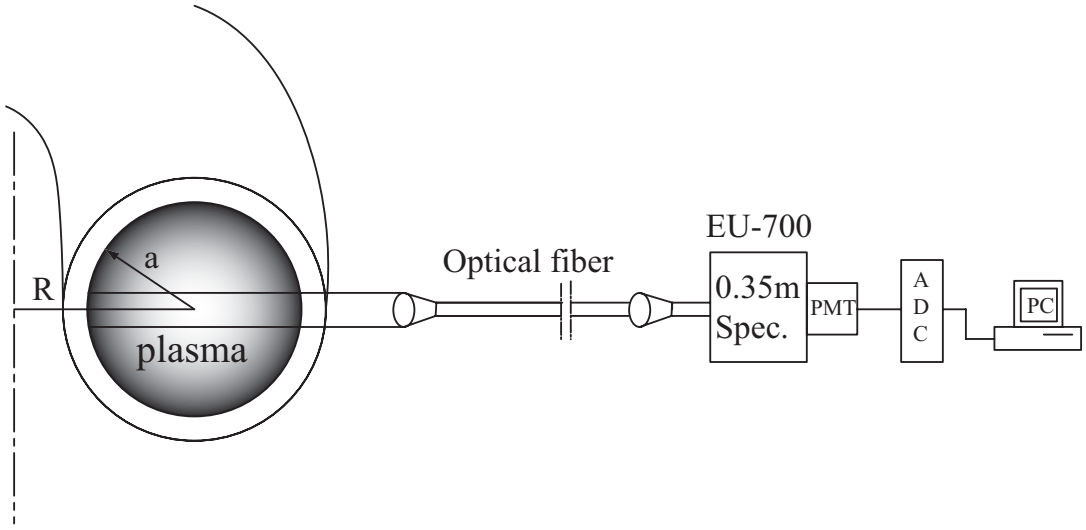

Figure 4.21: Monochromator set-up for H_α measurement in STOR-M.

4.4 USCTI Operation and performance

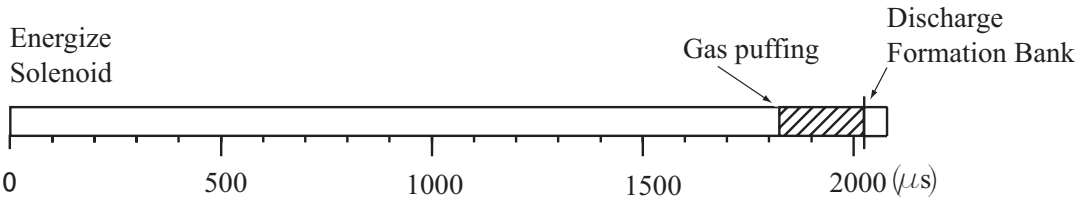

Figure 4.22: Time line of events in a typical USCTI discharge

In CT injection experiments, the STOR-M discharge is routinely operated in automatic mode. The discharges run shot by shot with a typical operation interval of 5 minutes. The charging cycle of both STOR-M and USCTI starts at the beginning of each operation cycle followed by the discharge cycle and the cooling cycle. The start point of the operation cycle defines the time $t = 0$ for both systems. The time sequence used in USCTI operation is shown in Figure 4.22. Formation is started by energizing the solenoid at $t = 0$, followed by gas puffing between 1830 μs and 2030 μs later. The formation bank discharge is initiated at $t = 2030$ μs.

Table 4.6: Operation parameters for a typical USCTI discharge

Parameters	Value
Formation bank voltage (V_{form})	18 kV
Acceleration bank voltage (V_{acc})	12 kV
Solenoid bank voltage	340 V, $\Psi_{bias} = 1.14$ mWb
Gas puffing bank voltage	950 V
Discharge time delay	3 μs
Bank charging cycle	168 s

Table 4.6 shows the operation parameters in a typical USCTI discharge. The time delay between formation and acceleration bank discharge can be adjusted between 0 and 8 μs.

The typical waveforms in a USCTI discharge are shown in Figure 4.23. The threshold of λ, $\lambda_c = 100\,\mathrm{m}^{-1}$ in the USCTI configuration ($\delta_{gap} = 0.032$ m). $\lambda \approx 153\,\mathrm{m}^{-1}$ which is determined by the formation current (peak) 140 kA and the bias flux $\Psi_{bias} = 1.15$ mWb. Therefore, $\lambda > \lambda_c$ is satisfied in USCTI discharges. CT velocity dependence on the acceleration voltage V_{acc} was studied. The formation bank voltage V_{form} was fixed at 18 kV during the scan of V_{acc}. Figure 4.24 shows that the maximum CT velocity is about $300\,\mathrm{kms}^{-1}$ at $V_{acc} = 16$ kV. Beyond this voltage, the CT magnetic fields were damaged and the "blow-by" effect occurred.

4.5 Summary

In this Chapter the STOR-M tokamak, the USCTI injector, and the major diagnostic tools for both CT plasma and STOR-M plasma are described. The injection system was constructed originally for tangential injection experiments. The injector consists of formation, compression and acceleration sections in a coaxial configuration. After formation, the CT relaxes to a stable minimum energy state through self-organization. In the acceleration region, the Lorentz force $\mathbf{J} \times \mathbf{B}$ accelerates the

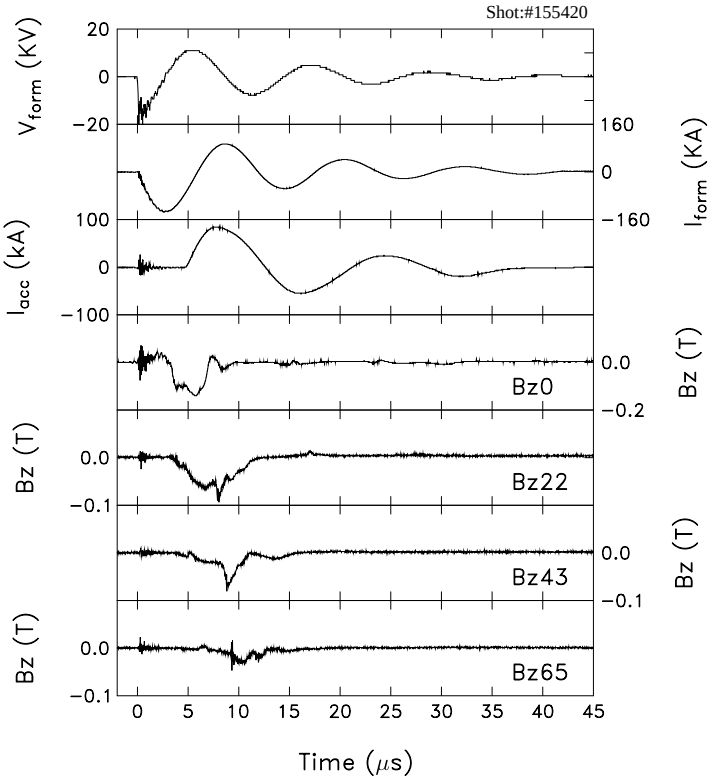

Figure 4.23: Typical USCTI discharge waveforms at $V_{form} = 18$ kV and $V_{acc} = 14$ kV. From top: Formation bank voltage (V_{form}); Formation bank current (I_{from}): Acceleration bank current (I_{acc}); Magnetic probe signal along several axial locations, Bz0, Bz22, Bz43, and Bz65.

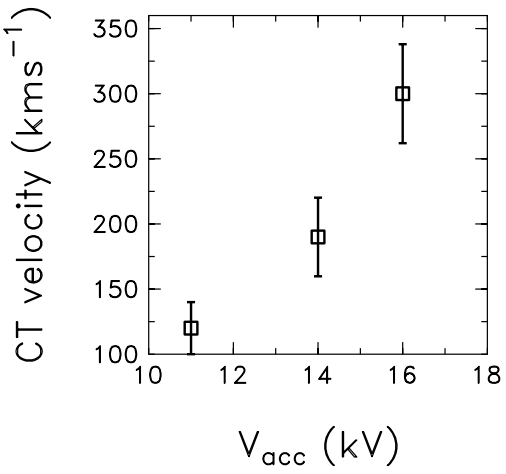

Figure 4.24: CT velocity vs. Acceleration bank voltage. The CT velocity (at P3) is evaluated by the time of flight method using two magnetic signals at the P2 and P3 locations.

CT to a high speed. The typical CT velocity and density are 150 kms^{-1} and (1-4)$\times 10^{21}\,\mathrm{m}^{-3}$, respectively. The CT velocity can reach its maximum, $\sim 300\,\mathrm{kms}^{-1}$, at higher acceleration voltage $V_{acc} = 16$ kV.

Chapter 5

Development of the CT deflector for vertical injection

The original USCTI was constructed for tangential CT injection. For vertical injection, a CT deflector has been developed. Essentially, it is a 90° flux conserving bend. The bend is attached to the exit of the acceleration section of USCTI. The CT is expected to follow the bend and change the injection direction from horizontal to vertical. This Chapter describes the modification of USCTI for the vertical injection. The detailed bench test results of CT translation in the curved tube are presented.

5.1 Introduction

The original USCTI as described in Chapter 4 was constructed for tangential CT injection experiments. The exit of the USCTI acceleration section was connected to a horizontal port through a bellows. To perform vertical injection, the straightforward way is to arrange the USCTI vertically by rotating the entire CT system by 90°. However, this idea was ruled out due to space limitation. An alternative is to bend the CT trajectory by 90°. For this purpose, a segment of 90° flux conserving bend has been developed. In the timescale of CT passing the bend (μs), the bend will act as a flux conserver and the image current in the wall provides the force to redirect CT translation direction. A conceptual illustration of CT deflection by the bend is shown in Figure 5.1. Once a CT is formed, its radial expansion is restricted by the image current flowing in the conducting walls of both the acceleration section and the linear drift tube. In addition, the gun produced CT is robust and can be

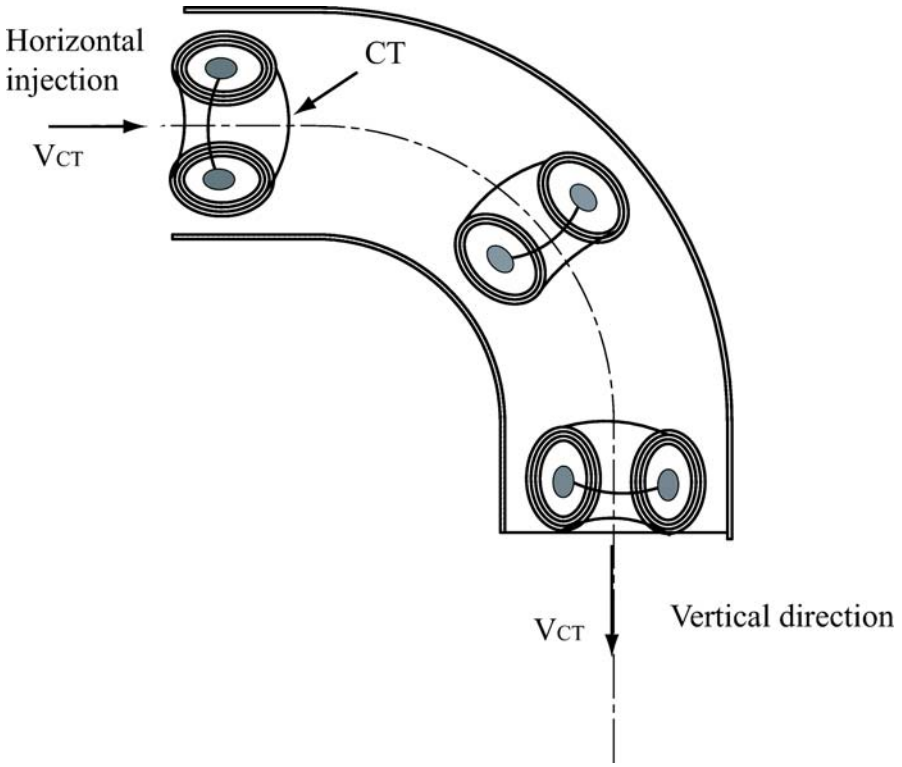

Figure 5.1: Conceptual illustration of CT deflection by a 90° flux conserving bend.

accelerated to a high velocity by the Lorentz force. These two factors may make CT deflection feasible. Therefore, testing of CT translation in a 90° bend is the first objective in this Chapter. Recent experimental investigation by Fukumoto *et al.* [53] has verified this conjecture. In their experiments, the CT produced by the HIT-CTI injector smoothly passed a segment of 45° and 90° stainless steel curved drift tube respectively (average curvature = 190 mm), with a velocity of $\sim 40\,\mathrm{kms}^{-1}$. The behavior of the CT in the curved tube was similar to that in a straight tube. The CT kept its integrity and magnetic field topology after the curved translation.

5.2 Deflector design

The deflector consists of a 90° segment of flux conserving curved tube (radius = 5 cm, average curvature radius = 164 mm), a compressor and a set of UHV vacuum

components. The main design parameter is the magnetic field diffusion time. The material in the curved tube is stainless steel with 3 mm wall thickness. The field diffusion time is estimated to be,

$$\tau \approx \frac{\delta R \mu_0}{2\eta} \approx 135\,\mu s, \tag{5.1}$$

where $\delta = 3$ mm is the wall thickness, $R = 5$ cm is the radius, η is the resistivity of the material ($7 \times 10^{-7}\,\Omega \cdot$ m for stainless steel), and $\mu_0 = 4\pi \times 10^{-7}$ H/m is the vacuum permeability. This value is much longer than the estimated CT transit time ($\leq 10\,\mu$s, based on the typical CT velocities $\sim 150\,\mathrm{kms}^{-1}$). The estimated lifetime of the CT is about $20\,\mu$s. In addition, a compressor (5 cm in radius at the entrance and 3 cm at exit) was used to match the vertical port of STOR-M for vertical injection.

Three small ports (9.5 mm in radius with 12 cm radial extension) are arranged axially along the curved tube to mount magnetic probes for diagnostic purposes. The diagram of the CT deflector is shown in Figure 5.2.

Another option for bending the CT trajectory is to extend the CT acceleration section in a curved geometry. It is expected that further CT acceleration can be achieved and higher CT velocity can be obtained after the CT passes the curved acceleration section. This can be done by an additional inner electrode which is coaxial with the 90° drift tube. Therefore, the 90° drift tube will become an outer electrode. The entire deflector is an extension of the original USCTI acceleration section as shown in Figure 5.3. The radius of the inner electrode is 18 mm to match that in the original USCTI.

5.3 Diagnostics and data acquisition

5.3.1 Magnetic probe array

To investigate CT motion in the 90° bend and the effects of the bend on CTs, two extra diagnostic tools, a magnetic probe array and a 12 channel spectrometer, were constructed to measure the CT magnetic field profile and CT optical emission (H_α,

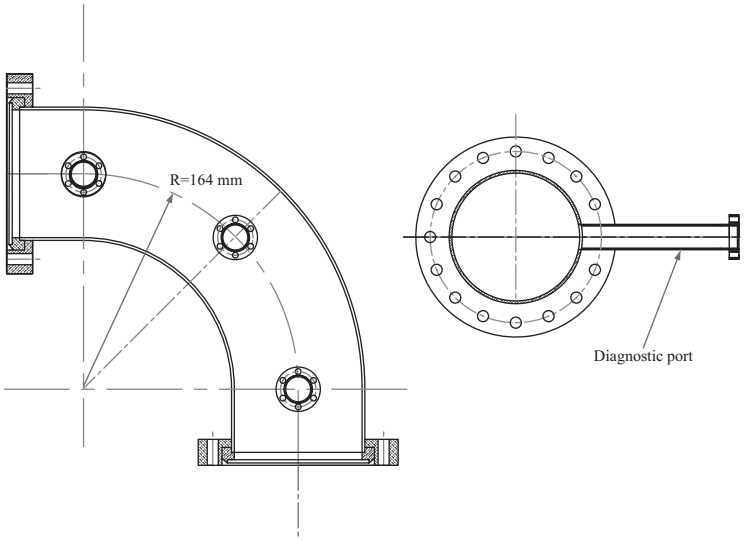

Figure 5.2: Schematic diagram of a 90° bend as a CT deflector. Three small diagnostic ports are 45° axially apart, designed for CT magnetic field measurement. The averaged curvature of the bend is 164 mm and the material is type 304 stainless steel with a 3 mm wall thickness.

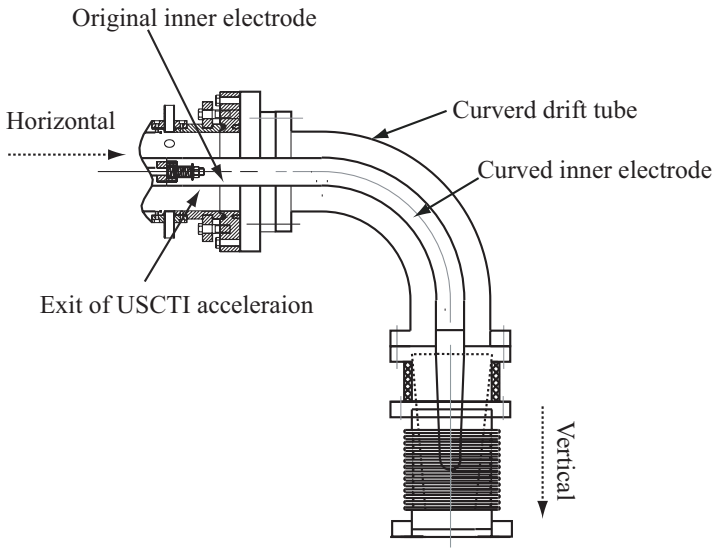

Figure 5.3: Schematic diagram of a 90° bend extending USCTI acceleration for CT deflection. The 90° inner electrode ($r = 17.8$ mm) is coaxial with the bend.

$\lambda = 657.6$ nm). In addition, a triple Langmuir probe was employed to measure CT plasma density and temperature.

The basic principle of magnetic field measurement by pick-up coils is well-known. Design considerations and applications were well described in a large amount of papers [98-109]. The magnetic probe array consists of a set of 4 pairs of miniature pick-up coils evenly spaced in a linear form 10 mm apart. The probe is mounted on the diagnostic port in the bend. There is one pair of pick-up coils at each location to measure both B_Z and B_ϕ of CT magnetic fields. AWG#34 copper wire (dia.= 0.16 mm) is used for winding the coils. All coils are wound on the form with 15 turns in each coil. The inductance of each pick-up coil is $L_{coil} \approx 0.8\,\mu$H. The fastest frequency response time of the coils is $L_{coil}/50 \approx 0.016\,\mu$s, where 50 is the characteristic impedance of the coaxial cable. At each location, two sets of holes are drilled in the form for winding the coil. The cross-section of each coil is 3 mm $\times$ 5 mm. The coils and the form are sealed in a 5 cm long ceramic tube (diameter = 6.4 mm) and Torrseal is used for vacuum tightness. A passive integrator is used to recover the magnetic field signal. In the probe design, the turn-area nA (sensitivity) of the coil should be large enough to make suitable probe output. nA is given by

$$nA = \frac{V_{coil}}{dB/dt} = \frac{V_{coil}}{\omega B_{max}}, \tag{5.2}$$

where V_{coil} is the coil output, $\omega = 2\pi f$ is angular frequency and B_{max} is the peak value of CT magnetic field. In USCTI, the frequency range of CT magnetic fields 0.1 MHz $\leq f \leq$ 1 MHz is assumed and $B_{max} = 0.2$ T. After integration, output of the probe is

$$V_{mp} = \frac{nA}{RC} B = 5B, \tag{5.3}$$

where V_{mp} is the probe output in volts, B is the magnetic field to be detected in Teslas, and $RC = 50\,\mu$s is the time constant of the integrator. The standard calibration technique was used to calibrate each probe along with 20m of coaxial cable. The calibration results are shown in Figure 5.4. Each probe has a flat frequency response up to 1 MHz which is sufficient high for CT magnetic field measurement. In Figure 5.4, the measured nA is about $250\,\text{mm}^2$. According to Eq. (5.3), a B of

0.2 T, which is the typical CT magnetic field in USCTI, will produce 1 volt probe output V_{mp}. This is suitable in the experiments. Figure 5.5 shows the probe data acquisition circuit.

5.3.2 Multi-channel spectrometer

A multi-channel spectrometer with a 300 mm focal length is used to monitor H_α emission of CT. The system consists of a SpectraPro 300i imaging spectrometer (Acton Research Corporation), a PIMAX 1024×256 Gen. II intensified CCD (ICCD) camera, an ST133 Controller (Princeton Instruments), a DG535 Timing Generator (Stanford Research Systems, Inc.), and a computer with Winspec data acquisition software. The diagram of the system is shown in Figure 5.6. A home-made collimator, made of a plane convex quartz lens of focal length 5 cm and diameter 1.3 cm, collects the nearly parallel light entering the collimator and focuses the light onto one end of a quartz optical fiber which guides the light to the entrance port of the spectrometer. The entrance slit width is 25 μm. The grating has 600 line/mm and blazed at 3000Å. The ICCD camera records the dispersed spectrum at the focal plane of the exit slit. After each shot, the image is read out to the controller, where it is digitized and transferred via a high-speed data link to a computer for post processing.

5.3.3 Data acquisition

The CT magnetic signals are digitized by two oscilloscopes with sampling frequency of 100 MHz (Lecroy 9314M, 4 channels) and 50 MHz (TDS 2014, 4 channels) respectively. The peak value of the signal is registered as the CT magnetic field strength. The CT velocity is determined by the time of flight method.

In CT field profile measurements, both oscilloscopes are used for digitizing the magnetic signals at the exit of the bend (4 channels for B_Z and 4 channels for B_ϕ) in each shot.

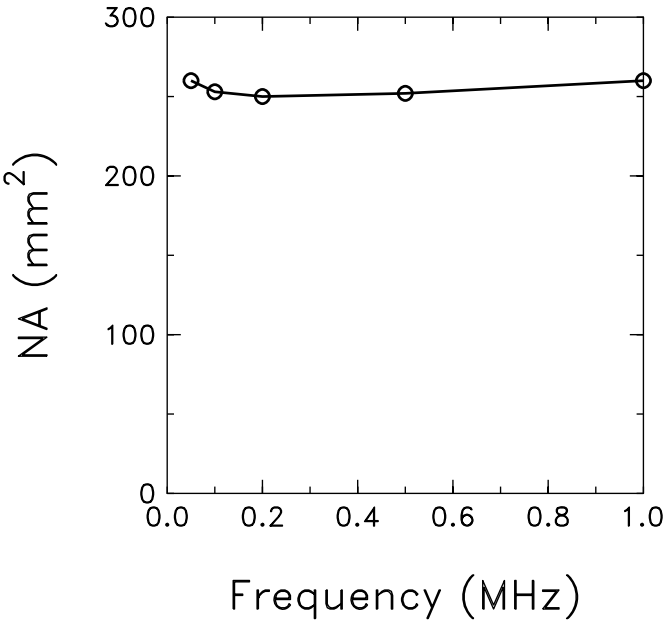

Figure 5.4: Turn-area (nA) vs. Frequency.

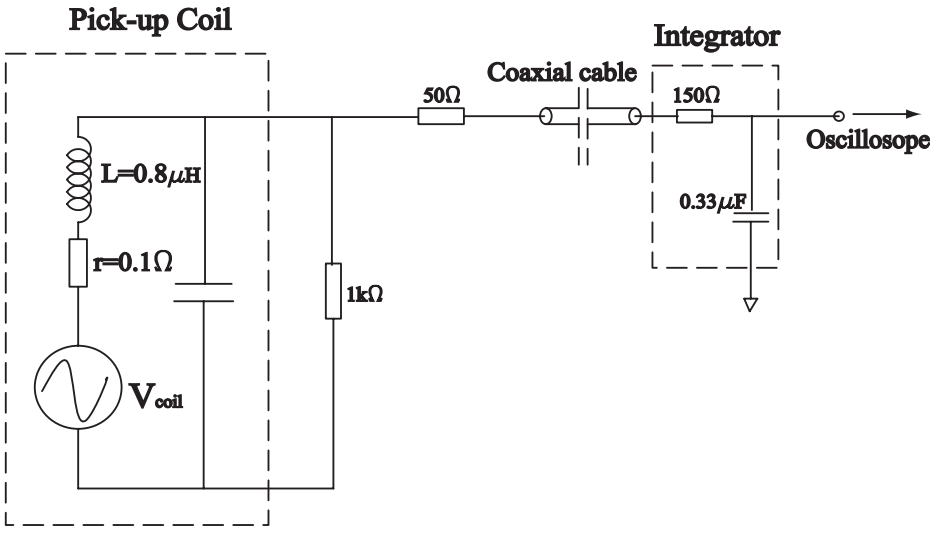

Figure 5.5: Circuit for magnetic probe data acquisition in USCTI.

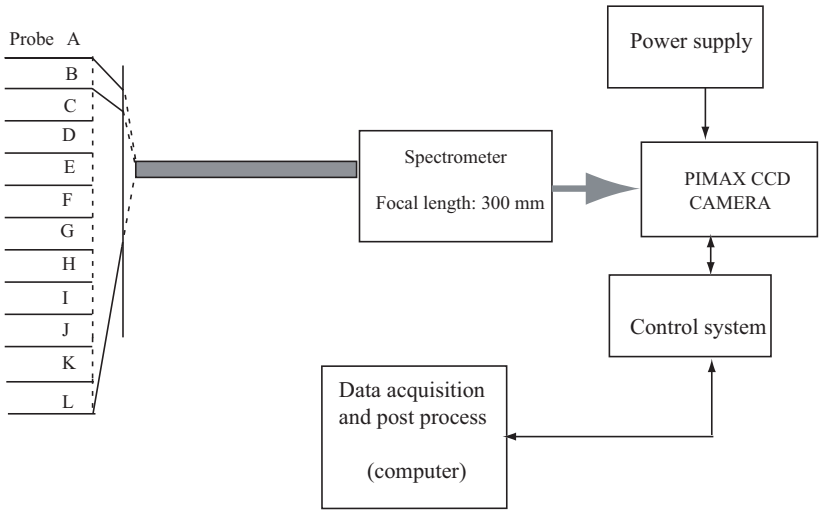

Figure 5.6: Block diagram of 12 channel spectrometer set-up.

5.4 Bench test of the 90° bend as the drift tube

5.4.1 Experimental set-up

Figure 5.7 shows the experimental set-up for the bench test. In the diagram, P0 to P7 indicate the locations for the magnetic probes, L1 for a Langmuir probe. At the P6 location, a probe array was inserted radially in the bend. Each pair of coils is at radial locations 12, 22, 32, 42 mm, respectively. This probe array was used to measure the radial profile of the CT magnetic field at the exit of the bend. Other magnetic probes were used to measure the CT magnetic fields at the outer electrode wall at several axial locations along the CT trajectory. CT velocity is evaluated by time of flight method. For example, CT velocity at the P6 location can be determined by $\overline{\text{P5P6}}/\Delta t$, where $\overline{\text{P5P6}}$ is the distance between P5, P6 and Δt is the time lag between the peak of magnetic signals at locations P5 and P6. This method is valid when CT acceleration is weak. A triple Langmuir probe was used to measure CT density and temperature. The Langmuir probe was inserted into the straight tube (radius = 32 mm) at the P7 location. A magnetic probe was mounted in the port opposite to the Langmuir probe. Therefore, at P7, the CT

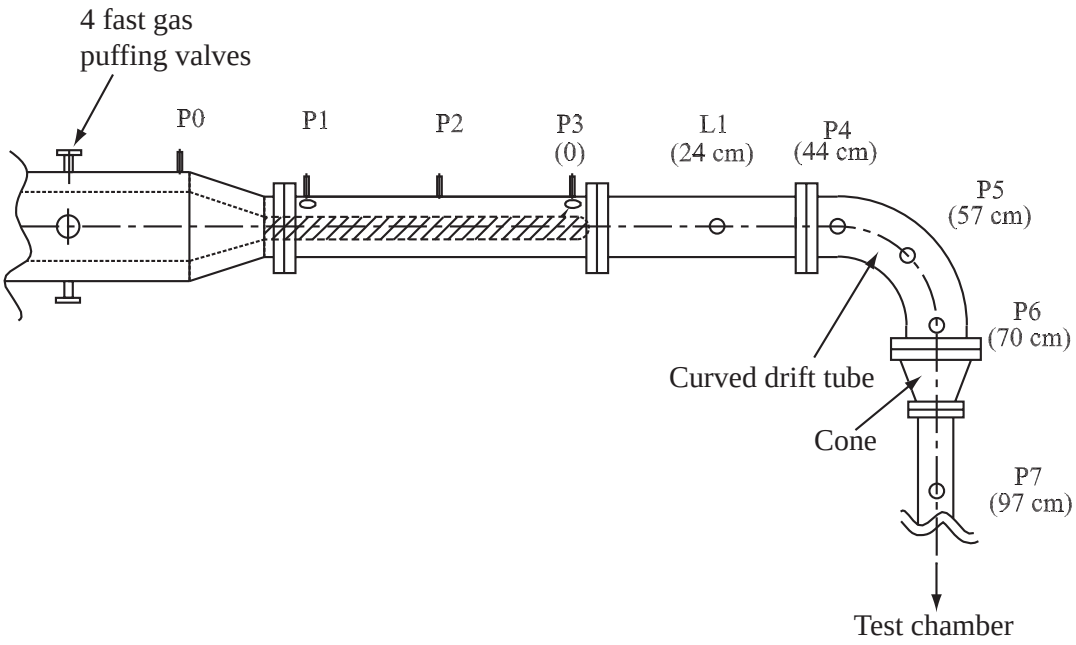

Figure 5.7: Schematic diagram of USCTI with curved drift tube and diagnostic port locations.

magnetic field, density and temperature can be detected at the same time for each discharge. A multi-channel optical spectrometer was used to simultaneously monitor the H_α radiation at several locations along the CT trajectory. The inner acceleration electrode ends near the P3 probe. The numbers attached to L1 and P4 $\sim$ P7 are the axial distances with respect to P3. A straight drift tube was added to ensure that the distance from P3 to P7 (97 cm) is close to the distance from P3 to the STOR-M tokamak center in the actual vertical injection experiment (114 cm). In bench tests, the voltages of the CT formation and acceleration banks were 18 kV and 14 kV, respectively. The solenoid typically induced a bias magnetic flux of 1.4 mWb.

5.4.2 Results and discussion

(1) **Temporal evolution of CT magnetic field along CT trajectory**

An accelerated CT undergoes a decay process when it travels in a linear drift tube. Both magnetic field and density of CT will decrease along its trajectory. The decay of the CT magnetic field is characterized by the decay time τ_{decay}. An

important issue of the bench tests is to study the effects of the bend on CT decay. CT poloidal magnetic fields were measured at locations P3 $\sim$ P7, where P3 is near the exit of acceleration section, P4, P5, P6 are in the bend and P7 is downstream of the compressor. In the early experiments, CT suffered from a fast decay in magnetic field in the curved drift tube. In Figure 5.8, magnetic signals of 20 consecutive shots at the discharge conditions V_{form} = 18 kV and V_{acc} = 14 kV were collected for statistical analysis. In the curved tube (P4 to P6, 26 cm in length), the field strength decreased from 80% to 25%, while in the straight tube (P3 to P4, 24 cm in length) the strength decreased about 20%. The fast decay of CT magnetic field is mainly due to impurities in the CT. In addition, the impurities in the CT lead to the low reproducibility of the discharges which results in a large error bar of the data in the early experiments.

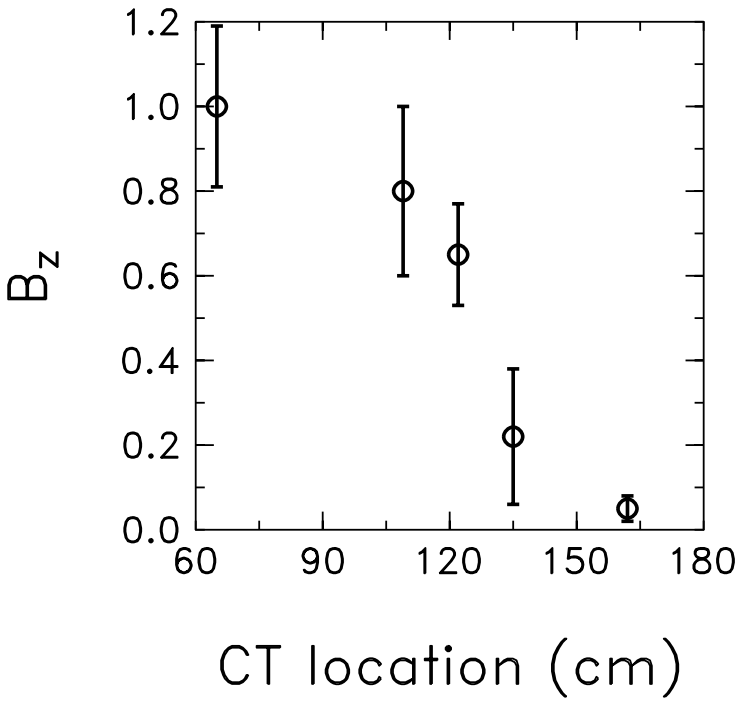

Figure 5.8: B_z vs. CT location. The CT poloidal magnetic field B_z is normalized by $Bz65$ at P3 location - the exit of the acceleration. The formation and acceleration bank voltages were V_{form} = 18 kV and $V_{\rm acc}$ = 14 kV.

CT parameters were significantly improved after the optimization of the USCTI

discharge and considerable electrode cleaning shots. Figure 5.9 shows the improved CT magnetic fields in the curved tube. The vertical scale for the last trace has been magnified by a factor of ten. The acceleration bank voltage was $V_{acc} = 14$ kV. Data indicate that the CT velocity before the compressor in the bending drift tube is approximately constant at $\sim 130\,\mathrm{kms}^{-1}$. The estimated velocity between the P6 and P7 positions is $\sim 30\,\mathrm{kms}^{-1}$. This shot shows that the magnetic field strength does not change significantly in the 90° bend. Significant decay of magnetic field occurred in the compressor. During the time span ($10\,\mu$s) for the CT to travel through the compressor from P6 to P7, the magnetic field strength decreases to about one-tenth of its value just before the compressor. This decay is somewhat faster than the estimated lifetime of 5 μs based on the averaged compressor radius $r = 4$ cm.

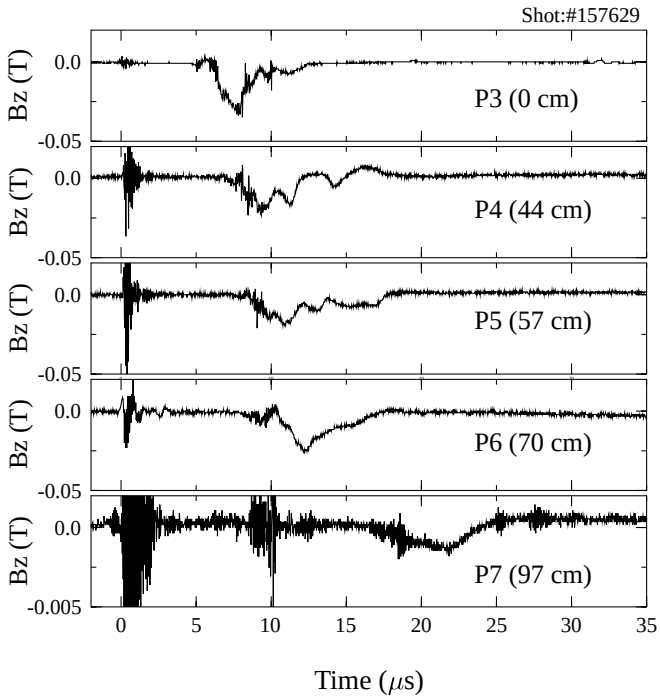

Figure 5.9: Poloidal CT magnetic field measured at locations 0, 44, 57, 70 and 97 cm away from the CT inner acceleration electrode. The acceleration bank voltage was $V_{\mathrm{acc}} = 14$ kV, from D. Liu *et al.* [120].

Figure 5.10 shows the CT velocity evolution along its trajectory. The acceleration bank voltage is 14 kV. CT velocity at each location P_i, $(i = 1 \sim 7)$ was estimated by $\overline{\mathrm{P}_{i-1}\mathrm{P}_i}/\Delta t$. The data presents the statistic results for 20 consecutive shots. It was

found that the curved drift tube did not significantly slow the CT velocity down. The measured CT velocity at P3 is about 230 kms^{-1} and 130 kms^{-1} at P6 location. An acceptable CT velocity has been obtained after the CT exits the curved drift tube, $V_{CT} \sim 130\,\text{kms}^{-1}$. Significant CT deceleration occurred after the CT passes the compressor: CT velocity decreases to 40 kms^{-1}. This is presumably caused by the retarding force due to the compression of the CT passing through the compressor.

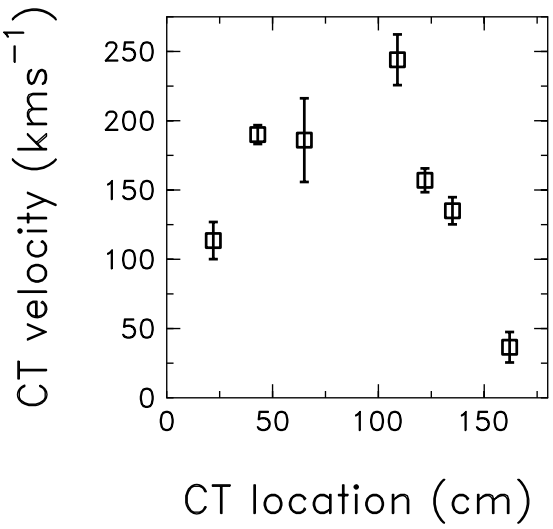

Figure 5.10: CT velocity vs. location. The acceleration bank voltage was $V_{acc} = 14$ kV.

(2) **CT magnetic field profile measurement**

CT field profile measurements during CT translation in the curved tube have been done by Fukumoto *et al.* [53]. This measurement is important to study the effects of the bend on the CT magnetic field structures. It was found that the CT field structure maintained a typical Bessel function shape at CT velocity $\sim 40\,\text{kms}^{-1}$. Our measurements have extended this study to a higher CT velocity of $130\,\text{kms}^{-1}$. At the P6 location, field profiles of CTs have been measured by a magnetic probe array at several radial locations: r =12, 22, 32, 42 mm respectively. Figure 5.11 shows both the CT toroidal (B_ϕ) and poloidal (B_z) field profiles. The measured profiles agree well with theory. The CT toroidal magnetic field does not change direction

across the minor radius but the CT poloidal magnetic field changes direction. The measured CT magnetic axis is about $0.55R_{fc}$ which is smaller than the theoretical value ($0.63R_{fc}$) for a CT in the force-free state. This is primarily because of a centrifugal force acting on the CT during its translation in the curved tube. This force pushes the CT radially inwards. The experimental results indicate that CT configuration remains intact in the curved drift tube.

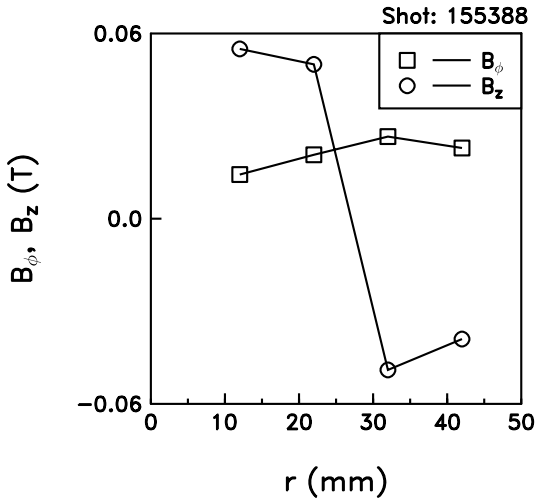

Figure 5.11: Radial profile of toroidal and poloidal magnetic fields of a traveling CT at the exit of the 90° bend; r is the distance from the center of curved drift tube, from D. Liu *et al*. [120].

(3) H_α **emission measurement**

Monitoring CT optical emission along its trajectory can offer us the information about the CT decay process directly. In this measurement, a series of images of the CT plasma were obtained by a multi-channel spectrometer. Five optical probes were mounted at P0, P1, P3, P4, and P7 locations respectively. In Figure 5.12 the highest intensity is found at $\lambda = 657.6$ nm which is H_α emission. Other spots correspond to impurity radiation. The H_α emission at P7 has been detected although the intensity is weak compared with that at the P1 location (the very beginning of acceleration region), as shown in Figure 5.12. This suggests that the CT can follow the curved tube and pass through the compressor.

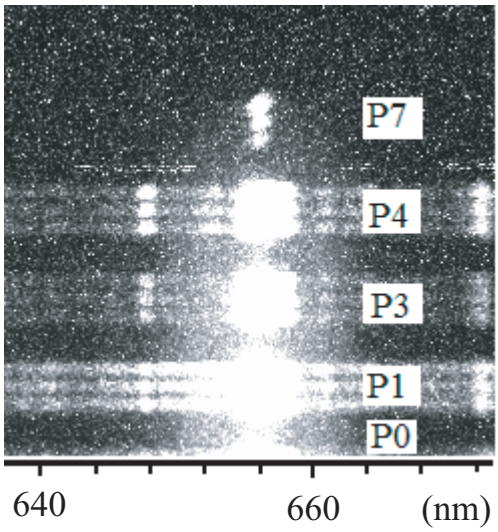

Figure 5.12: Images of H_α emission along CT trajectory. P0 is in the CT formation region, P1 and P3 are in the acceleration region, P4 is at the entrance of the 90° curved tube and P7 is 10 cm after the compressor.

(4) **CT density and temperature measurement**

At location P7, the CT density and temperature measured by a Langmuir probe are $(0.6 \sim 1) \times 10^{21}\,\mathrm{m}^{-3}$ and 10 eV, respectively. Figure 5.13 shows the temporal evolution of the CT density. The density at P7 is about half of that in the P3 location as measured by a He-Ne interferometer in tangential injection [37-38]. The longer CT traveling distance causes much decay of CT, which attributes to the density decrease.

5.5 Bench test with 90° bend for acceleration

5.5.1 Experimental set-up

In this experiment, a new curved inner electrode (made of Oxygen Free Electronic (OFE) copper) was added as an extension of the original one. The inner acceleration electrode extended into a newly designed compressor with a more gentle transition

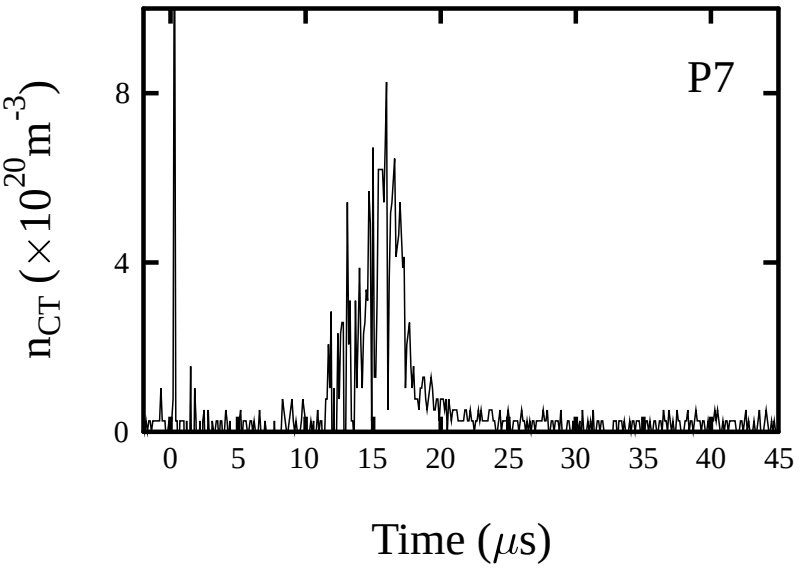

Figure 5.13: CT density at the P7 location measured by a triple Langmuir probe, discharge condition: $V_{acc} = 14$ kV.

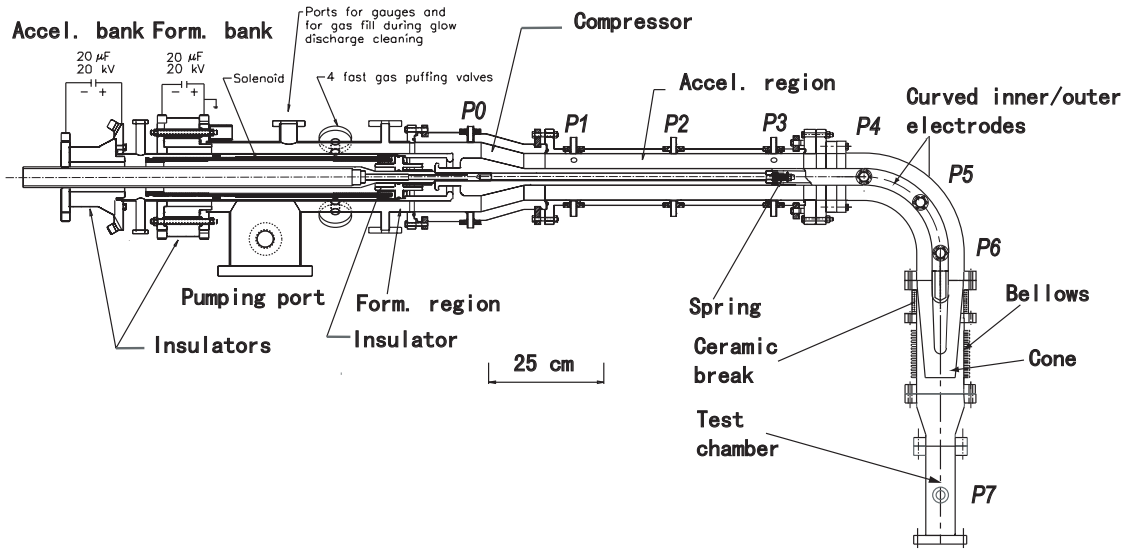

Figure 5.14: Experimental set-up of the modified USCTI with inner/outer curved electrodes. P0 $\sim$ P7 are diagnostic ports for mounting magnetic probes. A small test chamber was attached at the end.

part. The total length of the CT acceleration section was increased from 60 cm to 114 cm. The objective was to further increase the CT velocity in the curved acceleration section. The surface of the curved inner electrode was coated with chromium to minimize impurity content during CT translation. Figure 5.14 shows the set-up for the bench test of CT translation in the curved tube with an curved inner electrode.

5.5.2 Results and discussion

(1) **Typical discharge waveforms**

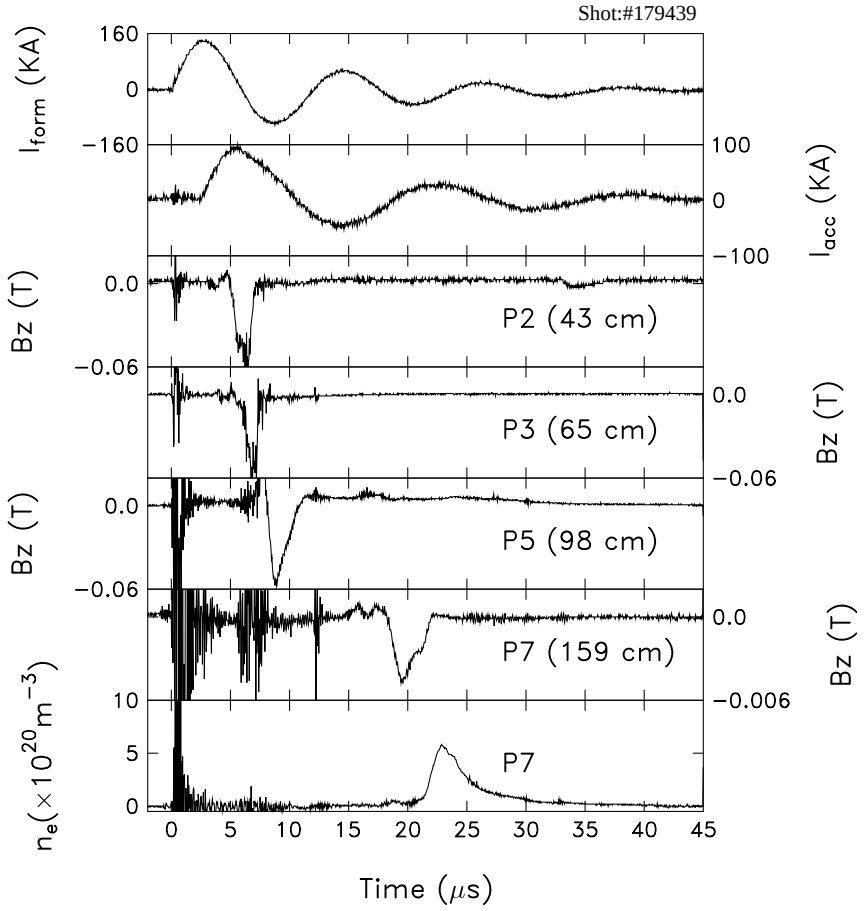

Figure 5.15: Typical waveforms for the modified USCTI discharge with the curved inner and outer electrodes, $V_{acc} = 16$ kV.

Typical waveforms of the bench test are shown in Figure 5.15, from top: CT

formation current, CT acceleration current, poloidal magnetic field at the P2, P3, P5, and P7 locations respectively, and CT density at the P7 location measured with a triple Langmuir probe. The vertical scale for the sixth trace has been magnified by a factor of ten. CT velocity is about 54 kms^{-1} at the P7 location. FWHM of the magnetic signals is narrower compared with those in Figure 5.9. This is because the high acceleration voltages applied produce larger acceleration magnetic fields to push the CT forward.

(2) H_α **emission along CT trajectory**

The H_α emission measurement along the CT trajectory has been carried out as shown in Figure 5.16. The emission was monitored at CT formation, CT acceleration, the bend, and the small test chamber. In Figure 5.16, an enhancement compared with that in Figure 5.11 in the H_α emission of CT plasmas at the P7 location was observed which implies less decay during the CT translation.

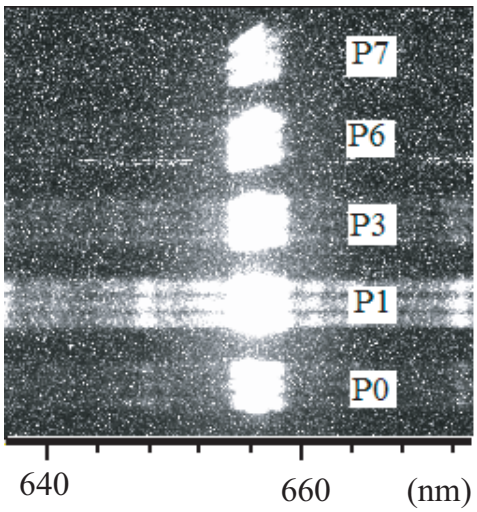

Figure 5.16: H_α emission at the P0, P1, P3, P6, P7 locations, where P0 is in the formation region, P1 and P3 are in the acceleration region, P6 is in the curved tube, and P7 is in the small test chamber.

(3) **Temporal evolution of CT traveling**

Based on the magnetic probe signals, the CT locations during its translation can be depicted. Here we define the time corresponding the peak value of the magnetic

signal as the time of CT passing the location. Figure 5.17 shows the temporal evolution of CT locations in terms of time with different acceleration bank voltage. The data markers represent the P0 (0 cm), P1 (22 cm), P2 (43 cm), P3 (65 cm), P5 (98 cm) and P6 (111 cm) locations. The dashed line shows the results based on one-dimensional point model (V_{acc} = 16 kV). At V_{acc} = 14 kV, a CT velocity $\sim$ 180 kms^{-1} after passing curved tube has been achieved. With the increase in acceleration bank voltages to 16 kV, the CT velocity increased to 270 kms^{-1}. The reason for the improvement in CT velocity is due to the further acceleration of CT in the curved acceleration.

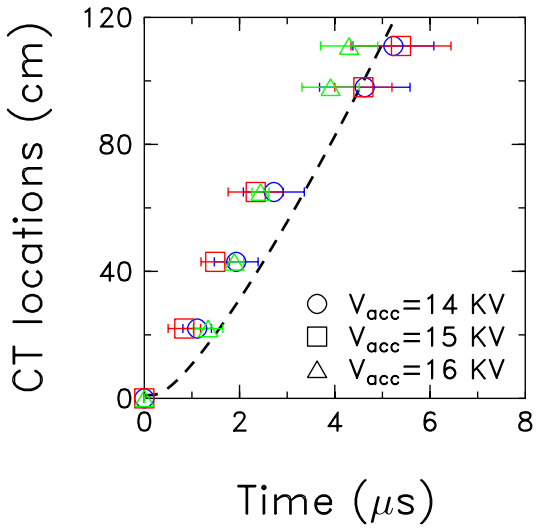

Figure 5.17: CT locations vs. Time at different acceleration bank voltages; the dashed line represents simulation results based on a one-dimensional point model.

(4) **Effects of the bend on CT magnetic field**

The magnetic signals in the curved acceleration section demonstrate a different patten at different acceleration voltages V_{acc}. The full width at half magnitude (FWHM) of the magnetic signal decreases with increasing V_{acc}, as shown in Figure 5.18. The reason for the decrease in FWHM of the magnetic signals is that larger accelerating magnetic fields B_{acc} act on the CT due to the higher acceleration cur-

rents. At fixed V_{acc}, the FWHM values of the CT magnetic signals increase along CT translation. However, this change evolves in different ways at $V_{acc} = 16$ kV and $V_{acc} = 14$ kV. At $V_{acc} = 14$ kV, the FWHM values of the magnetic signals peak at the P5 location (4.5 μs), while at $V_{acc} = 16$ kV the FWHM values keep increasing from 1.5 μs (P3) to 2.5 μs (P6).

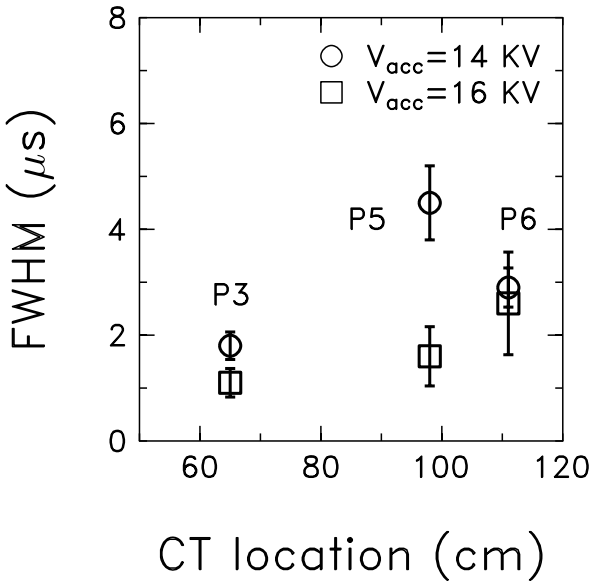

Figure 5.18: FWHM of the CT magnetic signals at V_{acc}=14 kV and 16 kV.

In addition, amplification of the magnetic signals in the curved acceleration section has been observed. In Figure 5.19, the magnetic signal at the P6 location was 50% larger than that in location P3. This phenomenon was also observed in the earlier CT compression experiments [31-33]. When CT is accelerated in a conical coaxial electrode configuration, the field amplification occurs. In our experiment, the acceleration configuration is in uniformly shaped; the cause of field amplification is presumably because of the curvature of the bend. From a macroscopic point of view, the CT will undergo two forces, one due to the $\mathbf{J} \times \mathbf{B}$ accelerating force, the other is a centrifugal force due to the curved motion of the CT during curved acceleration. It is suggested that this centrifugal force compressed the CT to give rise to field amplification.

Field amplification was not observed in the previous bench test in which only the curved drift tube was attached (see Figure 5.9 where the magnetic signal at P6 was smaller than at P3). Although the injected CT can translate in the curved drift tube, the CT velocity may not be high enough so the field amplification would not occur, since the centrifugal force $F_c \propto V_{CT}^2$. The observations suggest that further acceleration of CT has been achieved in the curved CT acceleration region.

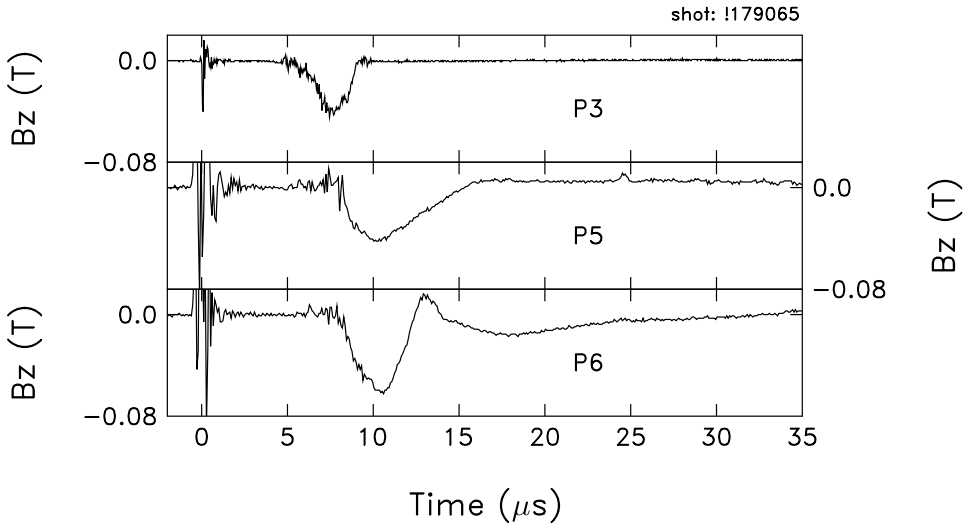

Figure 5.19: CT magnetic field signals along the 90° curved acceleration region at $V_{acc} = 16$ kV, showing field amplification.

Figure 5.20(a) and (b) illustrate the effects of curved acceleration electrodes on the decay of the CT magnetic field at different V_{acc}. The markers in the figure represent the P1, P2, P3, P5, and P6 locations respectively. In the straight CT acceleration region, fast CT decay was observed. The CT decay time τ_{decay} is about 5 μs at $V_{acc} = 14$ kV and 2.3 μs at $V_{acc} = 16$ kV. In the curved acceleration region, field decay of the CT is mitigated by field amplification through increased τ_{decay} at the P5 location and an increase in the magnitude of the CT magnetic field at location P6.

(5) **Effects of the compressor on CT parameters**

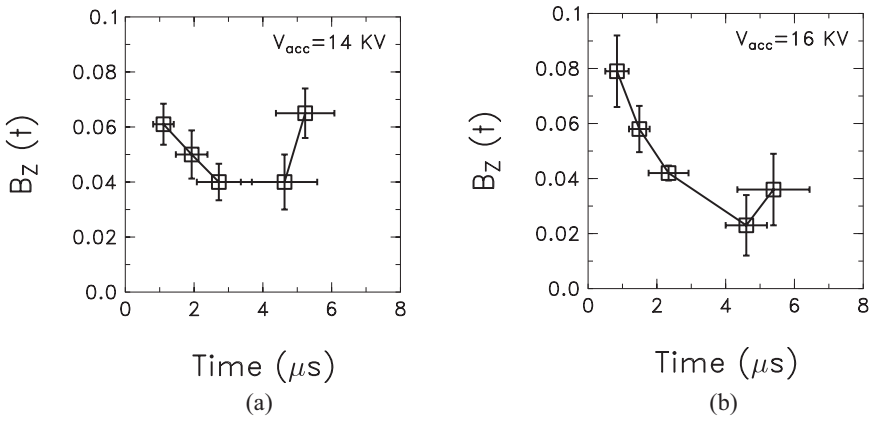

Figure 5.20: Temporal evolution of CT magnetic field signals at (a) V_{acc}=14 kV and (b) V_{acc}=16 kV.

After the CT passes through the curved acceleration region, it will further undergo a segment of conical coaxial electrodes with 18 cm length. This transition section is made to match the smaller vertical port of the STOR-M vacuum chamber. In the bench test, the key parameters are CT velocity and density, which infer the kinetic energy of CT. CT density is measured by the standard triple probe technique and CT velocity is evaluated by the time of flight method. Significant deceleration of the CT was observed after CT passing the compressor. The typical CT parameters at the P7 location (157 cm) are $60 \sim 100\,\mathrm{kms}^{-1}$ in velocity and $(0.6 \sim 1) \times 10^{21}\,\mathrm{m}^{-3}$ in density.

The Ψ_{bias} was scanned with fixed $V_{acc} = 16$ kV. Figure 5.21 (a) shows that density of the CT has a weak dependence on Ψ_{bias}. The CT velocity increased slightly as Ψ_{bias} increased, as shown in Figure 5.21(b).

5.6 Conclusion

The original USCTI has been modified to allow vertical injection. The modifications include attaching a 90° curved drift tube to the exit of the USCTI acceleration section. In this configuration, the injected CT was expected to be able to pass through the curved tube and change its injection direction form horizontal to vertical.

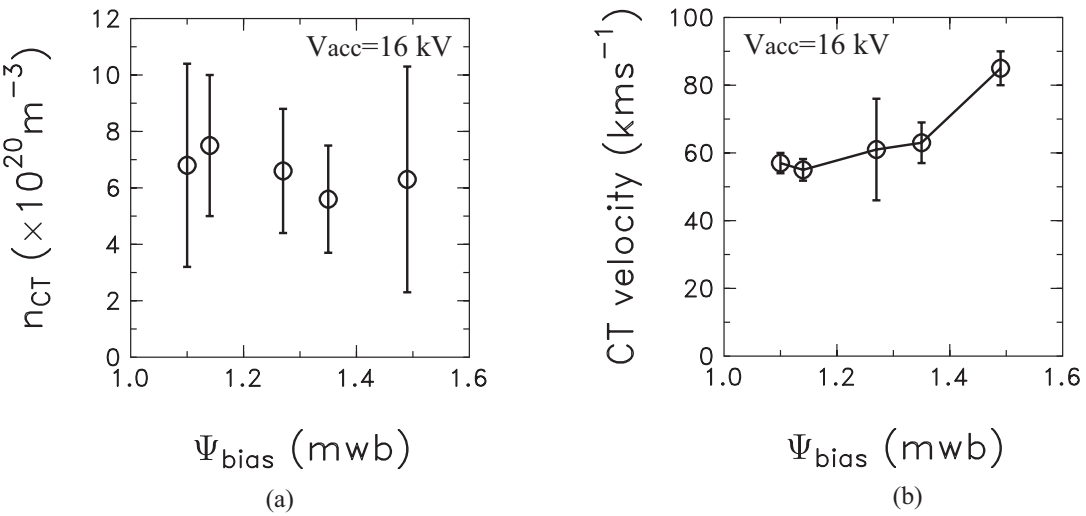

Figure 5.21: (a) CT density vs. Ψ_{bias}, (b) CT velocity vs. Ψ_{bias}, discharge condition: V_{acc}=16 kV.

The bench test results have confirmed this point. To optimize the CT parameters in the curved drift tube, particularly the CT velocity, an additional inner electrode, which is coaxial with the curved drift tube, was further added to the original part. Such a modification extended the original USCTI acceleration section in a curved geometry. Bench test results have revealed that further acceleration of the CT has been achieved in the curved acceleration region.

Bench tests in both CT deflection configurations showed that the horizontally injected CT can be deflected to the vertical direction. The results provided the basis for the actual vertical injection into the STOR-M tokamak.

Chapter 6

Vertical CT injection into STOR-M

6.1 Introduction

The bench test results have confirmed that the CT trajectory can be bent by the 90° curved tube at velocities of $\sim 130\,\mathrm{kms}^{-1}$. The CT magnetic field structure was conserved during deflection. Based on the results, actual vertical CT injection experiments have been subsequently performed on the STOR-M tokamak for the first time [119-120]. The objective is to study the feasibility of tokamak fuelling by vertical injection of CTs and the interaction between injected CTs and STOR-M plasma. In this Chapter, experimental results of vertical injection are presented.

The following effects are always observed following vertical injection: (a) rapid increase in line-averaged density and (b) increase in soft X-ray (SXR) emission level (central chord). Another significant achievement was that disruption-free discharges were obtained for the first time with vertical CT injection.

Experimental results are presented as follows. The normal Ohmic discharge in STOR-M will be described in Section 6.2. In Section 6.3, the experimental set-up for vertical injection experiments will be described. Experimental observations in vertical injection and comparison with tangential injection are presented in Section 6.4.

6.2 Normal ohmic discharge in STOR-M

The sequence of an ohmic discharge involves initial gas breakdown, current ramp-up, steady phase, and discharge termination. The initial gas breakdown depends critically on the ratio of applied electric field to gas pressure, E/P. In STOR-M, this value is about $3.5 \times 10^4\,\mathrm{V \cdot m^{-1} Torr^{-1}}$ [100]. Seed electrons are accelerated by the induced electric field through the transformer. The avalanche process produces more electrons through collisional ionization of neutrals. Preionization is used routinely before initiation of the toroidal electric field to get quality discharges with good reproducibility and to save magnetic flux in the iron core transformer. The preionization is realized either by an rf field (4 MHz, 10 kW, 1 ms duration) or by thermionic filament emission.

In the quasisteady phase, the normal loop voltage is 3 V. However, such a low loop voltage (which is an indication of higher electron temperature) is reached only after a considerable number of conditioning discharges to clean the chamber wall. After 30 minutes of glow discharge (gas pressure 1.1×10^{-4} torr), about one hundred preconditioning discharges are needed before the tokamak is ready for data collection.

After the gas breakdown phase, the plasma current starts to rise due to the externally applied electric field and reaches its peak value in 10 ms. Figure 6.1 shows a set of STOR-M plasma discharge parameters during a normal Ohmic discharge, from the top: plasma current I_p, loop voltage V_l, line-averaged electron density $\bar{n}_e$, gas puffing pulses, plasma position ΔH, and H_α radiation at the plasma edge. These measurements were made with hydrogen gas at a filling pressure of 1.8×10^{-4} Torr and toroidal field strength of 0.65 Tesla. The sudden drop in the loop voltage marks the beginning of the current ramp-up phase. It is due to the sudden increase in plasma conductivity, caused by further ionization. The plasma position is controlled by an active feedback system. The fourth trace in Figure 6.1 shows the plasma position variation during this shot. The safety factor $q(a)$ decreases as the plasma current increases. The plasma is more susceptible to MHD instability at low q. The $q(a)$ value is about 4 during the steady phase of the discharge.

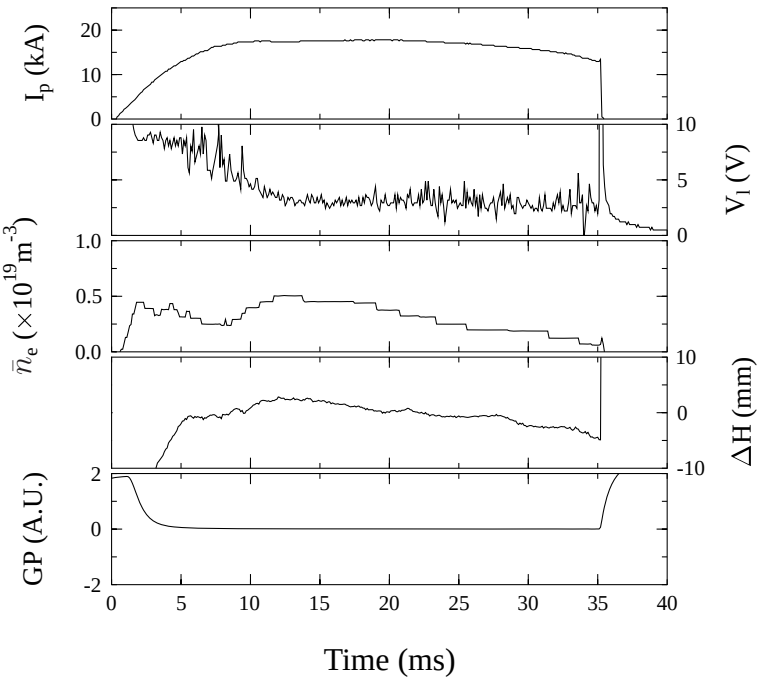

Figure 6.1: Normal Ohmic discharge waveforms in STOR-M.

The STOR-M discharge duration can last up to 200 ms, completely exhausting the available magnetic flux. However, the discharge is terminated usually at about 30-40 ms with strong gas puffing to avoid production of excessive run-away electrons at the end of the discharge. These energetic electrons could damage the limiter and the chamber wall.

The energy confinement time [10-11] during steady state of the discharge can be estimated as follows [112]:

$$\tau_E = \frac{W}{P_{OH}}, \tag{6.1}$$

where $W = \frac{3}{2}\bar{n}(\bar{T}_e + \bar{T}_i)V$, and $P_{OH} = I_p V_l$, V is the plasma volume. With $\bar{n} = 0.5 \times 10^{19}\mathrm{m}^{-3}$, and $\bar{T}_e$ =170 eV (evaluated from the neoclassical resistivity [10-11]), the energy confinement time during the steady state of the discharge is estimated as :

$$\tau_E \simeq 0.5\,\mathrm{ms}. \tag{6.2}$$

This is in reasonable agreement compared with the neoAlcator scaling law [122] given by $\tau_E = 7 \times 10^{-22} n_e R^2 a q(a)$, which gives 0.72 ms.

In the STOR-M discharge, the plasma behavior is monitored with the soft X-ray (SXR) camera (for the core plasma) and Mirnov coils (for edge plasma). Figure 6.2 shows the typical discharge with these diagnostics. Since the higher temperature and density is in the plasma center, the amplitude of the SXR radiation reaches its maximum at the central chord, as shown in the fifth trace in Figure 6.2. The Mirnov signals usually present such a pattern that higher oscillations accompany poor plasma confinement. A burst of rf noise can be seen in the Mirnov signals prior to the plasma current rise, indicating the preionization (see the last two traces in Figure 6.2).

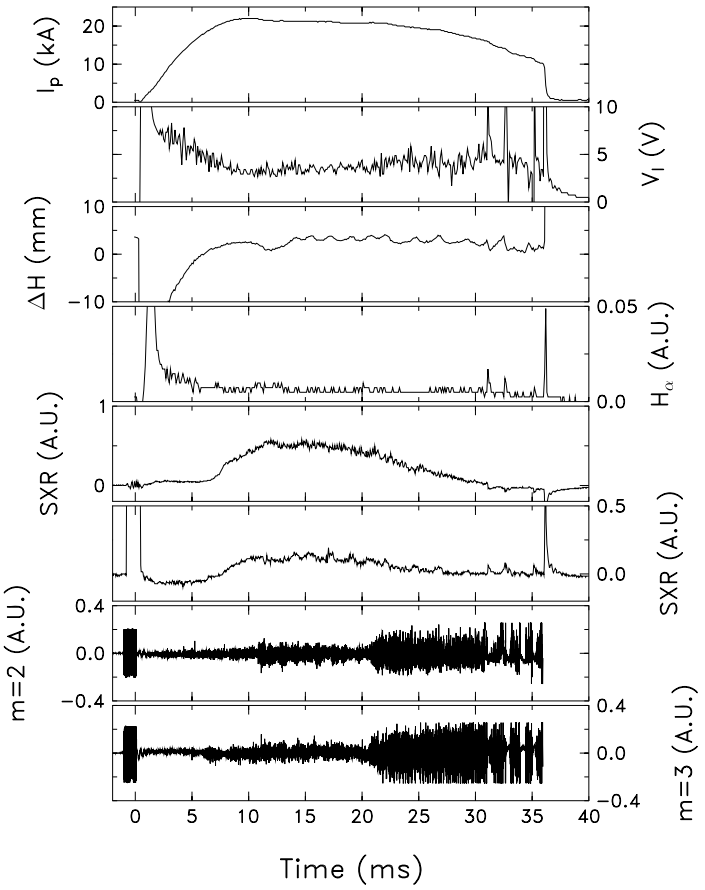

Figure 6.2: Normal STOR-M discharge, showing (from top) plasma current I_p, loop voltage V_l, plasma displacement ΔH, H_α emission, soft X-ray ($r = 0$ and 2 cm) and Mirnov coil measurements ($m = 2$ and 3).

6.3 Vertical injection set-up

The experimental set-up for vertical CT injection is shown in Figure 6.3. A vertical port with an oval cross-section (approximately 6.3 cm extended in the toroidal direction and 19 cm in the major radial direction) on top of STOR-M was used for vertical injection. The straight stainless steel tube with probe L1 in Figure 5.7 was replaced by a ceramic break (50 mm in axial length). In addition, a bellows was added between USCTI and STOR-M. These were used to isolate the ground and mechanical vibration of these two systems. A set of magnetic probes, Bz0 (corresponding to P3 in the bench test), Bz35, Bz48 and Bz82 were employed to monitor the CT poloidal magnetic field. The numerical numbers attached to Bz in the magnetic probe notations represent the linear distance from the Bz0 probe. The Bz82 probe was inserted from a port at the bottom of the tokamak. It could only be used to detect CT magnetic signals without tokamak discharges.

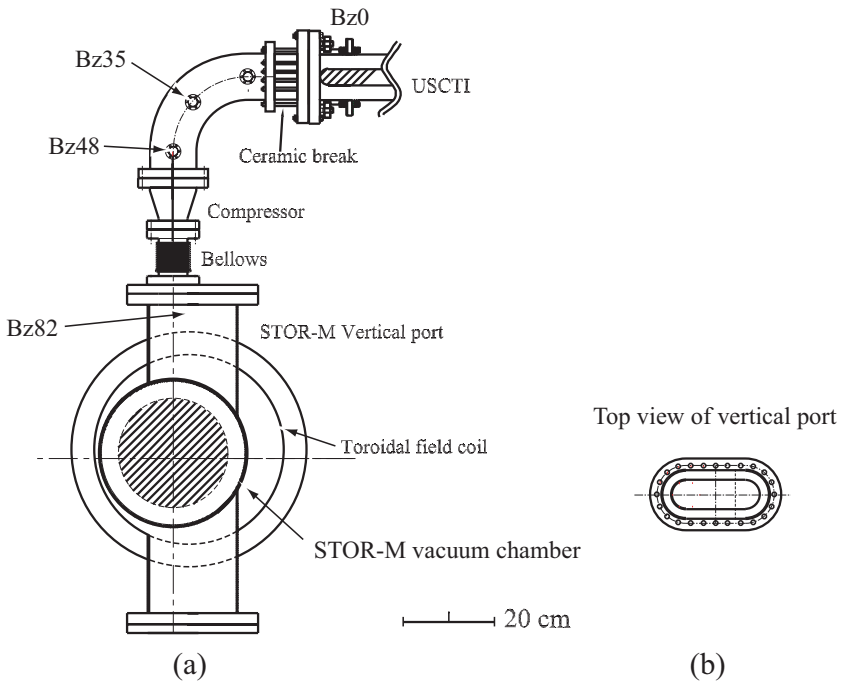

Figure 6.3: Experimental set-up for vertical CT injection into STOR-M. (a) Sideview of the interface between STOR-M and USCTI, and (b) Top view of the STOR-M vertical port for vertical injection.

In vertical injection, the toroidal magnetic field (B_t) of STOR-M was 0.7 T, plasma current (I_p) 20 kA and electron density ($\bar{n}_e$) in the range $(0.5 \sim 2) \times 10^{19}\,\mathrm{m}^{-3}$. The CT formation bank voltage was fixed at 18 kV and the voltage of the acceleration bank was scanned from 12 kV to 17 kV.

6.4 Results and discussion

6.4.1 Vertical CT injection into the toroidal field

Prior to the vertical CT injection into the tokamak discharge, the CT was injected into the vacuum tokamak toroidal magnetic field ($B_t = 0.7$ T) without plasma discharge. The objective was to study the interaction between the CT and the tokamak toroidal field. Figure 6.4 shows the typical CT poloidal magnetic field signals at various locations along the drift tube and in the tokamak port. The vertical scale for the last trace has been magnified by a factor of ten.

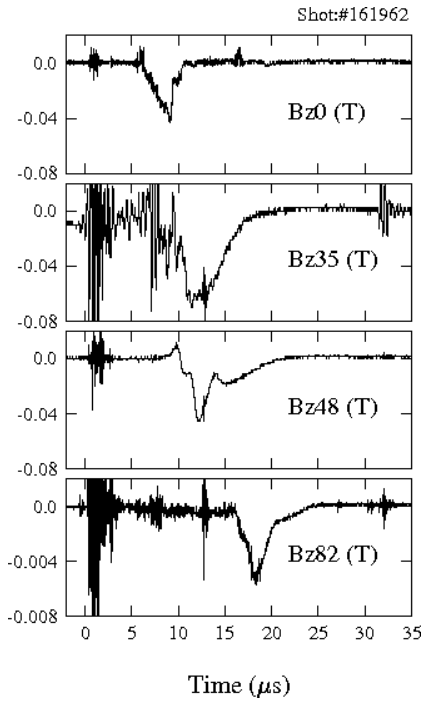

Figure 6.4: CT poloidal magnetic field along the 90° bend and after the compressor. Discharge conditions: tokamak toroidal magnetic field $B_t = 0.7$ T and $V_{acc} = 14$ kV.

In Figure 6.4, it has been found that the CT magnetic fields along the curved tube are almost the same, about 0.04 T. No decay of CT magnetic field was observed as the CT traveled along the curved drift tube. Significant decay of the CT magnetic field occurred in the compressor part. The CT poloidal magnetic field decreased to 0.006 T at the entrance of the vertical port (Bz82). CT velocity is estimated to be about 130 kms^{-1} in the curved tube. The final CT velocity has been calculated based on the time delay of the peaks of the magnetic signals at the Bz48 and Bz82 locations. For the CT discharge shown in Figure 6.4, the final velocity is $\sim 60\,\mathrm{kms}^{-1}$. It has been found that the final CT velocity increases almost linearly with acceleration bank voltage V_{acc} as shown in Figure 6.5.

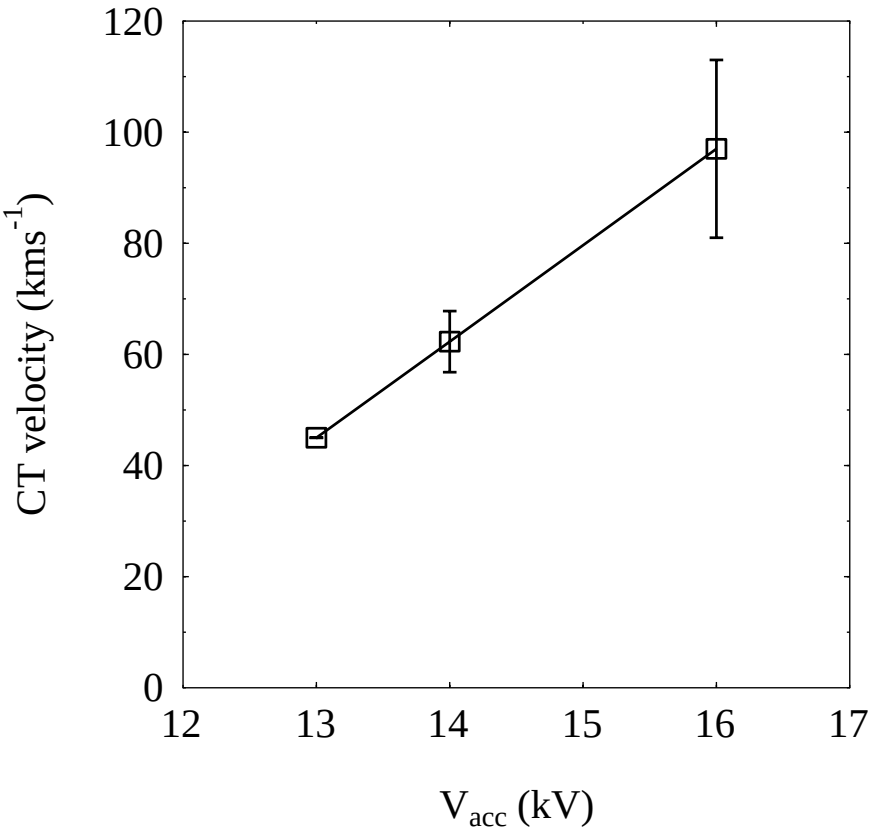

Figure 6.5: CT velocity vs. acceleration bank voltages. The vacuum tokamak toroidal magnetic field was $B_t = 0.7$ T.

At bank voltages lower than 13 kV, the CT poloidal magnetic signals could not be detected at the Bz82 locations, indicating that the initial CT velocity was too low to pass through the compressor. The minimum velocity for CTs to pass the compressor

is $\sim 160\,\mathrm{kms}^{-1}$ at the exit of the acceleration region (Bz0). At $V_{acc} = 16$ kV, the CT velocity reaches $\sim 100\,\mathrm{kms}^{-1}$ after passing the compressor. When the acceleration bank voltages are higher than 16 kV, no poloidal magnetic field signals from the CT can be detected at the exit of the acceleration region or along the 90° bend, as shown in Figure 6.6. The observations indicate that the CT was destroyed, presumably due to the "blow-by" CT discharge mode at high acceleration bank voltages [47, 52].

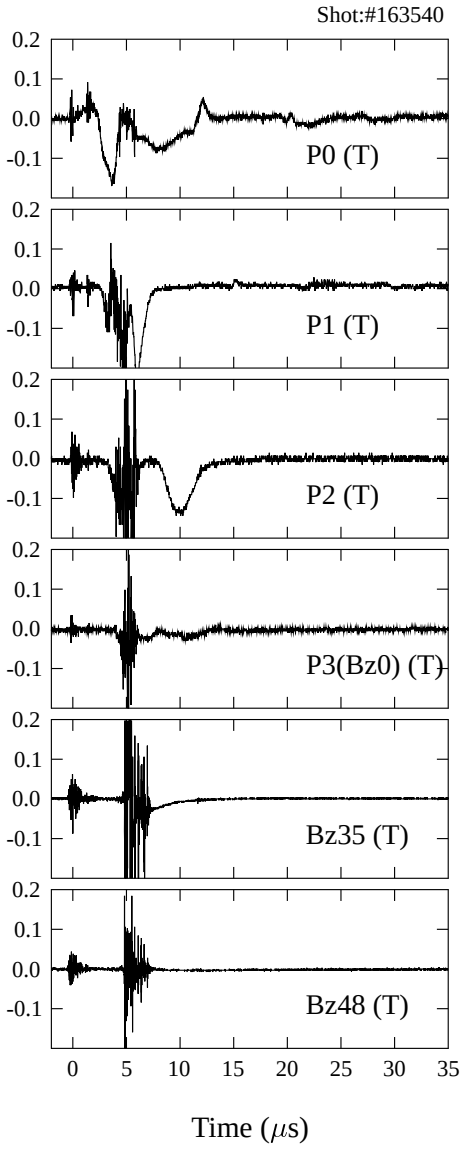

Figure 6.6: CT poloidal magnetic signals along the trajectory in vertical injection experiments at $V_{acc} = 17$ kV showing "blow-by" effect. Discharge conditions: $B_t = 0.7$ T.

It should be mentioned that the CT parameters have been improved compared

with the bench test experiments. The CT poloidal magnetic field (Figure 6.4) doubled compared with that in the bench test experiments (Figure 5.9). The possible explanations might be optimization of CT discharge parameters, conditioning of the electrode surfaces and also changes in the experimental set-ups. As a result, the final CT velocity increased from 30 kms^{-1} in the bench test to 60 kms^{-1} in the injection setup for the same acceleration bank voltage at V_{acc} =14 kV. Also, the minimum V_{acc} has been reduced to 13 kV to ensure that the CT can pass through the 90° bend and the compressor.

6.4.2 Typical discharge waveforms of vertical injection

Actual vertical CT injection experiments have been performed on the STOR-M tokamak. Typical parameters of the injected CT are: $(0.6 \sim 1) \times 10^{21}\,\mathrm{m}^{-3}$ in density, ~ 0.005 Tesla in magnetic field and $\sim 100\,\mathrm{kms}^{-1}$ in velocity. Figure 6.7 shows the temporal evolution of the tokamak parameters during a discharge with vertical CT injection at 14.2 ms. The CT acceleration bank voltage was 14 kV and the tokamak toroidal magnetic field was $B_t = 0.7$ T. The traces shown in Figure 6.7 are (from the top): plasma current (I_p), loop voltage (V_L), electron density ($\bar{n}_e$), plasma horizontal displacement (ΔH), H_α radiation level and floating potential (V_f). CT injection does not disrupt the tokamak discharge. The loop voltage (V_L), plasma horizontal displacement (ΔH), H_α radiation level, and floating potential (V_f) stay intact. The line averaged electron density increases abruptly, peaks at 400 μs after CT injection and then decreases again. In addition, compared with ht doubling of the line averaged electron density observed previously during the H-mode triggered by tangential CT injection [8, 37-38], the density increase following vertical CT injection is small, but clearly identifiable.

6.4.3 STOR-M fuelling by vertical injection

The vertical CT injection has been performed with different acceleration bank voltages V_{acc}. Higher V_{acc} leads to higher CT kinetic energy density, which will help CT

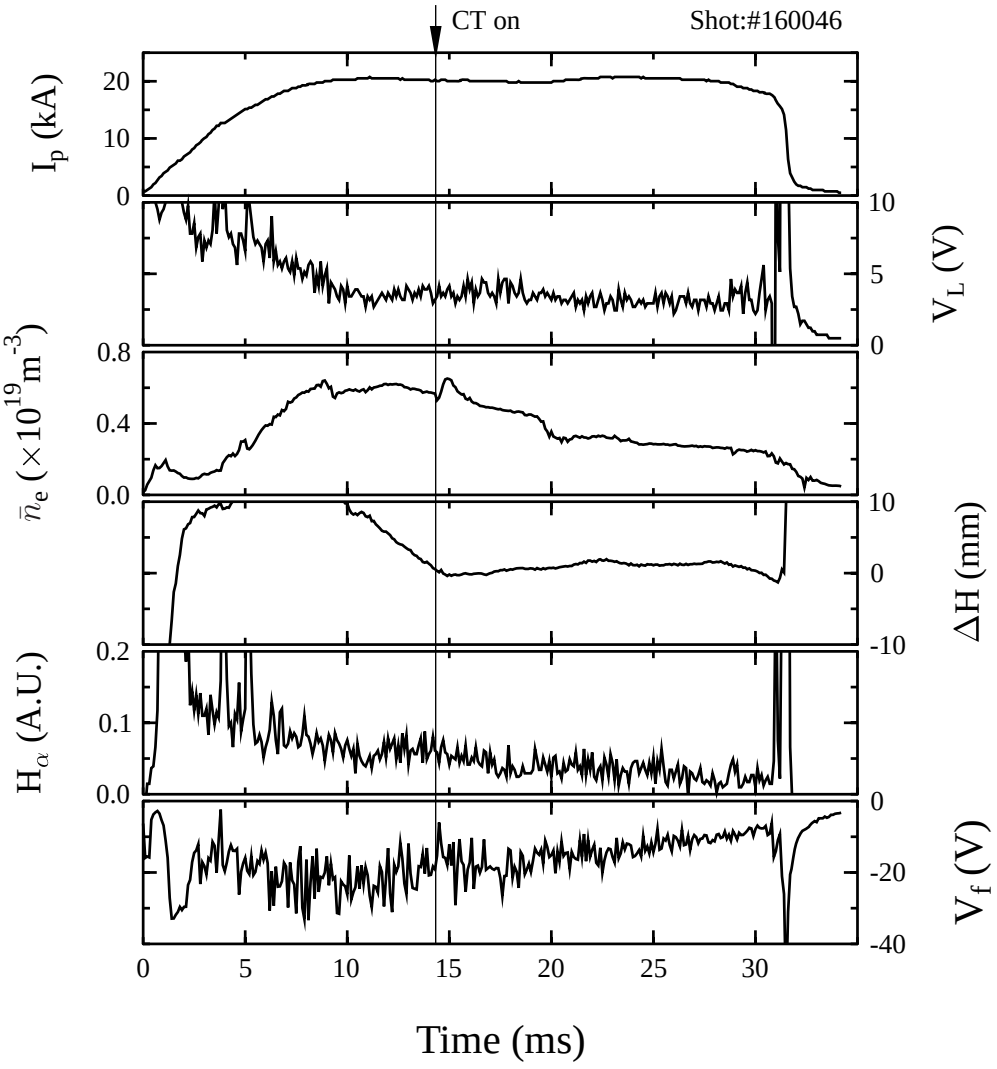

Figure 6.7: Time evolution of the STOR-M plasma parameters with vertical CT injection at 14.2 ms. From top: plasma current, loop voltage, line averaged density, horizontal displacement, and the floating potential at $r = 13.5$ cm in the scrape off layer.

penetration into the STOR-M toroidal magnetic field. Figure 6.8 shows STOR-M plasma fuelling by vertical CT injection at V_{acc} =16 kV. The density increases about 20% from $4.8 \times 10^{18}\,\mathrm{m}^{-3}$ to $5.8 \times 10^{18}\,\mathrm{m}^{-3}$ within 600 μs. This can be confirmed with the two fringe signals. There was a π phase shift in the fringe signals caused by vertical injection. In the 4 mm microwave interferometer for density measurement in STOR-M, 1 fringe phase shift corresponds to $2.3 \times 10^{18}\,\mathrm{m}^{-3}$ in density.

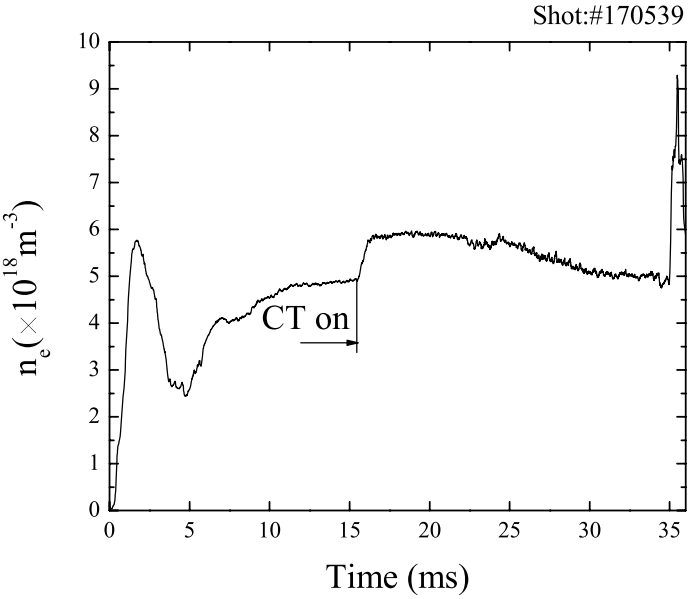

Figure 6.8: Temporal evolution of the line averaged density (center chord) during STOR-M discharge with vertical CT injection. Discharge condition: $B_t = 0.7$ T, $V_{form} = 18$ kV, $V_{acc} = 16$ kV.

The changes in electron density were studied with both vertical CT injection and CT gas puffing. Figure 6.9 illustrates the density evolution under these two conditions. The CT formation bank was discharged at $t = 13.1$ ms. In the case of vertical injection, the increase in electron density is immediate. However, there is a 5 ms time delay between the time of gas puffing and the starting time of density increase.

6.4.4 SXR measurement in vertical injection

Since CT penetration is determined by the balance between the CT kinetic energy and the toroidal magnetic pressure, a higher $V_{acc} = 16$ kV was applied to increase the

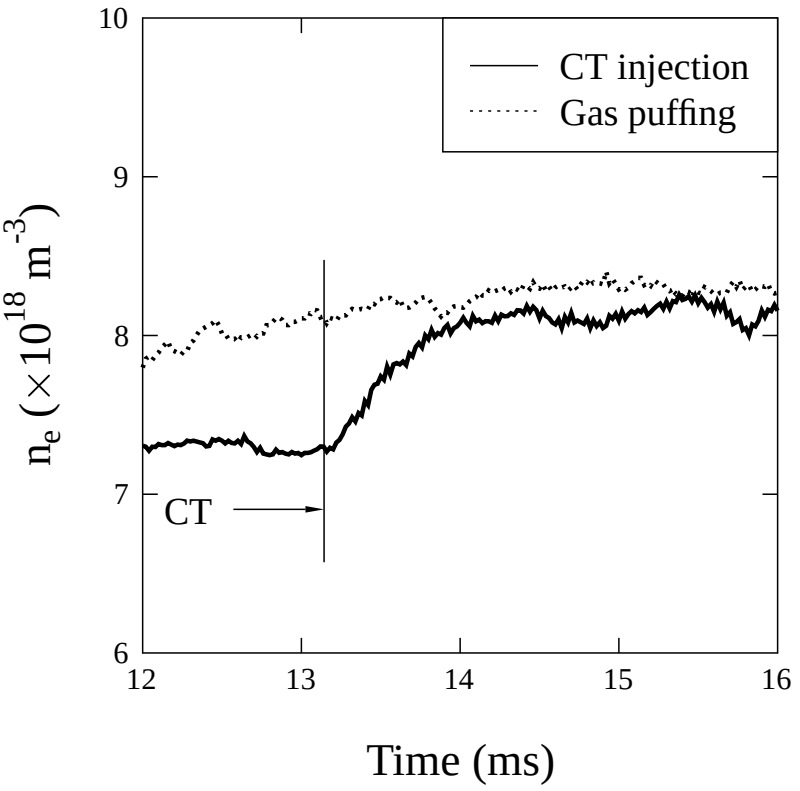

Figure 6.9: Temporal evolution of the line averaged density (center chord) during STOR-M discharge with vertical CT injection. Discharge condition: $B_t = 0.7$ T, $V_{form} = 18$ kV, $V_{acc} = 16$ kV.

kinetic energy of CT for deeper penetration. Figure 6.10 shows the response of SXR emission to vertical CT injection at 14.9 ms. The SXR emission rapidly increases to a higher level within 600 μs. The delays for the density increase in Figure 6.7 for $V_{acc} = 14$ kV and the SXR emission increase in Figure 6.10(b) at $V_{acc} = 16$ kV are on the same order of magnitude. An increase in the SXR emission from the central chord usually indicates an increase in the temperature and/or density in the core region. The particles from the CT must enter the core region and be heated by the main tokamak plasma to make detectable contributions to the SXR signal. The SXR emission measurement suggests that the core penetration of STOR-M plasma

by vertical CT injection has been achieved at higher V_{acc}.

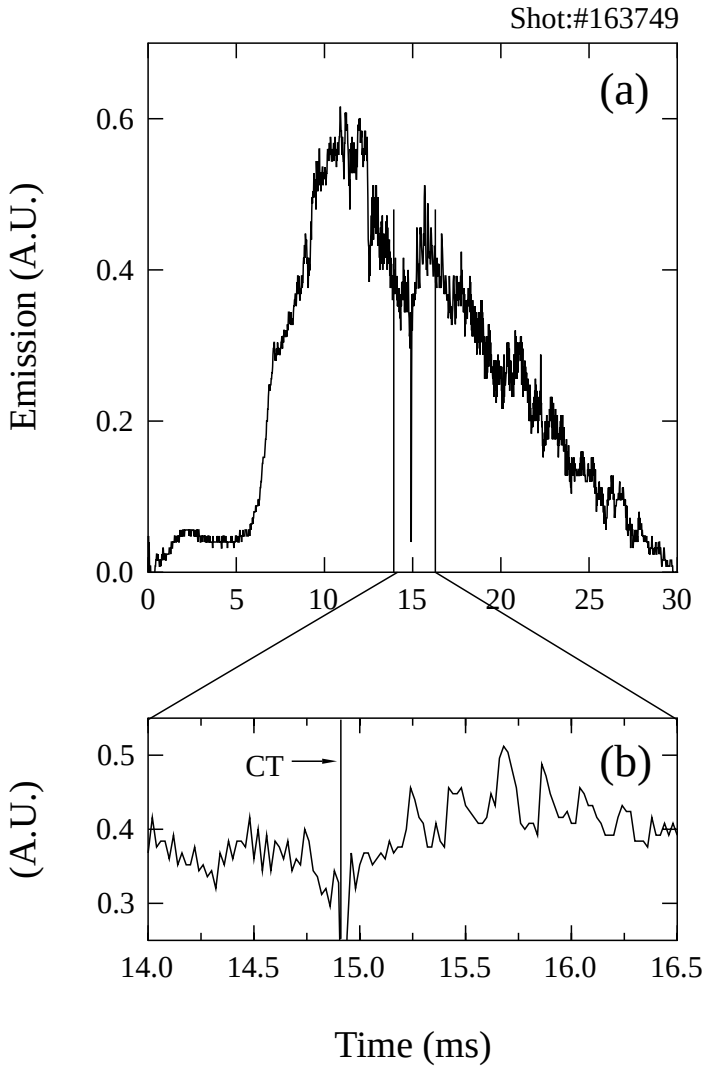

Figure 6.10: Evolution of SXR emission along a center chord from a tokamak discharge with a CT injected at 14.9 ms. Discharge conditions: $B_t = 0.7$ T, $V_{acc} = 16$ kV.

6.4.5 Comparison with tangential injection

Tangential CT injection has been performed to make comparison with vertical injection to study CT fuelling effects. In tangential injection without triggering H-mode, the typical increase in line-averaged density of about $0.25 \times 10^{19}\mathrm{m}^{-3}$ is usually observed under the same discharge conditions. The formation and acceleration bank voltages are 18 kV and 16 kV respectively. The increase in density is two times of

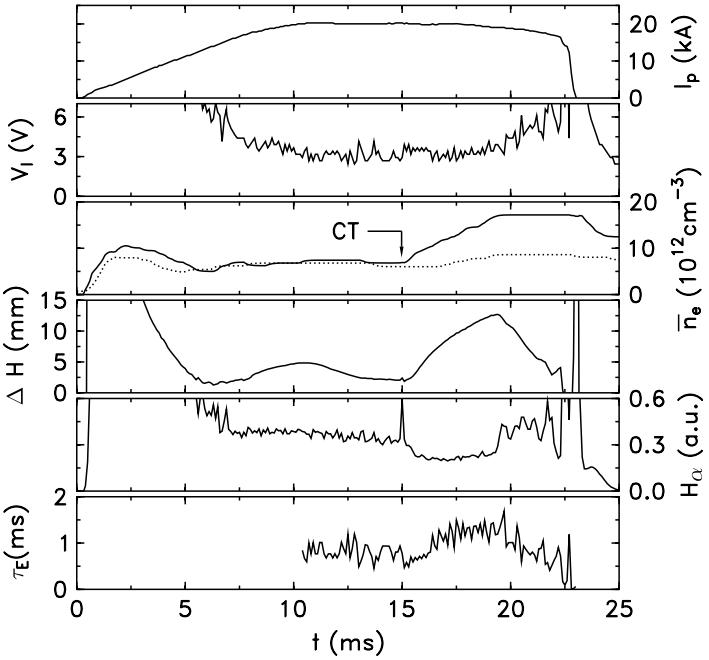

Figure 6.11: Typical waveforms of H-mode like discharges in STOR-M triggered by tangential CT injection, from C. Xiao [8].

that in vertical injection. The higher density increases by tangential injection are caused by higher CT velocity, $\sim 300\,\mathrm{kms}^{-1}$ and less CT density decay due to the shorter distance between the exit of acceleration section and the center of the STOR-M vacuum chamber. Figure 6.11 shows the waveforms of H-mode-like discharges in STOR-M triggered by the tangential CT injection [8], from top: plasma current, loop voltage, line averaged density, horizontal displacement, H_α emission intensity, and energy confinement time. The improvement in STOR-M plasma confinement in the H-mode-like discharges is characterized by doubling the line-averaged density (center chord), significant reduction in H_α emission level, steepening of the edge density profile, and suppression of floating potential fluctuation and $m = 2$ Mirnov oscillations. In the case of tangential CT injection with H-mode triggering, the line averaged electron density increases from $0.75 \times 10^{19}\,\mathrm{m}^{-3}$ to $1.7 \times 10^{19}\,\mathrm{m}^{-3}$ within 5 ms. It was found that vertical CT injection caused faster density increase than that in tangential injection. The density increase in tangential injection is due to both CT fuelling and L-H transition.

In the vertical injection, H-mode like phenomena have also been observed, such as

suppression of the $m = 2$ oscillation and a drop in H_α emission. Figure 6.12 depicts the $m = 2$ and m =3 Mirnov oscillations during the same tokamak discharge. It can be clearly seen that the CT injection led to suppression of $m = 2$ Mirnov oscillations for about 2.3 ms but had little effect on the $m = 3$ Mirnov oscillations. Figure 6.13 shows the drop in the H_α emission following vertical injection.

In the vertical injection experiments, a bending drift tube was used to redirect the CT injection direction from horizontal to vertical direction. The CTs are able to follow the curved drift tube. The CT velocity remains nearly constant at all locations in the drift tube. However, the compressor slows down the CT and causes significant decrease in the CT magnetic field. The results previously reported by Fukumoto *et al.* [53] and also reported in this thesis suggest that a bending drift tube can be used to effectively alter the CT direction. Vertical CT injection experiments resulted in some encouraging phenomena including increases in electron density and SXR emission level, although those phenomena have occurred in separate shots during the experiments reported in this thesis. The density ($\bar{n}_e$) increase which was observed in tangential CT injection experiments was due to both CT fueling and L-H transition. In the case of vertical injection the density increase is presumably due to the fuelling effect since there is no clear evidence of H-mode triggering in our vertical CT injection experiments. CT gas puffing without discharge causes density increase with a delay of 5 ms. This delay was also observed in previous tangential CT injection experiments but with a shorter delay time of 2 ms. The longer delay in the vertical injection case is mainly due to the addition of the 90° bending drift tube and smaller diameter of the port, which reduced the conductance of the neutral gas.

Initial CT penetration through the magnetic field in the tokamak port is still considered a major difficulty for both horizontal and vertical CT injection experiments. In tangential injection, the distance between the exit of the acceleration section and the center of the STOR-M vacuum chamber, $L_p = 27$ cm. While in vertical injection, however, L_p is increased to 127 cm due to the curved drift tube, the compressor, the bellows and the longer STOR-M vertical port. In tangential injection, CT kinetic energy density equals to the tokamak toroidal field energy density, $K_{CT} \simeq B_t^2/2\mu_0$,

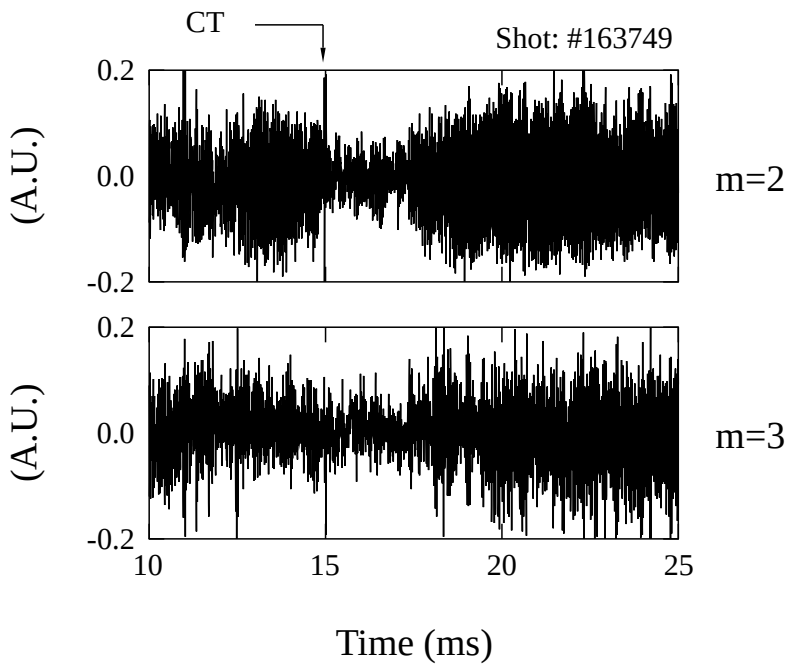

Figure 6.12: The $m = 2$ and $m = 3$ Mirnov oscillation signals in a tokamak discharge with a CT injected at 14.9 ms.

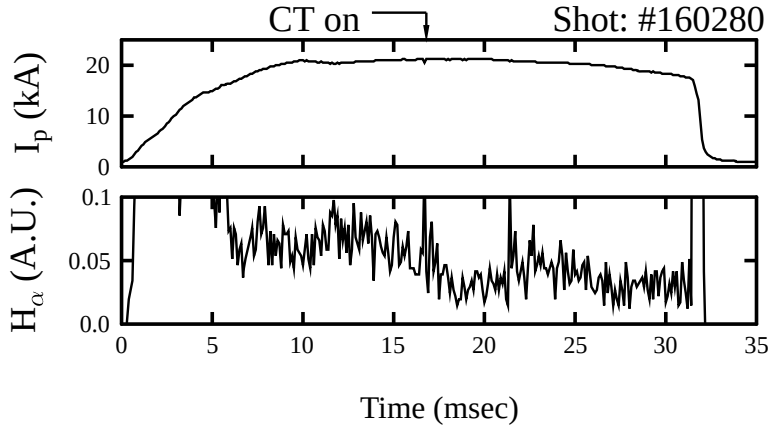

Figure 6.13: H_α drop in a tokamak discharge with a CT injected at 14.9 ms.

according to $V_{CT} \simeq 300\,\mathrm{kms}^{-1}$ and $\rho_{CT} \simeq 2.5 \times 10^{21}\,\mathrm{m}^{-3}$. Therefore, CTs are able to penetrate the tokamak toroidal field (0.7 T). In vertical injection, however, the CT kinetic energy density is significantly lower than the magnetic energy density of the STOR-M toroidal field, $K_{CT} \simeq 4\%$ of $B_t^2/2\mu_0$. This is mainly due to the CT density decay in the longer traveling distance and the significant deceleration of CT by the compressor.

Chapter 7

Conclusions and future work

As remarkable progress toward burning fusion plasma has been achieved in last two decades, for example, the fusion triple product has reached 1.5×10^{21} m^{-3}keV $\cdot$ s which is close to the fusion ignition condition (three times larger than the above value), it is more clear that the central fuelling of a reactor-grade tokamak is of great importance to the development of fusion as an energy source. The conventional tokamak fuelling methods, including gas puffing and cryogenic pellet injection are considered inadequate to meet the goal of central fuelling a reactor-size tokamak, such as ITER. Accelerated CT has the potential to centrally fuel such a large tokamak because of its unique fuelling mechanism. So far, the experimental studies on tokamak fuelling by CT have demonstrated the feasibility of centrally fuelling a large tokamak by CT injection. In these experiments, CTs were injected at different angles, for example, radial injection and tangential injection.

This thesis contributes to the investigation on tokamak fuelling by CT injection at different angles. The CTs produced in USCTI were injected vertically into the STOR-M toroidal field. Vertical CT injection was considered to be able to achieve deeper penetration. Prior to actual vertical injection, the bench tests of CT translation in the 90° bend were performed. Two kinds of configurations have been tested. Experimental measurements of the STOR-M plasma response to vertical CT injection have provided us with a comprehensive understanding of the physics of CT itself and tokamak fuelling by CT injection.

7.1 Conclusions

Vertical CT injection into the STOR-M tokamak has been demonstrated, for the first time, on the STOR-M tokamak. To perform vertical injection, the original USCTI has been modified. The modifications included adding a segment of a 90° flux conserving drift tube and a compressor to the exit of the original acceleration section. The experimental studies on CT translation in the 90° curved drift tube were carried out. Magnetic probes, Langmuir probe, and multi-channel monochromator for H_α emission measurement were used to characterize the CT plasma parameters. Bench test results in this configuration have confirmed that the CT, injected horizontally into the 90° bend, can be deflected to the vertical direction. Moreover, the experimental results have extended the CT velocity passing through the 90° bending drift tube from $40\,\mathrm{kms}^{-1}$ in Fukumoto's experiments [53] to $130\,\mathrm{kms}^{-1}$. At this speed, the magnetic probe measurements showed that the CT magnetic field structure kept intact as a typical structure of a compact torus plasma. At $V_{acc} = 14$ kV, CT velocity at the exit of the acceleration reached 230 kms^{-1}. A velocity of 130 kms^{-1} was obtained while CT passed the bend and it decreased to about 40 kms^{-1} after the compressor. The CT density is $(0.6 \sim 1) \times 10^{21}\,\mathrm{m}^{-3}$ at the downstream of the compressor.

Bench tests were also performed in another configuration in which an inner curved electrode was added to the original one. The length of CT acceleration section was increased from 60 cm to 114 cm. In this configuration a higher CT velocity $\sim 180\,\mathrm{kms}^{-1}$ was detected at $V_{acc} = 14$ kV while the CT passed the curved acceleration section. At $V_{acc} = 16$ kV this value increased to 270 kms^{-1}. The H_α emission measurement showed that the CT could reach a distance as far as the traveling distance for actual vertical injection. In addition, a one-dimensional point model was employed to study the CT acceleration dynamics in the modified acceleration region under the conditions of the USCTI typical operation parameters. The numerical results agreed well with the experimental measurements. Along with the improvement in CT velocity in the curved acceleration region, field amplification was also observed.

A CT experiences a centrifugal force due to the curvature in the trajectory. The CT is expected to be compressed which leads to field amplification. When the CT translated in the curved drift tube at the velocity of 130 kms^{-1}, this velocity was not be high enough to attribute to field amplification. In the bench tests the CT velocity was decreased significantly by the compressor in the configurations with and without the inner electrode.

Based on the encouraging bench test results, actual vertical CT injection experiments have been performed in the STOR-M tokamak. The modified USCTI was connected with the STOR-M tokamak. CTs were injected through a vertical port on STOR-M. Typical parameters of the injected CT are: $(0.6 \sim 1) \times 10^{21}\,\text{m}^{-3}$ in density, ~ 0.005 Tesla in magnetic field and $\sim 100\,\text{kms}^{-1}$ in velocity. Injection of CTs into the STOR-M vacuum field was studied. It was found that the final CT velocity (after the compressor) increased linearly with acceleration bank voltage. CT velocity was 40 kms^{-1} at $V_{acc} = 13$ kV and about 100 kms^{-1} at V_{acc} =16 kV. The "blow-by" effect occurred when $V_{acc} = 17$ kV.

Under the USCTI discharge condition: $V_{form} = 18$ kV and $V_{acc} = 14$ kV, disruption-free STOR-M discharges have been achieved with vertical CT injection. A prompt increase in the line averaged electron density, an increase in soft X-ray emission (center chord) and suppression of the m =2 Mirnov oscillation level have been observed following vertical CT injection. The typical density increase is about 20% within 600 μs at $V_{acc} = 16$ kV. The experimental results suggest that vertical CT injection is a feasible tokamak fuelling technique. Comparison between vertical injection and tangential injection was conducted. It was found that at $V_{acc} = 16$ kV, the density increase in the case of vertical injection is half of that in tangential injection without triggering H-mode discharge in STOR-M. The CT kinetic energy density was estimated in both cases: $K_{CT} \simeq B_t^2/2\mu_0$ for tangential injection and $K_{CT} \simeq 4\%$ of $B_t^2/2\mu_0$ for vertical injection. Compared with tangential injection, lower kinetic energy density of the CT in vertical injection is caused by much decay of the CT density due to longer CT traveling distance and smaller CT velocity.

7.2 Future work

CT injection as a means of tokamak fuelling has been tested in several tokamaks (TdeV, JFT-2M, STOR-M etc.) at different injection angles: radial, tangential and vertical. It has been demonstrated that CT injection is an important candidate for central fuelling a large tokamak or maybe the only way. Meanwhile, the techniques involved in CT formation, acceleration as well as CT translation have been greatly advanced. Some essential technical issues for CT injection include (1) the minimization of impurity levels caused by the gun electrodes (2) repetitive operation and (3) CT translation in curved drift tube. The work in this thesis has demonstrated vertical CT injection is a feasible injection scheme. To implement the vertical CT injection in a reactor-grade tokamak such as ITER, some further considerations are needed to be taken, including fuel deposition process, operational scenario and bend design for vertical injection. There is some work remaining to be done to get better understanding of tokamak fuelling by vertical CT injection.

Firstly, it is of interest to study the evolution of λ of the CT and its profile in the 90° flux conserving bend during CT translation in a curved drift tube, where λ is a parameter determined by the CT equilibrium (see Eq. (3.1)). Since the capability of translation of the accelerated CT in a 90° bend provides the basis for vertical CT injection experiments, it is important to investigate the effects of the curvature of the bend on the CT. Previous experimental measurements for CT decay in a linear drift tube [73] showed that λ was well characterized as a constant immediately following CT formation and departures from constant, which were well characterized by a λ profile, quadratic in Ψ or linear in Ψ. To investigate the λ profile for CTs in a 90° bend, measurements of CT magnetic field profiles with high spacial resolution are required, e.g., an array of 10 miniature magnetic pick-up coils would be suitable for the 90° bend in the USCTI. More care needs to be taken for the design of the magnetic probe to minimize the perturbation of the insertion of the probe on the CT plasma. The experimental results will elucidate the shape effects of the bend on the CT equilibrium and decaying and further benefit the bend design for vertical

injection.

Secondly, the detailed vertical CT penetration process in the tokamak vacuum chamber is needed to be well diagnosed. This is essential to understand the fuel deposition process by CT injection involving magnetic reconnection and excitation of Alfvén waves. A two dimensional soft X-ray camera and a fast multi-frame streak camera are key diagnostic tools for this investigation.

Thirdly, it is important to investigate experimentally the feasibility of repetitive vertical CT injection into a tokamak. This is because minimizing the density perturbation of the target tokamak plasma is essential for fuelling a reactor-size tokamak in steady state operation. The fuel particles are expected to be replenished in a repetitive manner. This is also the fuelling scenario for ITER discharges. In these experiments, the technical challenges lie in modification of the present CT discharge banks, both formation and acceleration, to achieve repetitive discharges with $f \approx 20$ Hz [16, 50].

References

[1] "International Energy Agency Workshop Summary", *Fusion Sci. and Tech.* **49**, 79 (2006).

[2] M.C. Zarnstorff, M.G. Bell, M. Bitter, R.J. Goldston, B. Grek, R,J. Hawryluk, K. Hill, D. Johnson, D. McCune, H. Park, A. Ramsey, G. Taylor, and R. Wieland, *Phys. Rev. Lett.* **60** (13), 1306 (1988).

[3] C.E. Kessel, *Nucl. Fusion* **34** (9), 1221 (1994).

[4] P.B. Parks, *Phys. Rev. Lett.* **61**, 1364 (1988).

[5] L.J. Perkins, S.K. Ho and J.H. Hammer, *Nucl. Fusion* **28**, 1365 (1988).

[6] R. Raman, F. Martin, B. Quirion, M. St-Onge, J-L. Lachambre, D. Michaud, B. Sawatzky, J. Thomas, A. Hirose, D.Q. Hwang, N. Richard, C. Côté, G. Abel, D. Pinsonneault, J-L. Gauvreau, B. Stansfield, R. Décoste, A. Côté, W. Zuzak and C. Boucher, *Phys. Rev. Lett.* **73**, 3101 (1994).

[7] T. Ogawa, N. Fukumoto, M. Nagata, H. Ogawa, M. Maeno, K. Hasegawa, T. Shibata, T. Uyama, J. Miyazawa, S. Kasai, H. Kawashima, Y. Miura, S. Sengoku, H. Kimura and JFT–2M Group, *Nucl. Fusion* **39**, 1911 (1999).

[8] S. Sen, C. Xiao, A. Hirose and R.A. Cairns, *Phys. Rev. Lett.* **88**, 185001 (2002).

[9] International Fusion Research Council, *Nucl. Fusion* **45**, A1 (2005).

[10] J. Wesson, *Tokamaks*, Oxford Science Publication, Oxford, (1987).

[11] F. F. Chen, *Introduction to plasma physics and controlled fusion*, Plenum press, New York (1984).

[12] ITER Physics Basics, *Nucl. Fusion* **39**, 2175 (1999).

[13] T. Fujita *et al.*, *Nucl. Fusion* **38**, 207 (1998).

[14] A. Fibson and the JET team, *Phys. Plasmas* **5**, 1839 (1998).

[15] P.T. Lang, *et al*. *Phys. Rev. Lett.* **79**, 1487 (1997).

[16] M.J. Gouge, D.Q. Hwang, L.R. Baylor, S.K. Combs, P.W. Fisher, C.R. Foust, S.L. Milora, H.S. McLean, R.D. Horton, R.W. Evans, J.C. Thomas, R. Raman, B.J. Denny, R.S. Willms, A. Frattolillo, and S. Migliori, *Fusion Energy 1996*, Montreal, IAEA-F1-CN64/GP-2, (IAEA, Vienna, 2003).

[17] ITER Performance Report 22, IAEA (1991).

[18] G. Becker, *Nucl. Fusion* **44**, 933 (2004).

[19] X. Garbet, *et al. Phys. Rev. Lett.* **91**, 035001 (2003).

[20] L.R. Baylor, S.K. Combs, T.C. Gernigan, W.A. Houlberg, L.W. Owen, D.A. Rasmussen, S. Maruyama, and P.B. Parks, *Phys. Plasmas* **12**, 056103 (2005).

[21] L.R. Baylor, T.C. Jernigan, S.K. Combs, W.A. Houlberg, M. Murakami, P. Gohil, K.H. Burrell, C.M. Greenfield, R.J. Groebner, C.-L. Hsieh, R.J. La Haye, P.B. Parks, G.M. Staebler, The DIII-D Team, G.L. Schmidt, D.R. Ernst, E.J. Synakowski, and M. Porkolab, *Phys. Plasmas* **7**, 1878 (2000).

[22] P.B. Parks, W.D. Sessions, and L.R. Baylor, *Phys. Plasmas* **7**, 1968 (2000).

[23] P.B. Parks and L.R. Baylor, *Phys. Rev. Lett.* **94**, 125002 (2005).

[24] V. Rozhansky, I. Senichenkov, I. Veselova, and R. Schneider, *Plasma Phys. Control. Fusion* **46**, 575 (2004).

[25] J.B. Taylor, *Rev. Mod. Phys* **58** (3), 741 (1986).

[26] W.A. Newcomb, *Phys. Fluids.* B **3** (8), 1818 (1991).

[27] A.W. Leonard, R.N. Dexter and J.C. Sprott, *Phys. Rev. Lett.* **57**, 333 (1986).

[28] A.W. Leonard, R.N. Dexter and J.C. Sprott, *Phys. Fluids* **30**, 2877 (1987).

[29] A.V. Voronin, V.K. Gusev, Yu.V. Petrov, N.V. Sakharov, K.B. Abramova, E.M. Sklyarova and S.Yu. Tolstyakov, *Nucl. Fusion* **45**, 1039 (2005).

[30] A.V. Voronin and K.G. Hellblom, *Plasma Phys. Control. Fusion* **43**, 1583 (2001).

[31] C.W. Hartman and J.H. Hammer, *Phys. Rev. Lett.* **48**, 929 (1982).

[32] J.H. Hammer, C.W. Hartman and J.L. Eddleman, *Phys. Rev. Lett.* **61**, 2843 (1988).

[33] J.H. Hammer, J.L. Eddleman, C.W. Hartman, H.S. McLean and A.W. Molvik, *Phys. Fluids* B **3**, 2236 (1991).

[34] M.R. Brown and P.M. Bellan, *Nucl. Fusion* **32**, 1125 (1992).

[35] M.R. Brown and P.M. Bellan, *Phys. of Fluids* B **2**, 1306 (1990).

[36] R. Raman. F. Martin, E. Haddad, M. St–Onge, G. Abel, C. Côté, N. Richard, N. Blanchard, H.H. Mai, B. Quirion, J.–L. Lachambre, J.–L. Gauvreau, G.W. Pacher, R. Décoste, P.J. Gierszewski, D.Q. Hwang, A. Hirose, S. Savoie, B.–J. Leblanc, H. Mclean, C. Xiao, B.L. Stansfield, A. Côté, D. Michaud and M. Chartré, *Nucl. Fusion* **37**, 967 (1997).

[37] C. Xiao, S. Sen, and A. Hirose, *Phys. Plasmas* **11**, 4041 (2004).

[38] C. Xiao, O. Mitarai, A. Hirose, W. Zawalski, D. White, E. Furkal, D. McColl, R. Raman, R. Décoste, B.C. Gregory, F. Martin, *Fusion Energy 1996*, Montreal, IAEA–CN–64/AP1–1, Vol. **II**, 963 (IAEA, Vienna, 2003).

[39] M. Nagata, N. Fukumoto, H. Ogawa, T. Ogawa, K. Uehara, H. Niimi, T. Shibata, Y. Suzuki, Y. Miura, N. Kayukawa, T. Uyama, H. Kimura and JFT-2M Group, *Nucl. Fusion* **41**, 1687 (2001).

[40] T. Ogawa, H. Ogawa, Y. Miura, H. Niimi, H. Kimura, Y. Kashiwa, T. Shibata, M. Yamamoto, N. Fukumoto, M. Nagata and T. Uyama, *J. Nucl. Mater.* **290–293**, 454 (2001).

[41] M. Nagata, H. Ogawa, S. Yatsu, N. Fukumoto, H. Kawashima, K. Tsuzuki, N. Nishino, T. Uyama1, Y. Kashiwa, T. Shibata, Y. Kusama and JFT–2M Group, *Nucl. Fusion* **45**, 1056 (2005).

[42] H. Niimi, T. Ogawa, H. Ogawa, N. Fukumoto, H. Kimura, Y. Miura, T. Shibata, M. Nagata, S. Yatsu, T. Uyama, N. Kayukawa, *Proc. 10th International Congress on Plasma Physics*, vol **3**, 768 (Québec, 2001).

[43] J.H. Degnan, R.E. Peterkin, Jr., G.P. Baca, J.D. Beason, D.E. Bell, M.E. Dearborn, D. Dietz, M.R. Douglas, S.E. Englert, T.J. Englert, K.E. Hackett, J.H. Holmes, T.W. Hussey, G,F, Kiuttu, F.M. Lehr, G.J. Marklin, B.W. Mullins, D.W. Price, N.F. Roderick, E.L. Ruden, C.R. Sovinec and P.J. Turchi, *Phys. Fluids* B **5** (8), 2938 (1993).

[44] J.H. Degnan, G.P. Baca, D.E. Bell, G. Bird, A.L. Chesley, S.K. Coffey, M.E. Dearborn, M.R. Douglas, S.E. Englert, T.J. Englert, D. Gale, J.D. Graham, K.E. Haxkett, J.H. Holmes, T.W. Hussey, G.F. Kiuttu, F.M. Lehr, G.J. MARKLIN, B.W. Mullins, R.E. Perterkin, Jr., D.W. Price, N.F. Rpderick, E.L. Ruden, M. Scott, S.W. Seiler, W. Sommars and P.J. Turchi, *Fusion Technology* **27**, 107 (1995).

[45] R. Roman, J.C. Thomas, D.Q. Hwang, G.D. Conway, F. Martin, A. Hirose, P. Gierszewski and R. Décoste, *Fusion Technology* **24**, 239 (1993).

[46] P.K. Loewenhardt, M.R. Brown, J. Yee, and P.M. Bellan, *Rev. Sci. Instrum.* **66**, 1050 (1995).

[47] K.L. Baker, D.Q. Hwang, R.W. Evans, R.D. Horton, H.S. McLean, S.D. Terry, S. Howard, C.J. DiCaprio, *Nucl. Fusion* **42**, 94 (2002).

[48] K.L. Baker, D.Q. Hwang, R.D. Horton, R.W. Evans, H.S. McLean, and S.D. Terry, *Fusion Energy 2000*, IAEA-CN-77/EXP4-14, (Sorrento, Italy, 2000).

[49] N. Fukumoto, H. Ogawa, M. Nagata, T. Uyama, T. Shibata, Y. Kashiwa, Y. kusama and JFT-2M Group, *Fusion Eng. and Des.* **70**, 289 (2004).

[50] R. Raman and P. Gierszewski, *Fusion Eng. and Des.* **39-40**, 977 (1998).

[51] J. Yee and P.M. Bellan, *Nucl. Fusion* **38**, 711 (1998).

[52] K.L. Baker, R.D. Horton, D.Q. Hwang, R.W. Evans, and S. Howard, *IEEE Trans. on Plasma Science* **30** (1), 48 (2002).

[53] N. Fukumoto, Y. Innoo, M. Nomura, M. Nagata, T. Uyama, H. Ogawa, H. Kimura, U. Uehara, T. Shibata, Y. Kashiwa, S. Suzuki, S. Kasai and JFT–2M Group, *Nucl. Fusion* **44**, 982 (2004).

[54] C. Xiao, A. Hirose and W. Zawalski, *Nucl. Fusion* **38**, 249 (1998).

[55] Y. Suzuki, T. Hayashi and Y. Kishimoto, *Nucl. Fusion* **41**, 769 (2001).

[56] Y. Suzuki, *et al.*, *Nucl. Fusion* **41**, 873 (2001).

[57] Y. Suzuki, T. Hayashi, Y. Kishimoto, *Phys. Plasmas* **7**, 5053 (2000).

[58] G. Bateman, *MHD instabilities*, MIT Press, Cambridge, Mass. (1978).

[59] R.S. Granetz, I.H. Hutchinson, and D.O. Overski, *Nucl. Fusion* **19**, 1587 (1979).

[60] O.P. Pogutse and E.I. Yurchenko, *Reviews of Plasma Physics* edited by M.A. Leontovich (Consultants Bureau, New York) **11**, 121 (1986)

[61] S.V. Goeler, W. Stodiek and N. Sauthoff, *Phys. Rev. Lett.* **33**, 1201 (1974).

[62] A. Sarkissian, A. Hirose, W. Zhang, *et al.*, *Can. J. Phys.* **68**, 369 (1990).

[63] J.W. Connor, R.J. Hastie, and J.B. Taylor, *Phys. Rev. Lett.* **40**, 396 (1978).

[64] A. Hirose, *Lecture Notes on Plasma Waves*, University of Saskatchewan, Chapter 4, 21 (2002).

[65] A.A. Galeev, V.N. Oraevskii, and R.Z. Sagdeev, *Sov. Phys. JETP* **17**, 615 (1963).

[66] J.Q. Dong, W. Horton, and J.Y. Kim, *Phys. Fluids* B **4**, 1867 (1992).

[67] W. Horton, *Rev. Mod. Phys.* **71**, 735 (1999).

[68] W. Horton, D. Choi, and W.M. Tang, *Phys. Fluids* **24**, 1077 (1981).

[69] J.W. Connor, *Plasma Phys. Control. Fusion* **35**, (1993).

[70] S. Coda, *et al.*, *Phys. Plasmas* **12**, 056124 (2005).

[71] J.B. Taylor, *Phys. Rev. Lett.* **33**, 1139 (1974).

[72] P.M. Bellan, *Spheromaks: A Practical Application of Magnetohydrodynamics Dynamos and Plasma Self-Organization*, Imperial College Press, (2000).

[73] C.G.R. Geddes, T.W. Kornack and M.R. Brown, *Phys. Plasmas* **5**, 1027 (1998).

[74] Finn, Manhaimer, and Ott, *Phys. Fluids* **24** (7), 1336 (1981).

[75] M.J. Schaffer, *Phys. Fluids* **30**, 160 (1987).

[76] A.W. Molvik, J.L. Eddleman, J.H. Hammer, C.W. Hartman, and H.S. McLean, *Phys. Rev. Lett.* **66**, 165 (1991).

[77] E. Hameiri, D.C. Stevens and W. Grossmann, *Phys. Fluids* **28**, 590 (1985).

[78] W.C. Turner, G.C. Goldenbaum, E.H.A. Granneman, J.H. Hammmer, C.W. Hartman, D.S. Prono and J. Taska, *Phys. Fluids* B **26**, 1965 (1988).

[79] J. Miyazawa, H. Yamada, K. Yasui, S. Kato, N. Fukumoto, M. Nagata, and T. Uyama, *Fusion Eng. and Des.* **54**, 1 (2001).

[80] K.L. Baker *et al.*, App. Phys. Lett. **79**, 1237 (2001).

[81] M.R. Brown, D.M. Cutrer, and P.M. Bellan, *Phys. Fluids B* **3** (5), 1198 (1991).

[82] E.N. Parker, *Astrophys, J. Suppl. Ser.* **8**, 177 (1963).

[83] P.A. Sweet, IAU *Symp.* **6**, 123 (1958).

[84] H.E. Petschek, *NASA Spec. Publ.* **SP-50**, 425 (1964).

[85] C.W. Hartman, W.L. Barr, J.L. Eddleman, M. Gee, J.H. Hammer, S.K. Ho, B.G. Logan, D.J. Meeker, A.A. Mirin, W.M. Nevins, L.J. Perkins, D.E. Shumaker, A. Leonard, P.B. Parks, H. McLean, E. Morse, and D.R. Solvin, 12^{th} *Internaional Conference on Plasma Physics and Controlled Nuclear Fusion Research*, IAEA-CN-50/H-1-11, (Nice, France, 1988).

[86] A. Hirose, C. Xiao, O. Mitarai, J, Morelli, and H.M. Skarsgard, *Physics in Canada* **60**, 111 (2006).

[87] C. W. Williams, *Master Thesis*, University of Saskatchewan (1995).

[88] J.C. Thomas, D.Q. Hwang, R.D. Horton, J.H. Rogers, and R. Raman, *Rev. Sci. Instrum.* **64**, 1410 (1993).

[89] K.W. Gentle, *Rev. Mod. Phys.* **67** (4), 809 (1995).

[90] R.H. Huddlestone and S.L. Leonard, *Plasma diagnostic techniques*, Academic press, New York (1965).

[91] I.H. Hutchinsin, *Principles of Plasma Diagnostics*, Cambridge University Press, New York (1987).

[92] P.C. Stangeby, *Phys. Fluids* **27** (3), 682 (1984).

[93] C. Riccard, G. Longoni, G. Chiodini, and M. Fontanesi, *Rev. Sci. Instrum.* **72** (1), 461 (2001).

[94] H. Ji, H. Toyama, K. Yamagishi, S. Shinohara, A. Fujisawa, and K. Miyamoto, *Rev. Sci. Instrum.* **62** (10), 2326 (1991).

[95] S.G. Lee and J.G. Bak, *Rev. Sci. Instrum.* **72** (1), 442 (2001).

[96] S.L. Chen and T. Sekiguchi, *J. Appl. Phys.* **36** (8), 2363 (1965).

[97] L. Lindberg and L. Kristoferson, *Plasma Physics* **12**, 831 (1970).

[98] R.C. Phillips and E.B. Turner, *Rev. Sci. Instrum.* **36** (12), 1822 (1965).

[99] D.E.T.F. Ashby, L.S. Holmes, and M.A. Kasha, *J. Sci. Instrum.* **40**, 364 (1963).

[100] G. Decker and D.L. Honea, *J. Phys. E.: Sci. Instrum.* **5**, 481 (1972).

[101] S. Berglund, S. Weaterlund, and S. Svennerstedt, *J. Sci. Instrum.* **40**, 250 (1963).

[102] D.C. Black and R.M. Mayo, *Rev. Sci. Instrum.* **67** (4), 1508 (1996).

[103] E.J. Strait, *Rev. Sci. Instrum.* **67** (7), 2538 (1996).

[104] I. Semenov, S. Mironov, I.C. Nascimento, R.M.O. Galvao, Yu. Kuznetsov, *Rev. Sci. Instrum.* **70** (1), 449 (1999).

[105] J.T. Slough and K.E. Miller, *Rev. Sci. Instrum.* **72** (1), 417 (2001).

[106] L. Bilbao and D. Grondona, *Meas. Sci. Technol.* **5**, 288 (1994).

[107] R.M. Castro, M.V.A.P. Heller, R.P. Da Silva, I.L. Caldas, F.T. Degasperi, and I.C. Nascimento, *Rev. Sci. Instrum.* **68** (12), 4418 (1997).

[108] H. Bruzzone and D. Grondona, *Plasma Phys. Control. Fusion* **39**, 1315 (1997).

[109] H. Bruzzone, C. Moreeno and H. Kelly, *Meas. Sci. Technol.* **2**, 1195 (1991).

[110] A. Nagashima, A. Funahashi, T. Kawakami, T. Shoji and K. Takahashi, *Japan. J. App. Phys.* **17**, 1263 (1978).

[111] M. Emaami, O. Mitarai and S.W. Wolfe, *Plasma Physics Lab. Report*, University of Saskatchewan, PPL-86, (1986).

[112] Wei Zhang, *PhD. thesis*, University of Saskatchewan (1993).

[113] A.D. Cheetham, *Progress report* (ANU-PRL/TR85/6), Australian national university, Research school of physics science (1985).

[114] M. Emaami, *PhD. thesis*, University of Saskatchewan (1990).

[115] M. Emaami and H. Rasouli, *Meas. Sci. Technol.* **15**, 1000 (2004).

[116] C.J. Buchenauer and A.R. Jacobson, *Rev. Sci. Instrum.* **48**, 769 (1977).

[117] E.L. Ruden, B.W. Mullins, M.E. Dearborn, and S.K. Coffey, *Phys. Fluids* B, **4** (7), 1800 (1992).

[118] *The HEATH Scanning Monochromator EU-700 Series User Manual* (HEATH Company).

[119] C. Xiao, D. Liu, S. Livingstone, A.K. Singh E. Zhang and A. Hirose, *Plasma Sci. Tech.* **7**, 2701 (2005).

[120] D. Liu, C. Xiao, A.K. Singh, and A. Hirose, *Nucl. Fusion* **46**, 104 (2006).

[121] D.Q. Hwang, M. Ryutova, and H. Mclean, *Phys. Plasmas* **6** (5), 1515 (1999).

[122] W. Pfeiffer and R.E. Waltz, *Nucl. Fusion* **19**, 51 (1979).

[123] M.N. Bussac, *et al., Phys. Rev. Lett.* **35**, 1638 (1975).

[124] A. Hirose, *Phys. Rev. Lett.* **92**, 025001 (2004).

Appendix A

Density calculation with two fringe signals

In STOR-M, the line averaged electron density is measured by a 4 mm microwave interferometer. A fringe counter is used to resolve the density in real time. In principle, the fringe counter has resolution of a quarter of a fringe, corresponding to one step of the fringe counter output (0.25 volt). This is the minimum identifiable density variation which can be detected by the fringe counter for STOR-M plasma. In the density measurements, one step corresponds to $0.58 \times 10^{18}\,\mathrm{m}^{-3}$ and one fringe $2.32 \times 10^{18}\,\mathrm{m}^{-3}$, which is 4 steps.

An alternative to resolve the temporal evolution of the STOR-M plasma density is by numerical calculation [110, 115]. In this case, the two fringe signals along with the density signal are collected simultaneously in the experiments. As described in Chapter 4, the two fringe signals were adjusted to be the sine and cosine of the phase shift $\Delta\phi$ and, therefore, the phase shift can be described as

$$\Delta\phi(t) = \tan^{-1}(\mathrm{V_2(t)/V_1(t)})_\mathrm{i} + \pi \mathrm{k_i}. \tag{A.1}$$

In Eq. (A.1), $\Delta\phi$ is determined by monitoring the values of an increase or a decrease in k_i in the previous step. Here, the subscript i refers to the quantity at the ith sampling time ($20\,\mu$s). The resolution of the calculated $\Delta\phi(t)$ is 1/40 of one fringe. Figure A.1 shows the flow chart to calculate the phase shift.

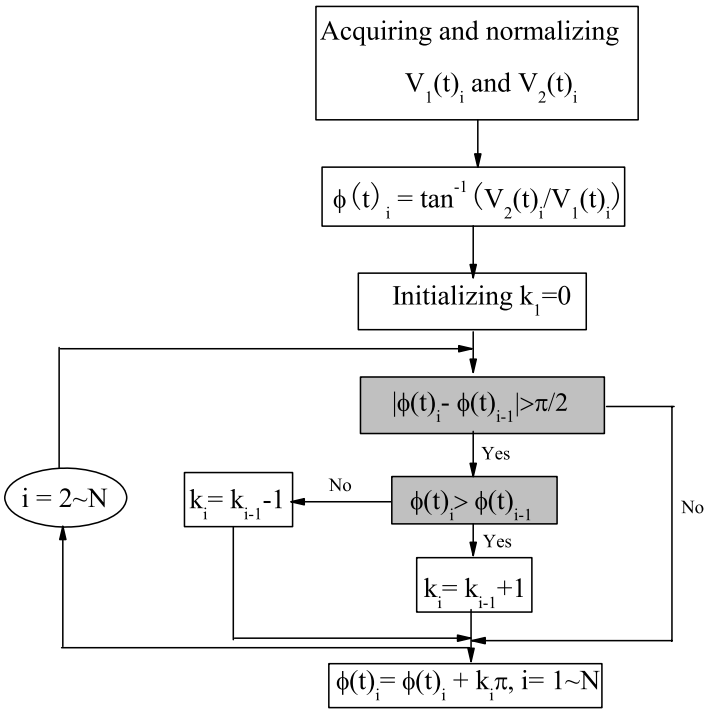

Figure A.1: Flow chart of numerical calculation of density with two fringe signals, from Nagashima [110].